FACOLTÀ DI INGEGNERIA

DIPARTIMENTO DI INGEGNERIA DELL'INFORMAZIONE

PhD Course in Information Engineering

Curriculum "Biomedical, Electronics and Telecommunication Engineering"

SSD: ING-INF/06

Advanced techniques for EMG-based assessment of muscular co-contraction during walking

Doctoral Dissertation of: **Annachiara Strazza**

Supervisor: **Prof. Sandro Fioretti**

Co-supervisor**: Dott. Ing. Francesco Di Nardo**

To my grandma

To my parents

To my sister

To my brothers

The only source

of knowledge

is experience.

(A.E.)

INDEX

INTRODUCTION

Gait analysis is defined as the systematic study of human locomotion aided by instrumentation for measuring body mechanics and muscles activity. A central part of the gait analysis is represented by surface electromyography (sEMG), providing the assessment of the activation patterns of muscles involved in gait [1][2] and supporting the objective description of muscular function during walking. The sEMG signals can show a wide inter-person variability and they can also differ for the same motion even within the same person, reflecting the variability in muscles activity during walking. A central role in controlling walking is played by lower limb muscles, and in particular by lower limb muscular co-contraction. Muscular co-contraction is defined as the concomitant recruitment of muscles usually acknowledged as agonist and antagonist crossing a targeted joint [3]. It is acknowledged that muscle co-contraction has an important role in movement regulation during motor learning activities, enhancing joint stability, in particular ankle and knee joint [4], [5]. Muscle co-contraction should be a crucial factor to consider during motor rehabilitation. Thus, this mechanism represents a known strategy of the neuromuscular system for improving postural stability, joint stiffness and movement accuracy [6]. Muscular co-contraction was identified in both healthy and pathological populations [7][8]. In able-bodied subjects, co-contraction occurs to achieve a homogeneous pressure on joint surface, preserving the articular stability and controlling its mechanical impedance [7]. In pathological and injured individuals, e.g. in those who are affected by joint chronic instability or suffered ligaments injuries, co-contraction appeared to have a key role in developing compensation strategies by enhancing joint stability [9][10]. Thus, quantitative assessment of muscle co-contractions is meaningful for deepening the comprehension of this neurophysiological

mechanism and for discriminating dysfunction conditions of the central nervous system, such as traumatic brain injury, stroke, cerebral palsy, or Parkinson's disease [7].

Albeit the problem of quantifying co-contraction activity of lower-limb muscles is far to be solved, sEMG has acknowledged as a common experimental tool to assess time duration and magnitude of antagonistic muscle activity. Different methodologies for EMG processing in time domain were developed to this purpose. In 1985, Falconer and Winter [6] introduced a co-contraction index (CI) based on the computation of areas under the curve of the rectified EMG signal from antagonist muscles. Similar formulation for CI was reported [11][12]. Although these techniques keep on being used also nowadays [5][12][13], they are able to provide only an overall numerical index but not a time course of co-contraction, that could be suitable to characterize more dynamic task such as walking. Rudolph et al. [12] overcame this limitation developing a dynamic co-contraction index that describes the temporal and magnitude components of EMG signals from antagonist muscles. However, a recent study in young adults showed that Rudolph's index may present a poor reliability during gait [13]. Further studies provided information about muscular co-contraction by overlapping linear envelopes or by evaluating sample by sample magnitude of relative activation of muscular pair in selected strides [9]. Moreover, co-contraction has been quantified as the temporal interval (in percentage of gait cycle) where EMG activity of the two muscles superimposed, but no information is reported on its magnitude [5][10] . Thus, a gold standard for identifying muscle co-contraction is not available yet. Moreover, poor information is available in literature to assess the frequency band where the muscles showed the reported co-contractions.

The aim of the present study is to perform a comprehensive EMG-based analysis of muscular co-contraction during walking by proposing new and reliable techniques for the assessment of muscle co-contraction in time-frequency domain and by providing normative data on leg-muscle co-contraction during heathy adult and child walking.

Wavelet transform (WT) analysis appears to be an appropriate tool for extraction of relevant EMG-based features in time-frequency domain [14][15]. WT is an advanced signal processing technique that maps a time waveform into time-scale providing a good localization in both time and frequency domains [16]. This multiresolution analysis allows to define time-frequency energy density

of a signal and to provide a localized statistical assessment of the time-frequency cross-energy density between two signals [17]. WT analysis of sEMG signal is the technique adopted in the present study, in the attempt of developing a novel approach for assessing muscle co-contraction. The proposed method is named CO-contraction DEtection algorithm (CODE). A further application of WT analysis is the extraction and assessment of fetal heart sounds, from fetal phonocardiography signal.

Statistical Gait Analysis (SGA)[18] is a recent and efficient technique, able to provide a statistical characterization of gait, by averaging spatial-temporal and sEMG-based parameters over hundreds of strides during the same walking trial of each subject. This technique relies on the cycle-dependency of muscle-activation during gait, so that averaging is performed only over features assessed in strides including the same number of activations [16]. Moreover, SGA allowed to quantify muscle co-contractions in terms of the onset-offset muscular activation and in terms of the occurrence frequency, i.e. the number of strides where simultaneous muscles activity has been detected [19]. The muscular co-contractions have been assessed as the period of overlap between activation intervals of the antagonist muscles [20][21]. This technique has been adopted in the present study, to provide reference data on lower-limb-muscle co-contraction during heathy adult and child walking.

Chapter references

[1] J. Perry, *Gait Analysis: Normal and Pathological Function*, vol. 12. 1992.

[2] D. Sutherland, "The development of mature gait," *Gait and Posture*, vol. 6, no. 2. pp. 163–170, 1997.

[3] S. J. Olney, "Quantitative evaluation of cocontraction of knee and ankle muscles in normal walking," in *Biomechanics IX: International Congress of Biomechanics*, 1983, vol. 9, pp. 431–436.

[4] M. Seyedali, J. M. Czerniecki, D. C. Morgenroth, and M. E. Hahn, "Co-contraction patterns of trans-tibial amputee ankle and knee musculature during gait," *J. Neuroeng. Rehabil.*, 2012.

[5] F. Di Nardo, A. Mengarelli, E. Maranesi, L. Burattini, and S. Fioretti, "Assessment of the ankle muscle co-contraction during normal gait: A surface electromyography study," *J. Electromyogr. Kinesiol.*, vol. 25, no. 2, pp. 347–354, 2015.

[6] K. Falconer and D. A. Winter, "Quantitative assessment of co-contraction at the ankle joint in walking.," *Electromyogr. Clin. Neurophysiol.*, 1985.

[7] M. C. N. Rosa, A. Marques, S. Demain, C. D. Metcalf, and J. Rodrigues, "Methodologies to assess muscle co-contraction during gait in people with neurological impairment - A systematic literature review," *Journal of Electromyography and Kinesiology*, vol. 24, no. 2. pp. 179–191, 2014.

[8] A. Strazza, A. Mengarelli, S. Fioretti, L. Burattini, V. Agostini, M. Knaflitz, and F. Di Nardo, "Surface-EMG analysis for the quantification of thigh muscle dynamic co-contractions during normal gait," *Gait Posture*, vol. 51, pp. 228–233, 2017.

[9] W. J. Hurd, T. L. Chmielewski, M. J. Axe, I. Davis, and L. Snyder-Mackler, "Differences in normal and perturbed walking kinematics between male and female athletes," *Clin. Biomech.*, vol. 19, no. 5, pp. 465–472, 2004.

[10] A. Mengarelli, E. Maranesi, V. Barone, L. Burattini, S. Fioretti, and F. Di Nardo, "Evaluation of gender-related differences in co-contraction activity of shank muscles during gait," in *Proceedings of the Annual International Conference of the IEEE Engineering in Medicine and Biology Society, EMBS*, 2015, vol. 2015–Novem, pp. 6066–6069.

[11] G. Frost, J. Dowling, K. Dyson, and O. Bar-Or, "Cocontraction in three age groups of children during treadmill locomotion," *J. Electromyogr. Kinesiol.*, vol. 7, no. 3, pp. 179–186, 1997.

[12] K. S. Rudolph, M. J. Axe, and L. Snyder-Mackler, "Dynamic stability after ACL injury: Who can hop?," *Knee Surgery, Sport. Traumatol. Arthrosc.*, 2000.

[13] M. Mohr, K. Lorenzen, L. Palacios-Derflingher, C. Emery, and B. M. Nigg, "Reliability of the knee muscle co-contraction index during gait in young adults with and without knee injury history," *J. Electromyogr. Kinesiol.*, 2018.

[14] A. Merlo, D. Farina, and R. Merletti, "A fast and reliable technique for muscle activity detection from surface EMG signals," *Biomed. Eng. IEEE*, vol. 50, no. 3, pp. 316–323, 2003.

[15] G. Vannozzi, S. Conforto, and T. D'Alessio, "Automatic detection of surface EMG activation timing using a wavelet transform based method," *J. Electromyogr. Kinesiol.*, 2010.

[16] M. Vetterli and J. Kovačević, *Wavelets and subband coding*. 2007.

[17] P. Sukiennik and J. T. Białasiewicz, "Cross-correlation of bio-signals using continuous wavelet transform and genetic algorithm," *J. Neurosci. Methods*, 2015.

[18] V. Agostini and M. Knaflitz, "Statistical Gait Analysis," in *Distributed Diagnosis and Home Healthcare*, 2012, pp. 99–121.

[19] F. Di Nardo, V. Agostini, M. Knaflitz, A. Mengarelli, E. Maranesi, L. Burattini, and S. Fioretti, "The occurrence frequency: A suitable parameter for the evaluation of the myoelectric activity during walking," in *Proceedings of the Annual International Conference of the IEEE Engineering in Medicine and Biology Society, EMBS*, 2015, vol. 2015–Novem, pp. 6070–6073.

[20] A. R. Den Otter, A. C. H. Geurts, T. Mulder, and J. Duysens, "Gait recovery is not associated with changes in the temporal patterning of muscle activity during treadmill walking in patients with post-stroke hemiparesis," *Clin. Neurophysiol.*, 2006.

[21] L. A. Prosser, S. C. K. Lee, A. F. VanSant, M. F. Barbe, and R. T. Lauer, "Trunk and Hip Muscle Activation Patterns Are Different During Walking in Young Children With and Without Cerebral Palsy," *Phys. Ther.*, 2010.

Chapter 1

MYOELECTRIC SIGNAL

Any human activity, from a slight gesture to physical exercise, requires muscle contractions to achieve the desired movement, or to maintain a desired posture. These muscle contractions are the final result of a complex series of tasks: motion planning, generation of muscle control signals, and monitoring of sensory information to allow appropriate corrections of the movement original plan. A muscle contraction is performed by an electrical signal called action potential that will be generated and transmitted along spinal nerves, during the movement of body segment [1]. The electromyographic (EMG) signal is a biomedical signal that is composed of action potentials. EMG signals are often used by clinicians as a diagnostic tool especially in fields of neurology [2]. In addition, EMG signals can be used in the area of assistive and rehabilitation robotics for the control of assistive devices such as active exoskeletons and prostheses [3]. To extract information about the control of movement by the nervous system from EMG signals, it is necessary to understand the processes underlying the generation of the activation signal.

1.1 Anatomical and physiological description of motor unit and of motor unit action potential

The basic functional unit of the neuromuscular system is the motor unit. It comprises a motor neuron, including its dendrites and axon, and the muscle fibers innervated by the axon (Fig. 1.1) [4].

The motor neuron is in the ventral horn of the spinal cord or brain stem where it receives sensory and descending inputs from other parts of the nervous system. The axon of each motor neuron exits the spinal cord through the ventral root, or through a cranial nerve in the brain stem, and projects in a peripheral nerve to its target muscle and to the muscle fibers it innervates. The nervous impulses are produced by the motor neurons; they travel along the axons and are transmitted to muscle fibers through neuromuscular junctions. The electrical changes generated by activity of the MU can be acquired and amplified by electrodes located in muscle mass and these changes can be recorded and edited using EMG recorders. The representation of the changes generated by a MU is the motor unit action potential (MUAP). MUAP is a summation of the muscle fiber action potential (MFAP).

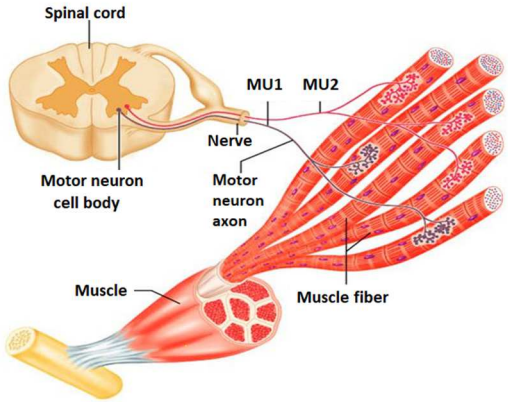

Fig. 1.1 Motor unit.

Let MFAPi(t) be the waveform of a muscle fiber action potential from the *i*-th fiber of a motor unit. Let MUAPj(t) be the electrical potential from the *j*-th motor unit, which arises as a sum of all MFAPs (Eq. 1) [5]:

$$MUAP_j(t) = \sum_{i=1}^{N_j} MFAP_i\,(t - \tau_i)s_j \qquad (1)$$

here τi is the temporal offset of MFAPi(t), and Nj is the number of fibers in motor unit j. The binary variable si represents the neuromuscular junction function that has a value of 1 if fiber i fires and 0 if not. Instead, τi depends on the location of the neuromuscular junction and the conduction velocity of

the muscle fiber. *Nj* represents the size of the motor unit (Nj ~ 10−10000). Because a single action potential in a motor neuron can activate hundreds of muscle fibers in synchrony, the resulting currents sum to generate an electrical signal that is readily detectable outside the muscle itself [6]. Because of the attenuation of MFAP with distance from the detection electrode, the size of the MUAP is often dependent on the location and diameter of the closest few muscle fibers. MUAP waveforms will vary in shape due to variations in the delays of the fiber potentials (affecting τi), possible changes in the position of the electrode relative to the muscle fibers (affecting MFAPi), and the possibility of a particular fiber failing to fire (affecting si). These variations are the source of stochastic biological variability in the MUAP waveform. [7].

1.2 Motor Unit Action Potential Train (MUAPT)

In order to maintain or increase the force generated by a muscle, the specific motor neuron must fire a temporal sequence of action potentials, called a spike train. Thus, one action potential from a single motor neuron results in one MUAP. Therefore, this spike train, when arriving at the neuromuscular junctions of all muscle fibers of this motor unit, results in a temporal sequence of MUAPs, called Motor Unit Action Potential Train (MUAPT), mathematically expressed (Eq.2):

$$MUAPT_j(t) = \sum_{i=1}^{M_j} MUAP_{jk}\left(t - \delta_{jk}\right)s_j \tag{2}$$

where MUAPTj(t) is the MUAPT of the *j*-th motor unit, MUAPjk(t) is the MUAP generated during the *k*-th firing of the *j*-th motor unit, Mj is the number of times the *j*-th motor unit fires, and δ_{jk} is the *k*-th firing time of the *j*-th motor unit [8].

1.3 Excitability of muscle membranes and action potential

The excitability of muscle fibers through neural control represents a major factor in muscle physiology [9]. This phenomenon can be represented by a model of a semi-permeable membrane describing the electrical properties of the sarcolemma. An ionic equilibrium between the inner and outer spaces of a muscle cell forms a resting potential at the muscle fiber membrane (approximately -80 to -90 mV at rest). This difference in potential which is maintained by physiological processes (ion pump) results in a negative intracellular charge compared to the external surface. The activation of an alpha-motor anterior horn cell, induced by the central nervous system, results in the conduction of the excitation along the motor nerve. After the release of transmitter substances at the motor endplates, an endplate potential is formed at the muscle fiber innervated by this motor unit. The diffusion characteristics of the muscle fiber membrane are briefly modified and Na+ ions flow in, causing a membrane Depolarization which is immediately restored by backward exchange of ions within the active ion pump mechanism, the Repolarization (Fig. 1.2).

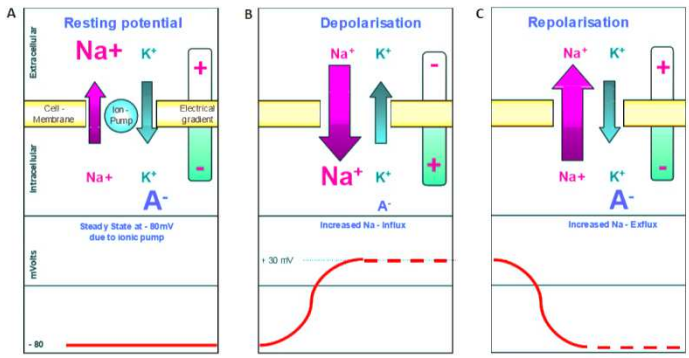

Fig. 1.2 Excitability of muscle membrane.

If a certain threshold level is exceeded within the Na+ influx, the depolarization of the membrane causes an Action potential to quickly change from – 80 mV up to + 30 mV (Fig. 1.3). It is a monopolar electrical burst that is immediately restored by the repolarization phase and followed by an after-hyperpolarization period of the membrane. Starting from the motor end plates, the action potential spreads along the muscle fiber in both directions and inside the muscle fiber through a tubular system.

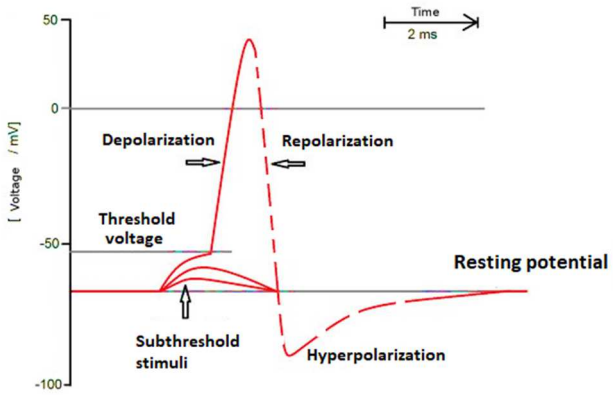

Fig. 1.3 Action potential.

This excitation leads to the release of calcium ions in the intra-cellular space. Linked chemical processes finally produce a shortening of the contractile elements of the muscle cell. Thus, EMG signal is based upon action potentials at the muscle fiber membrane resulting from depolarization and repolarization processes.

1.4 Skeletal Muscle Fibers and sarcomere

The best-known feature of skeletal muscle is its ability to contract and cause movement [10]. Skeletal muscles are able to regulate movement and to maintain posture. Skeletal muscles also prevent excess movement of the bones and joints, maintaining skeletal stability and preventing skeletal structure damage or deformation. Joints can become misaligned or dislocated entirely by pulling on the associated bones; muscles work to keep joints stable [11]. Each skeletal muscle is an organ that consists of various integrated tissues. These tissues include the skeletal muscle fibers, blood vessels, nerve fibers, and connective tissue. Each muscle is characterized by irregular connective tissue called the epimysium, which allows a muscle to contract and move powerfully while maintaining its structural integrity. The epimysium also separates muscle from other tissues and organs in the area, allowing the muscle to move independently. Muscle fibers are organized into individual bundles, each called a fascicle, by a middle layer of connective tissue called the perimysium. This fascicular organization is common in muscles of the limbs; it allows the nervous system to trigger a specific movement of a muscle by activating a subset of muscle fibers within a bundle, or fascicle of the muscle. Inside each fascicle, each muscle fiber is

encased in a thin connective tissue layer of collagen and reticular fibers called the endomysium. The endomysium contains the extracellular fluid and nutrients to support the muscle fiber [12] (Fig. 1.4).

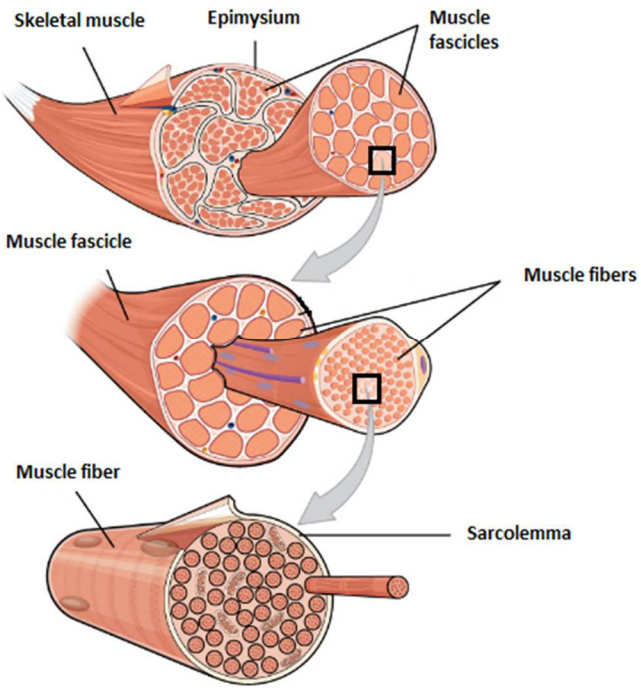

Fig. 1.4 Skeletal muscle, muscle fascicle and muscle fiber.

In the muscle fibers, the most important part is represented by the myofibrils. Each myofibril is about 10^{-6} m in diameter and extends the entire length of the muscle fiber. The number of myofibrils per fiber varies. At the end of the fiber, the myofibrils are attached to the plasma membrane by the intervention of specialized proteins. Each adjacent myofibrils are separated by a series of channels that open through the sarcolemma to the extra-fiber space. These channels are called the transverse tubules (T-tubules) because they run across the fiber. The transverse tubular system is a network of interconnecting rings, each of which surrounds a myofibril. The myofibrils are composed of sarcomeres, the functional contractile unit of a skeletal muscle fiber. Thus, a skeletal muscle fiber is surrounded by a plasma membrane, the sarcolemma, which contains sarcoplasm, the cytoplasm of muscle cells. The sarcomere is a highly organized arrangement of the contractile myofilaments, actin (thin filament) and myosin (thick filament), along with other support proteins. The arrangement of the thick and thin filaments creates light and dark regions along the myofibril. It is the light and dark regions of

the sarcomere that give the muscle fiber the striated appearance. Each sarcomere is approximately 2 μm in length with a three-dimensional cylinder-like arrangement and is bordered by structures called Z-discs (also called Z-lines, because pictures are two-dimensional), to which the actin myofilaments are anchored. The actin myofilaments are the main protein of the thin filament, but there are 2 regulatory proteins that are also part of the thin filament, troponin and tropomyosin. Likewise, because the myosin strands and their multiple heads (projecting from the center of the sarcomere, toward but not all to way to, the Z-discs) have more mass and are thicker, they are called the thick filament of the sarcomere. The different regions of the sarcomere are: I band, defined by where there are only thin filaments, A band, defined by the length of the thick filament, H zone, part of the A band where only the thick filament is present, M line, connective proteins in the middle of the H zone, Z discs or Z lines, proteins that form the boundary of the sarcomere [13]. A representation of sarcomere and its features is reported in Fig. 1.5.

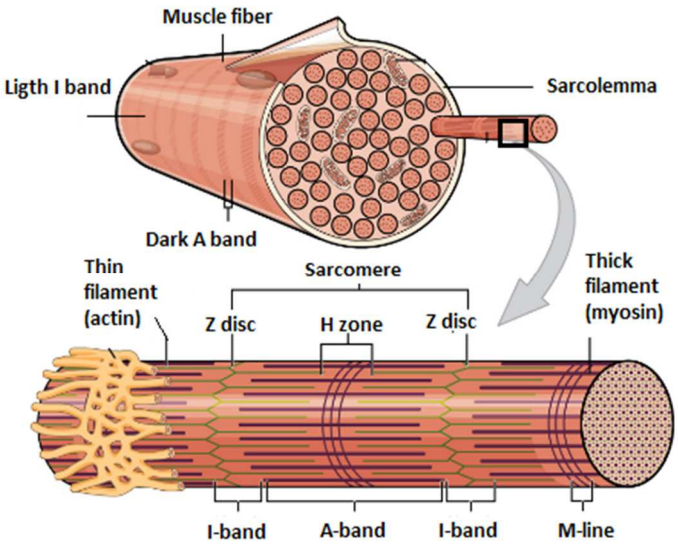

Fig. 1.5 Muscle Fiber. A skeletal muscle fiber is surrounded by a plasma membrane called the sarcolemma, which contains sarcoplasm, the cytoplasm of muscle cells.

1.5 The Neuromuscular Junction

Another specialization of the skeletal muscle is the site where a motor neuron's terminal meets the muscle fiber—called the neuromuscular junction (NMJ) [14]. This is where the muscle fiber first responds to signaling by the motor neuron. Every skeletal muscle fiber in every skeletal muscle is innervated by a motor neuron at the NMJ. Excitation signals from the neuron functionally stimulate fibers, to contract them. The NMJ consists of the end of the axon, the axon terminal (also known as the synaptic bulb or synaptic terminal) and the specialized region of the sarcolemma across from the synaptic terminal, the motor end plate. In the motor end plate, the sarcolemma is highly folded and contains special proteins. There is no physical contact between the neuron and muscle fiber, the small space between them is the synaptic cleft. Signaling begins when a neuronal action potential travels along the axon of a motor neuron, then along the axonal branches and then enters the axon terminal. When the action potential reaches the axon terminal, it stimulates the release of a neurotransmitter, called acetylcholine (ACh). The ACh molecules diffuse across the synaptic cleft and bind to specialized receptors, ACh receptors, in the motor end-plate of the sarcolemma. Once ACh binds to the receptor, a channel in the ACh receptor opens and positively charged ions can pass through into the muscle fiber, causing it to depolarize, meaning that the membrane potential of the muscle fiber becomes less negative (closer to zero). This depolarization is known as the end-plate potential. In the motor end plate is also an enzyme called acetylcholinesterase that hydrolyzes ACh which helps to end stimulation of the muscle fiber by the motor neuron.

1.6 Muscle Fiber Contraction and Relaxation

The sequence of events that result in the contraction of an individual muscle fiber begins with a signal from the motor neuron innervating that fiber. The local membrane of the fiber will depolarize as positively charged sodium ions (Na+) enter, triggering an action potential that spreads to the rest of the membrane will depolarize, including the T-tubules. In the membrane of the t-tubules there are voltage-sensitive proteins that are linked to proteins in the membrane of the sarcoplasmic

reticulum. When the action potential propagates down the t-tubule, the voltage-sensitive proteins are activated, and this triggers the release of calcium ions (Ca++) from the sarcoplasmic reticulum. The Ca++ then initiates contraction, which is sustained by ATP. As long as Ca++ ions remain in the sarcoplasm to bind to troponin, which keeps the actin-binding sites "unshielded," and as long as ATP is available to drive the cross-bridge cycling and the pulling of actin strands by myosin, the muscle fiber will continue to shorten to an anatomical limit.

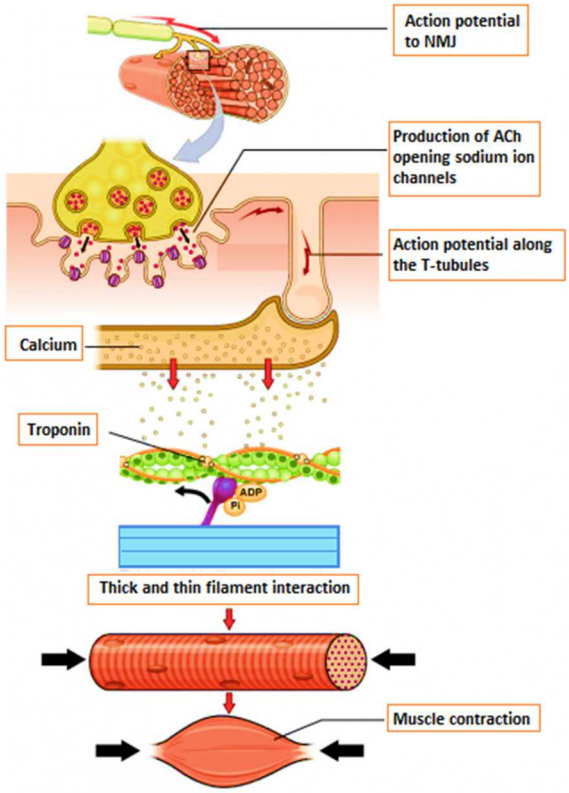

Fig. 1.6. Contraction of a Muscle Fiber.

Muscle contraction usually stops when signaling from the motor neuron ends, which repolarizes the sarcolemma and T-tubules, and closes the voltage-gated calcium channels in the sarcoplasmic reticulum (Fig. 1.6). Ca++ ions are then pumped back into the sarcoplasmic reticulum, which causes the tropomyosin to reshield (or re-cover) the binding sites on the actin strands [15]. A muscle also can stop contracting when it runs out of ATP and becomes fatigued (Fig. 1.7).

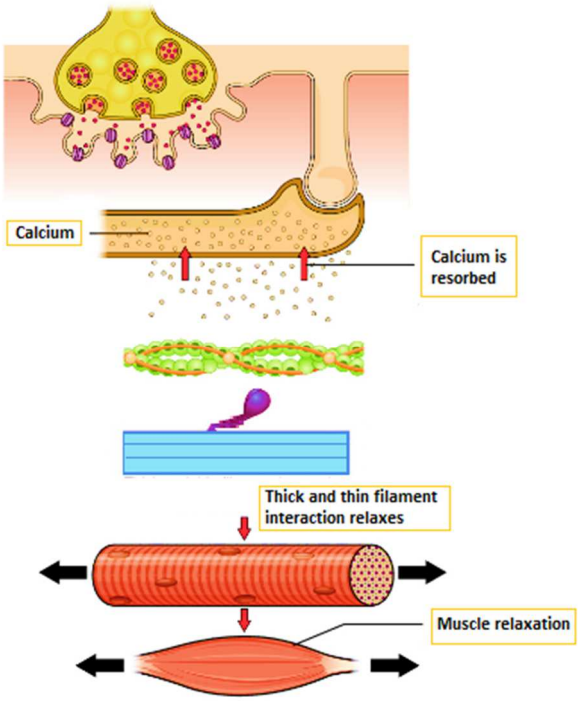

Fig. 1.7. Relaxation of a Muscle Fiber.

1.7 The electromyographic signal

An unfiltered and unprocessed signal detecting the superposed MUAPs is called a raw EMG Signal. EMG is defined as an experimental technique concerned with the development, recording and analysis of myoelectric signals. Myoelectric signals are formed by physiological variations in the state of muscle fiber membranes [16]. In particular EMG is the study of muscle function through the inquiry of the electrical signal the muscles emanate [16]. EMG signal is essentially the voltage fluctuation resulting from ionic current flows across the membranes of the muscle cells, when these cells are electrically or neurologically activated. Therefore, from the EMG signal, it is possible to analyze the biological processes of muscles. The EMG signal analysis allows to diagnose neuromuscular deficiencies such as caused by stroke and Parkinson's disease [50], and the biomechanics of human or animal movement. EMG can be categorized into two types, surface EMG and intramuscular EMG, based on the electrodes being used. In Surface EMG (sEMG) a pair of electrodes or a more complex array of multiple electrodes is placed on the surface of the skin above the muscle; while in intramuscular EMG,

(iEMG), typically either a monopolar or concentric needle electrode is inserted through the skin into the muscle tissue. Notably, the sEMG technique is preferred to measure EMG signals as this approach is free of discomfort and gives minimal risk of infection to amputees [17]. In this study, sEMG are used for its more advantages. Surface EMG recordings provide a safe, easy, and non-invasive method, allowing objective quantification of muscle activity. It is not necessary to penetrate the skin and record from single motor units to obtain useful and meaningful information regarding muscles [18]–[20].

A raw surface EMG recording (sEMG) is reported in Fig. 1.8:

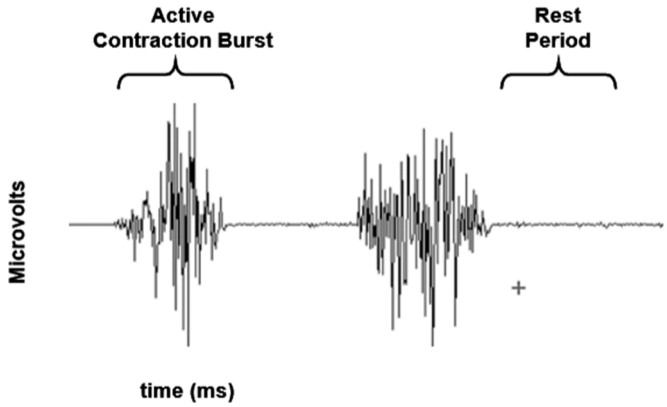

Fig. 1.8. The raw EMG recording.

The raw EMG baseline noise depends on many factors, especially the quality of the EMG amplifier, the environment noise and the quality of the given detection condition. Assuming a state-of-the-art amplifier performance and proper skin preparation, the averaged baseline noise should not be higher than 3 – 5 microvolts. SEMG amplitude is in a range between 0 to 10 mV and the frequency range is restricted from 10 to 500 Hz.

1.8 Factors influencing the EMG signal

During the detection and recording EMG signals, the main issue that affects the fidelity of the signals is the noise [21]. The factors affecting the EMG signal can mainly be classified into three basic categories: causative, intermediate and deterministic factors. The first one affects the signal directly. Causative factors can be classified into extrinsic and intrinsic factors. The extrinsic factors are related to the electrode structure and its placement. Intrinsic factors are due to the physiological and anatomical factors, depending by the number of active motor units, blood flow, amount of tissue between the surface of the muscle and the electrode. The intermediate factors can be due to band-pass filtering of the electrode alone with detection volume, superposition of action potentials of the EMG signal, and to the crosstalk from nearby muscles. Intermediate factors are the cause for deterministic factors. Deterministic factors are also caused by amplitude, duration and shape of motor unit action potential.

In general, noise is defined as electrical signals that are not part of the desired EMG signal [22]. The electrical noise affecting EMG signals can be due to electronics equipment, ambient noise, motion artifact, electrocardiographic artifacts, crosstalk, electrode contact, and transducer noise. Inherent noise is electrical noise generated by all types of electronic equipment which have frequency components that range from DC to several thousand Hz [23]. This noise can be contained using intelligent circuit design and high-quality instruments. In addition, the surface of human body is constantly exposed to electromagnetic radiations. Thus, the electromagnetic radiation is the source of ambient noise. Its amplitude is one to three times greater than the EMG signals of interest. The Power-Line Interference (PLI) is ambient noise arising from the 60 Hz (or 50 Hz) radiation of power sources. To remove this kind of noise, a notch filter can be used. Another kind of noise is related to motion artifacts. During the signal acquisition, the two main sources of motion artifacts are characterized by electrode interface and electrode cable. Motion artifacts can be reduced by proper design of the electronic circuitry and set-up. The frequency range of motion noise is usually from 1 to 10 Hz. The voltage range is comparable to the amplitude of the EMG signal. Recessed electrodes can contain the movement artifact significantly, in which a conductive gel layer is used between the skin surface and the electrode-electrolyte interface.

Instead, the inherent instability of signal is due to the quasi-random amplitude of EMG signals. The range 0-20 Hz of frequency components are unstable because they are affected by the firing rate of the motor units [17]. Because of the unstable nature of these signal components, it is considered as unwanted noise. The number of active motor units, motor firing rate and mechanical interaction between muscle fibers can change the behavior of information in EMG signals.

Electrical activity of the heart (ECG) is the foremost interfering component for EMG in the shoulder girdle (ECG artifact). This artifact often contaminates EMG signals, especially in trunk muscle electromyography [24]. The placement of EMG electrodes which is conducted by a selection of pathological muscle group often decides the level of ECG contamination in EMG. Due to an overlap of frequency spectra by ECG and EMG signals and their relative characteristics such as non-stationarity and varied temporal shape, it is very difficult to remove ECG artifacts from EMG signals.

During signal acquisition, an incorrect interpretation of the signal information is due to crosstalk. Crosstalk phenomenon consists in recording the volume-conducted electromyographic activity of muscles other than that under study. It depends on many physiological parameters and can be minimized by choosing, in an opportune way, the electrode size and inter-electrode distances

However, sEMG is affected also by the power line interference, the noise generated by the cable motion, the baseline and the movement artifact noise. In particular, the baseline is the combination of the two noise sources originated in the electronics of the amplification system (thermal noise) and at the skin-electrode interface (electrochemical noise), respectively. While the power line interference and the cable motion artifact can be removed using standard filtering procedures [16], the baseline and the movement artifact have spectra that include also the low frequency spectrum of EMG signal: a standard filtering risks to alter important information of the signal. The solution is to filter the maximum quantity of noise while keeping as much of the effective signal frequency spectrum as possible.

In the last years, a valid approach to remove noise from signal, without losing information, is represented by wavelet denoising algorithm, that have been received extensive consideration in the processing of white Gaussian noise in biological signals [25][26]. Wavelet based denoising literatures suggest the use of the Donoho's method [27], that estimates the thresholds by maximizing a risk

function in terms of quadratic loss at the sample points. A more details of this filtering technique is reported in chapter 4.

1.9 Muscle co-contraction

Muscle co-contraction is the simultaneous contraction of agonist and antagonist muscles crossing a joint [28]. Co-contraction generally-held purpose is to augment ligament function in maintenance of joint stability, providing resistance to rotation at a joint and equalizing pressure distribution at joint surfaces [29]. Muscle co-contraction has an important role in movement regulation during motor learning activities, enhancing joint stability and should be a crucial factor to consider during motor rehabilitation [30].

Physiologically, this mechanism is controlled by the neuromuscular system, allowing the contraction of both muscles [31]. It occurs through a motor neuron sending a signal (through creating action potentials) to the muscle fiber to contract. When signals are sent to all muscle fibers in a muscle group, the muscle group will contract as a whole. In the lower limbs, stability is important in upright standing balance. The co-activation (i.e. co-contraction) of different muscle groups allows for proper balance and the ability to adjust weight and to stay upright on uneven ground. It is also believed to be important for postural control by stabilizing the spine. Muscle co-contraction is necessary for learning a fine motor skill or for any activity involving stability. The reciprocal innervation should inhibit in order to realize a muscle co-contraction. Thus, a muscular co-contraction is performed by the contraction of a muscle and the concomitant relaxation of synergistic one.

Muscular co-contractions were assessed as the overlapping periods among activation intervals of the considered muscles in the same strides [30]. A muscular activity shorter than 30 ms does not yield an active control on a joint motion during gait [32], thus overlapping periods with a time length lower than 30 ms were discarded. An example of muscle co-contraction is reported in Fig.1.9; the muscle co-contraction between two sEMG signals is highlighted by a red box.

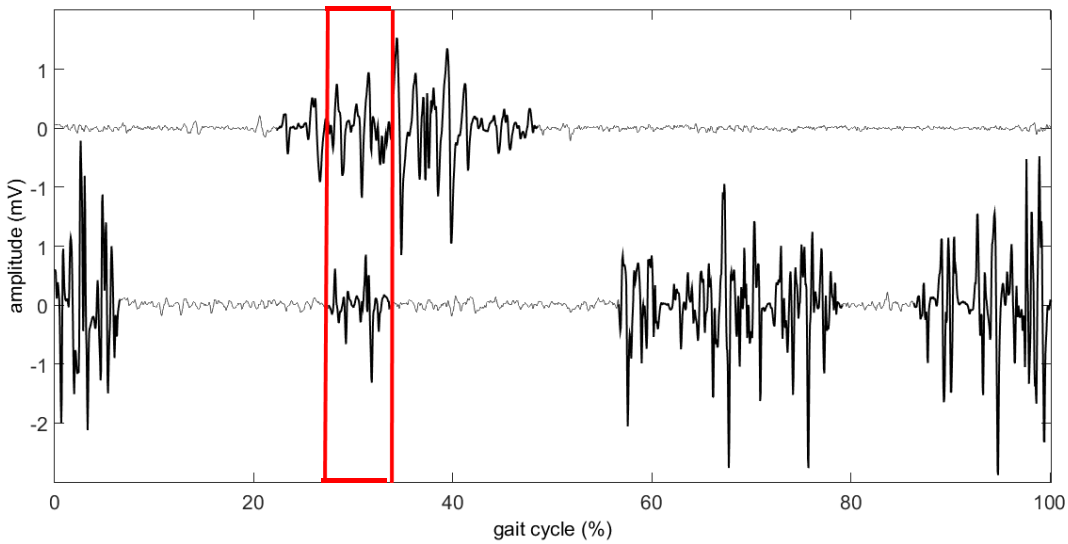

Fig. 1.9. Example of muscle co-contraction; the muscle co-contraction is highlighted by a red box. The first signal is gastrocnemius lateralis; the second one is the tibialis anterior.

Chapter references

[1] J. A. Rall, *Mechanism of muscular contraction*. 2014.

[2] S. L. Pullman, "Clinical utility of surface EMG," *Neurology*, 2000.

[3] L. M. Vaca Benitez, M. Tabie, N. Will, S. Schmidt, M. Jordan, and E. A. Kirchner, "Exoskeleton technology in rehabilitation: Towards an EMG-based orthosis system for upper limb neuromotor rehabilitation," *J. Robot.*, 2013.

[4] C. J. Heckman and R. M. Enoka, "Physiology of the motor neuron and the motor unit," *Handb. Clin. Neurophysiol.*, 2004.

[5] C. J. Heckman and R. M. Enoka, "Motor unit," *Compr. Physiol.*, 2012.

[6] G. E. Loeb and C. Ghez, "The motor unit and muscle action," in *Principles of Neural Science*, 2000.

[7] D. Stashuk, "EMG signal decomposition: How can it be accomplished and used?," *Journal of Electromyography and Kinesiology*. 2001.

[8] I. Rodriguez-Carreno, L. Gila-Useros, and A. Malanda-Trigueros, "Motor Unit Action Potential Duration: Measurement and Significance," in *Advances in Clinical Neurophysiology*, 2012.

[9] A. Fletcher, "Action potential: Generation and propagation," *Anaesth. Intensive Care Med.*, 2016.

[10] D. A. Rivas and R. A. Fielding, "Skeletal Muscle," in *Encyclopedia of Human Nutrition*, 2012.

[11] P. M. Hopkins, "Skeletal muscle physiology," *Contin. Educ. Anaesthesia, Crit. Care Pain*, 2006.

[12] "Skeletal Muscle," *The Journal of Physiology*. 1994.

[13] J. Squire, "The Structural Basis of Muscular Contraction," in *The Structural Basis of Muscular Contraction*, 1981.

[14] I. H. Hong and S. J. Etherington, "Neuromuscular Junction," in *Encyclopedia of Life Sciences*, 2011.

[15] S. Schiaffino and C. Reggiani, "Skeletal muscle fiber types," in *Muscle*, 2012.

[16] J. V Basmajian and C. J. De Luca, "Chapter 3: Description and analysis of the EMG Signal," in *Muscles Alive: their functions revealed by electromyography*, 1985.

[17] N. Nazmi, M. A. A. Rahman, S. I. Yamamoto, S. A. Ahmad, H. Zamzuri, and S. A. Mazlan, "A review of classification techniques of EMG signals during isotonic and isometric contractions," *Sensors (Switzerland)*. 2016.

[18] K. R. Mills, "The basics of electromyography," *Neurology in Practice*. 2005.

[19] G. D. Pope, "Introduction to Surface Electromyography," *Physiotherapy*, 1998.

[20] E. Criswell, *Cram's Introduction to Surface Electromyography*. 2011.

[21] D. L. Donoho and J. M. Johnstone, "Ideal spatial adaptation by wavelet shrinkage," *Biometrika*, 1994.

[22] M. B. I. Reaz, M. S. Hussain, and F. Mohd-Yasin, "Techniques of EMG signal analysis: detection, processing, classification and applications (Correction)," *Biol. Proced. Online*, vol. 8, no. 1, pp. 163–163, 2006.

[23] A. V H, "A Review on Noises in EMG Signal and its Removal," *Int. J. Sci. Res. Publ.*, 2017.

[24] R. H. Chowdhury, M. B. I. Reaz, M. A. Bin Mohd Ali, A. A. A. Bakar, K. Chellappan, and T. G. Chang, "Surface electromyography signal processing and classification techniques," *Sensors (Switzerland)*. 2013.

[25] M. Blanco-Velasco, F. Cruz-Roldán, E. Moreno-Martínez, J. I. Godino-Llorente, and K. E. Barner, "Embedded filter bank-based algorithm for ECG compression," *Signal Processing*, 2008.

[26] P. B. Patil and M. S. Chavan, "A wavelet based method for denoising of biomedical signal," in *International Conference on Pattern Recognition, Informatics and Medical Engineering, PRIME 2012*, 2012.

[27] D. L. Donoho and I. M. Johnstone, "Threshold selection for wavelet shrinkage of noisy data," in *Engineering in Medicine and Biology Society, 1994. Engineering Advances: New Opportunities for Biomedical Engineers. Proceedings of the 16th Annual International Conference of the IEEE*, 1994.

[28] S. J. Olney, "Quantitative evaluation of cocontraction of knee and ankle muscles in normal walking," in *Biomechanics IX: International Congress of Biomechanics*, 1983, vol. 9, pp. 431–436.

[29] R. Baratta, M. Solomonow, B. H. Zhou, D. Letson, R. Chuinard, and R. D'Ambrosia, "Muscular coactivation. The role of the antagonist musculature in maintaining knee stability.," *Am. J. Sports Med.*, 1988.

[30] A. R. Den Otter, A. C. H. Geurts, T. Mulder, and J. Duysens, "Gait recovery is not associated with changes in the temporal patterning of muscle activity during treadmill walking in patients with post-stroke hemiparesis," *Clin. Neurophysiol.*, 2006.

[31] P. Le, T. M. Best, S. N. Khan, E. Mendel, and W. S. Marras, "A review of methods to assess coactivation in the spine," *Journal of Electromyography and Kinesiology*. 2017.

[32] P. Bonato, T. D'Alessio, and M. Knaflitz, "A statistical method for the measurement of muscle activation intervals from surface myoelectric signal during gait," *IEEE Trans. Biomed. Eng.*, vol. 45, no. 3, pp. 287–299, 1998.

Chapter 2

GAIT ANALYSIS AND GAIT CYCLE

Walking can be defined as a method of locomotion involving the use of the legs, alternately, to provide both support and propulsion of the body [1][2]. Formally walking uses a repetitious sequence of limb motion to move the body forward while simultaneously maintaining stance stability [3]. During walking, the main functions carried out by the locomotor apparatus are:

• Generation of a propulsive force;

• Maintaining stability at the higher level, despite the continuous change in the posture situation;

• Shock absorption due to impact with the ground at every step;

• Preservation of energy during previous functions, to minimize the effort by the muscles.

Normal people initiate floor contact with their heel (i.e., heel strike).

The gait cycle (GC) is the time interval between the exact same repetitive events of walking that generally begin when one-foot contacts the ground. Each GC is divided into two periods, stance and swing also known as gait phases. Stance is the term used to designate the entire period during which the foot is on the ground. A stance phase starts with a heel contact and continues with sub-phases: initial contact, loading response, mid stance, terminal stance and pre-swing [3]. Instead, swing phase begins as the foot is lifted from the floor (toe-off). The separation of toes from the ground marks the beginning of swing phase which involves the following sub-phases: initial swing, mid-swing and terminal swing [3]. The stance phase usually lasts about 60% of the GC, the swing phase about 40% of the GC.

To provide the basic functions required for walking, each stride involves an ever-changing alignment between the body and the supporting foot during stance phase and selective advancement of the limb segments in swing phase [4]. These reactions result in a series of motion patterns performed by the hip, knee and ankle. Each stride contains eight functional patterns or sub-phases. The phases of GC also provide a means for correlating the simultaneous actions of the individual joints into patterns of total limb function. This is a particularly important approach for interpreting the functional effects of disability. Each of the eight gait phases has a functional objective. The sequential combination of the phases also enables the limb to accomplish three basic tasks: weight acceptance (WA), single limb support (SLS) and limb advancement (LA). Weight acceptance begins the stance period and uses the first two gait phases (initial contact and loading response). Single limb support continues stance with the next two phases of gait (mid stance and terminal stance). Limb advancement begins in the final phase of stance (pre-swing) and then continues through the three phases of swing (initial swing, mid swing and terminal swing). A representative scheme of GC and gait phase is reported in Fig. 2.1.

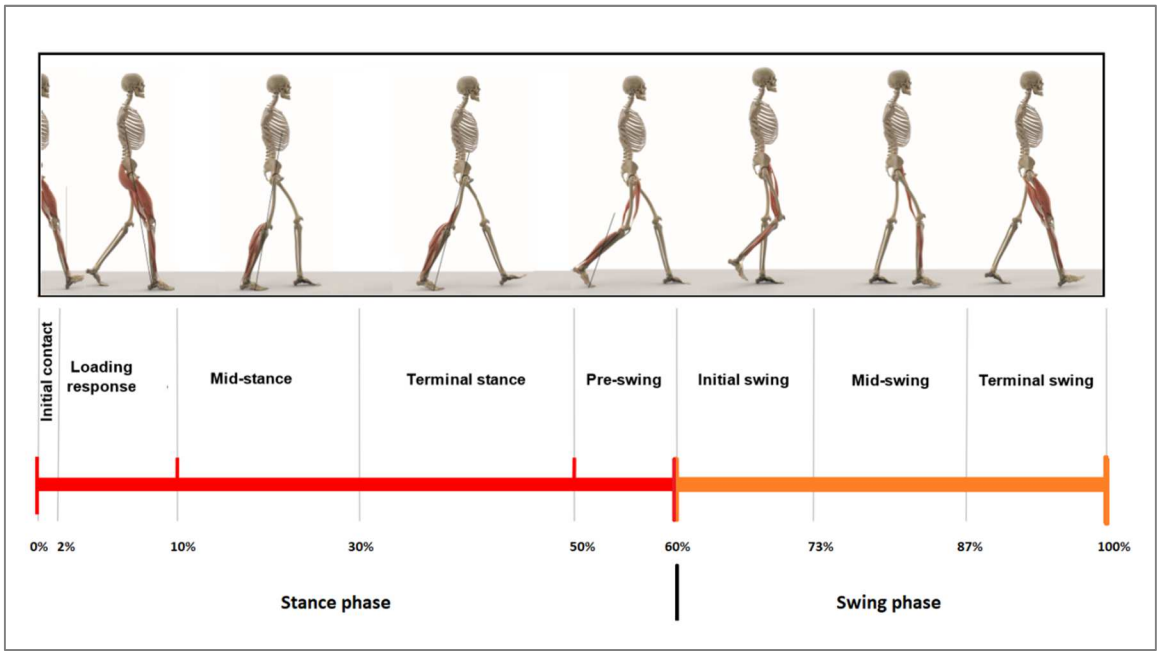

Fig. 2.1. A representative scheme of GC and gait phase.

2.1 Weight Acceptance

This is the most challenging task in the gait cycle. Three functional patterns are needed: shock absorption, initial limb stability and the preservation of progression. The challenge is the abrupt transfer of body weight on a limb that has just finished swinging forward and has an unstable alignment. In this task initial contact and loading response are involved.

Phase l-Initial Contact

The first sub-phase that involved weight acceptance function is initial contact. Initial contact, also known as Heel Strike, is a short period that begins the moment the foot touches the ground and is the first phase of double support. The ankle moves from a neutral position into plantar flexion. After this, knee flexion begins and increases. The plantar flexion is controlled by eccentric contraction of the tibialis anterior, extension of the knee is caused by a contraction of the quadriceps, flexion is caused by the contraction of the hamstring, and the flexion of the hip is caused by the contraction of the rectus femoris [3].

Phase 2-Loading Response

In loading response phase, the body weight is transferred on the forward limb. Using the heel as a rocker, the knee is flexed for shock absorption. Ankle plantar flexion limits the heel rocker by forefoot contact with the floor. The opposite limb (clear) is in its pre-swing phase. This is the initial double stance period. The phase begins with initial floor contact and continues until the other foot is lifted for swing [3].

2.2 Single Limb Support

Lifting the other foot for swing begins the single limb support interval for the stance limb. This continues until the opposite foot again contacts the floor. During the resulting interval, one limb has the total responsibility for supporting body weight in both the sagittal and coronal planes while

progression must be continued. Two phases are involved in single limb support: mid stance and terminal stance. They are differentiated primarily by their mechanisms of progression [3].

Phase 3-Mid Stance

In the first half of single limb support, the limb advances over the stationary foot by ankle dorsiflexion (ankle rocker) while the knee and hip extend. The opposite limb is advancing in its mid swing phase. This is the first half of the single limb support interval. It begins as the other foot is lifted and continues until body weight is aligned over the forefoot [3].

Phase 4- Terminal Stance

During the second half of single limb support, the heel rises and the limb advances over the forefoot rocker. The knee increases its extension and then just begins to flex slightly. Increased hip extension puts the limb in a more trailing position. The other limb is in terminal swing. This phase completes single limb support. It begins with heel rise and continues until the other foot strikes the ground. Throughout this phase body weight moves ahead of the forefoot [3].

2.3 Limb Advancement

To facilitate advancing of the limb, preparatory posturing begins in stance. Then the limb swings through three postures as it lifts itself, advances and prepares for the next stance interval. Four gait phases are involved: pre-swing (end of stance), initial swing, mid swing and terminal swing.

Phase 5-Pre-Swing

Floor contact by the other limb has started terminal double support. The reference limb responds with increased ankle plantar flexion. Greater knee flexion and loss of hip extension. The opposite limb is in Loading Response. This final phase of stance is the second (terminal) double stance interval in the gait cyc1e. It begins with initial contact of the opposite limb and ends with ipsilateral toe-off. This phase is also known as weight release and/or weight transfer phase. While the abrupt transfer of body weight promptly unloads the limb, this extremity makes no active contribution to the event. Instead, the

unloaded limb uses its freedom to prepare for the rapid demands of swing. All the motions and musc1e actions occurring currently relate to this latter task [3].

Phase 6-lnitial Swing

The foot is lifted, and limb advanced by hip flexion and increased knee flexion. The ankle only partially dorsiflexes. The other limb is in early mid stance. This first phase is approximately one-third of the swing period. It begins with lift of the foot from the floor and ends when the swinging foot is opposite the stance foot [3].

Phase 7-Mid Swing

Advancement of the limb anterior to the body weight line is gained by further hip flexion. The knee is allowed to extend in response to gravity while the ankle continues dorsiflexing to neutral. The other limb is in late mid stance. This second phase of the swing period begins as the swinging limb is opposite the stance limb. The phase ends when the swinging limb is forward, and the tibia is vertical (i.e., hip and knee flexion postures are equal) [3].

Phase 8- Terminal Swing

Limb advancement is completed by knee flexion. The hip maintains its earlier flexion. And the ankle remains dorsiflexed to neutral. The other limb (clear) is in terminal stance. This final phase of swing begins with a vertical tibia and ends when the foot strikes the floor. Limb advancement is completed as the leg (shank) moves ahead of the thigh [3].

Chapter references

[1] T. P. Andriacchi, J. A. Ogle, and J. O. Galante, "Walking speed as a basis for normal and abnormal gait measurements," *J. Biomech.*, 1977.

[2] J. G. G. Jessica Rose, *Human walking*. 2007.

[3] J. Perry, *Gait Analysis: Normal and Pathological Function*, vol. 12. 1992.

[4] C. BenAbdelkader, R. Cutler, and L. Davis, "Stride and cadence as a biometric in automatic person identification and verification," in *Proceedings - 5th IEEE International Conference on Automatic Face Gesture Recognition, FGR 2002*, 2002.

Chapter 3

ANATOMY AND PHISIOLOGY OF THE MAIN LOWER LIMB MUSCLES

The leg is the anatomical region of the human body between the thigh and the foot [1]. Articulation is at the border between the thigh and the leg and at the border between the leg and the foot. In the first case, it is the articulation of the knee; in the second case, instead, is the articulation of the ankle. The majority of muscles in the leg are considered long muscles, in that they stretch great distances. As these muscles contract and relax, they move skeletal bones to create movement of the body. Smaller muscles help the larger muscles, stabilize joints, help rotate joints, and facilitate other fine-tuned movements. The leg is characterized by thirteen muscles: six flexors, two extensors, two adductors and three abductors [2]. They contribute to fundamental movements for locomotion: plantarflexion, dorsiflexion, extension of the leg and toes, flexion of the leg and toes, foot eversion and inversion of the foot. Plantarflexion is the movement that allows you to point your foot towards the floor. The dorsiflexion, however, is the movement that allows you to lift the foot and walk on the heels. The flexion movement of the leg means reducing the posterior angle, existing between the leg and the thigh. On the other hand, making an extension movement means increasing the posterior angle between the leg and the thigh. The knee joint is decisively involved in the adjustment of the two movements. The knee allows the flexion of the leg backwards and its extension until it is in axis with the thigh (point of maximum extension). Flexing the toes means bending them towards the sole of the foot (or down); vice versa, extending the toes means to bend them upwards as far as possible. Perform an eversion gesture with the foot, it means to raise the lateral edge of the latter and hold,

instead, the medial edge on the floor. On the contrary, performing an inversion gesture with the foot, means lifting the medial edge of the latter and maintaining, on the opposite of the previous case, the lateral edge on the floor.

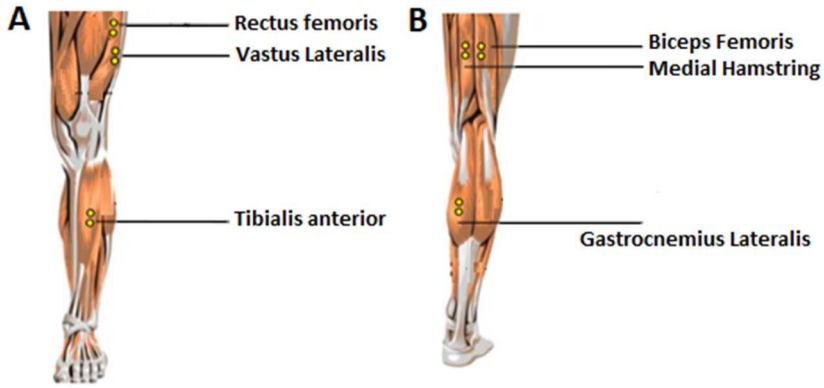

Fig. 3.1. Leg muscle. Upper muscle (A) and lower muscle (B).

3.1 Tibialis anterior

The tibialis anterior (TA) muscle is a long, narrow muscle of the lower leg (Fig. 3.1, A). It origins along the lateral condyle and proximal body of the tibia and runs down the shin just lateral to the tibia. Across the ankle, the muscular body of TA ends and its long tendon extends across the medial side of the ankle and into the foot. In the foot, the tendon forms insertions on the first metatarsal and first cuneiform bones [3]. The tibialis anterior functions as a dorsiflexor of the foot by pulling the top, or dorsum, of the foot towards the shin. Dorsiflexion results in the lifting of the toes off the ground, which is an important motion during walking and running to prevent tripping over one's toes. The tibialis anterior also provides a slight inversion of the foot by pulling the plantar surface of the foot toward the body's midline. This motion is important in balancing the body's weight on the foot during locomotion or standing and is especially important when standing on one foot [4]. The timing activation of TA [4] is reported in Fig. 3.2.

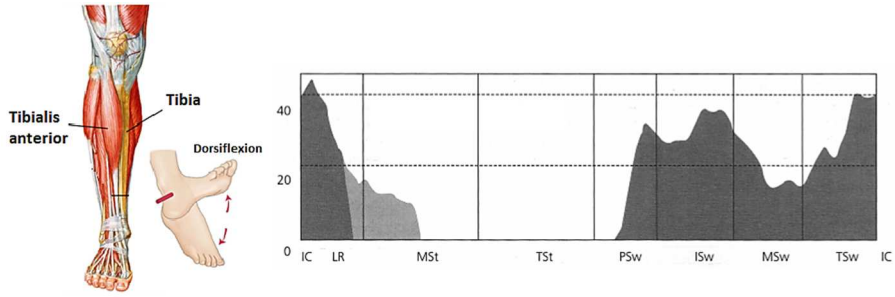

Fig. 3.2. Anatomy and physiology of TA; timing activation of TA.

3.2 Gastrocnemius Lateralis

The gastrocnemius is the most superficial muscles of the leg posterior region and it is characterized by the lateral and medial head, named respectively gastrocnemius lateralis (GL) and medialis (Fig. 3,1, B). The lateral head originates above the lateral epicondyle of the femur, from the popliteal plane and from the articular capsule of the knee. The far end of this muscle joins the strong Achilles tendon, which descends to the heel and attaches to the calcaneus [5]. The gastrocnemius is a powerful plantar flexor of the foot, that aids in pushing the body forward when a person walks or runs. It also works to flex the leg at the knee [4]. The timing activation of GL [4] is reported in Fig. 3.3.

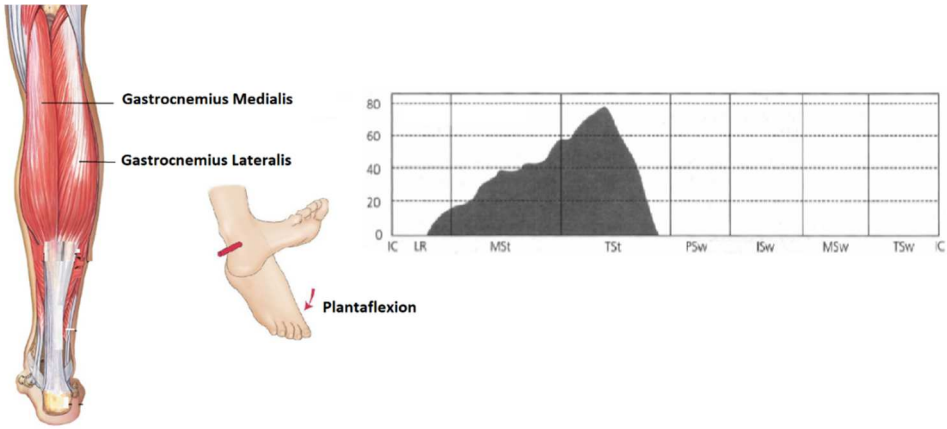

Fig. 3.3. Anatomy and physiology of GL; timing activation of GL.

3.3 Quadriceps femoris

Quadriceps femoris (QF) muscle occupies the front and sides of the thigh and is primary extensor of the knee. It is composed of four parts - rectus femoris, vastus lateralis, vastus medialis, and vastus intermedius (Fig. 3.1, B). These parts connect the ilium and femur to a common patellar tendon, which passes over the front of the knee and attaches to the patella (knee cap). This tendon then continues as the patellar ligament to the tibia (lower leg bone).

3.4 Rectus femoris

The Rectus femoris (RF) muscle is one of the four quadriceps muscles (Fig. 3.1, A). It is located in the middle of the front of the thigh. It is responsible for knee extension and hip and thigh flexion. It is the main muscle that can flex the hip. The rectus femoris attaches from the pelvis to just below the knee (on the patellar tendon.) The other muscles of the quadriceps include the vastus medialis, the vastus intermedius, and the vastus lateralis. The rectus femoris muscle has two heads. The straight head has its origin on the anterior inferior iliac spine. The reflected head has its origin on the ilium, above the acetabulum. It has its insertion into the patellar tendon at the patella of the knee. It is fed by a descending branch of the lateral femoral circumflex artery. It is enervated by the femoral nerve. The timing activation of RF [4] is reported in Fig. 3.4.

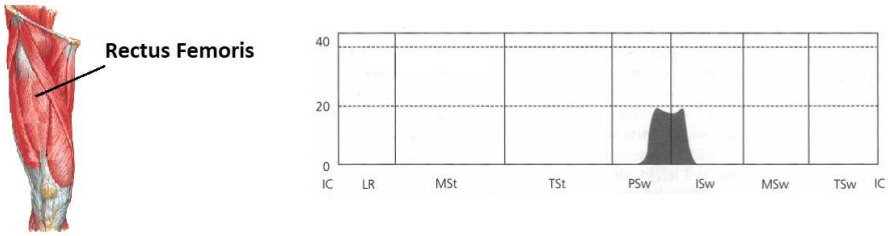

Fig. 3.4. Anatomy of RF; timing activation of RF.

3.5 Medial hamstrings

The hamstrings are a group of muscles and their tendons at the rear of the upper leg (Fig. 3.1, B). They include the biceps femoris, semitendinosus, and semimembranosus. The hamstrings flex the knee joint, adduct the leg, and extend the thigh to the backside of the body. The hamstring muscles have their origin, where their tendons attach to bone, at the ischial tuberosity of the hip (often called the sitting bones) and the linea aspera of the femur. The hamstring tendons flank the space behind the knee. The most medial muscle, the semimembranosus, inserts on the medial condyle of the tibia bone. The semitendinosus inserts on the superior part of the medial tibia. The most lateral hamstring, the biceps femoris, inserts on the lateral side of the fibula. They are innervated by the sciatic nerve. Hamstrings flex the knee and extend the hip.at the beginning of each step. During walking, they are antagonists to the quadriceps muscles in the action of deceleration of knee extension [6]. The timing activation of hamstrings [4] is reported in Fig. 3.5.

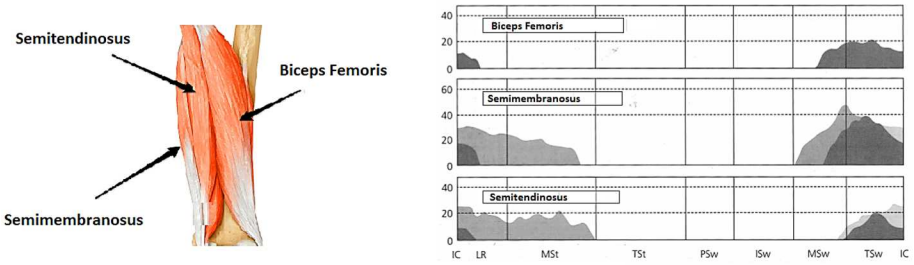

Fig. 3.5. Anatomy and timing activation of hamstrings.

3.6 Vastus Lateralis

The vastus lateralis (VL) muscle is located on the side of the thigh (Fig. 3.1, A). This muscle is the largest of the quadriceps group which also includes the rectus femoris, the vastus intermedius, and the vastus medialis. Collectively, the quadriceps muscle is the largest in the human body and its purpose is to extend the knee. It origins from superior portion of intertrochanteric line, anterior and inferior borders of greater trochanter, superior portion of lateral lip of linea aspera, and lateral portion

of gluteal tuberosity of femur. The specific task of the vastus lateralis muscle is to extend the lower leg and it is involved in knee extension, along with the other muscles which make up the quadriceps muscle. The timing activation of VL [4] is reported in Fig. 3.6.

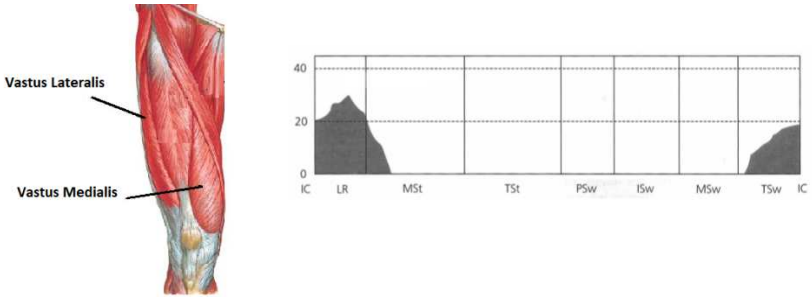

Fig. 3.6. Anatomy and timing activation of VL.

Chapter references

[1] P. Coales, "Principles of Anatomy and Physiology," *Physiotherapy*, 2000.

[2] D. A. Rivas and R. A. Fielding, "Skeletal Muscle," in *Encyclopedia of Human Nutrition*, 2012.

[3] A. V. D'Antoni, *Gray's Anatomy. The Anatomical basis of clinical practice.* 2016.

[4] J. Perry, *Gait Analysis: Normal and Pathological Function*, vol. 12. 1992.

[5] P. L. Williams, L. H. Bannister, M. M. Berry, P. Collins, M. Dyson, J. E. Dussek, and M. W. J. Ferguson, "Gray's anatomy," *Soames, R.W*, vol. p, p. 612, 1995.

[6] E. Kellis, "Quantification of quadriceps and hamstring antagonist activity," *Sport. Med.*, vol. 25, no. 1, pp. 37–62, 1998.

Part 1

Chapter 4

WAVELET TRANSFORM

Experimental data frequently appear as a time series. In order to be characterized, time signals are often transformed in frequency domain to describe their spectral content. A fundamental method for signal processing is the Fourier transform (FT). However, the Fourier analysis is useful for stationary system i.e. the frequency spectrum is correctly correlated only with a temporally invariant physical system. Moreover, the time-evolution of the frequencies is not provided by the FT. Thus, in the recent past, to overcame FT limitations, time-scale, or better time-frequency, methods have been used for the analysis of nonstationary signals. In particular, the wavelet transform (WT) is a powerful mathematical tool for analysis and synthesis of signals and has found successful applications in a remarkable diversity of disciplines such as physics, geophysics, numerical analysis, statistics and signal processing, in particular biomedical signal processing. This recent approach is able to perform a local analysis, revealing signal aspects that other analysis techniques miss, such as trends, breakdown points, discontinuities, etc, for non-stationary signals. Moreover, WT is a time-frequency analysis method which provides a good localized information in time and frequency domain simultaneously [1]. The one-dimensional time series data are decomposed into a time-frequency plane allowing to determine the temporal evolution of the signal spectral content i.e. both spectral modes and how those modes vary in time. WT is an alternative to the classical windowed Fourier analysis, providing not only the representation of the spectral energy content of the signal at a certain time, but also the ability to adapt the resolution to the signal frequency. Moreover, a wavelet is a localized function that can be used to capture informative, efficient, and useful descriptions of a signal. If the signal is

represented as a function of time, then wavelets provide efficient localization in both time and either frequency or scale [1].

4.1 Continuous Wavelet Transform

Continuous Wavelet Transform (CWT) is a flexible approach to signal decomposition [1]. CWT is a time-frequency analysis method that quantifies temporal changes of frequency content of non-stationary signals, without losing resolution in time or frequency.

CWT of a function *x(t)* is defined by the sum over all time of *x(t)* (Eq.1), with a dilated as well as shifted versions of a single function $\psi_{a,b}(t) \in L_2(\mathbb{R})$[1]:

$$CWT(a,b) = X_\psi(a,b) = \int_{-\infty}^{\infty} x(t)\psi^*_{a,b}(t)dt \quad (1)$$

where $\psi^*_{a,b}(t)$ is the complex conjugate of the wavelet $\psi_{a,b}(t)$.

From the definition, the wavelet transform gives the inner product between the function *x(t)* and wavelet $\psi_{a,b}(t)$. Since $\psi_{a,b}(t)$ is only non-vanishing in the neighborhood of *b*, $X_\psi(a,b)$ gives the local information of *x(t)* around *t*. Furthermore, $X_\psi(a,b)$ measures the similarity between function *x(t)* around *b* and $\psi_a(t)$, the mother wavelet scaled by *a* (Eq.2):

$$\psi_a(t) \stackrel{\text{def}}{=} \psi_{a,0} = \frac{1}{\sqrt{a}}\psi\left(\frac{t}{a}\right) \quad (2)$$

where *a* is the scale parameter and *b* the translation parameter.

From Eq. (1) and Eq. (2), the follow equation can be derived (Eq.3):

$$\psi_{a,b}(t) = \psi_a(t-b) \quad (3)$$

[1] $L_2(\mathbb{R})$ is the set of complex valued functions which satisfy $\int_{-\infty}^{+\infty}|\psi(t)|^2\,dt < \infty$.

Using $\psi_a(t)$ instead of $\psi_{a,b}(t)$, Eq. (1) can be rewritten as (by substituting t with t + u) (Eq. 4):

$$X_\psi(a,b) = \int_{-\infty}^{\infty} x(t+b)\psi_a^*(t)dt \tag{4}$$

Another way to view the CWT when the mother wavelet is a symmetric, real-valued function is showed in the following equation (Eq. 5).

$$\begin{aligned} X_\psi(a,b) &= \int_{-\infty}^{\infty} x(t)\psi_{a,b}^*(t)dt \\ &= \int_{-\infty}^{\infty} x(t)\psi_a(t-b)dt \\ &= \int_{-\infty}^{\infty} x(t)\psi_a(b-t)dt \\ &= (x * \psi_a)(u) \end{aligned} \tag{5}$$

From Eq. (5), CWT can also be viewed as a convolution between the function *x(t)* and scaled mother wavelet $\psi_a(t)$, when the mother wavelet is a symmetric, real-valued function. The results of $X_\psi(a,b)$ are called wavelet coefficients; each wavelet coefficient is associated to a scale (frequency) and a point in the time domain. The WT also has an inverse transformation. The inverse continuous wavelet transformation (ICWT) is defined by (Eq. 6):

$$x(t) = \frac{1}{C_\psi^2} \int_{-\infty}^{\infty}\int_{-\infty}^{\infty} X_\psi(a,b)\ \frac{1}{s^2}\ \psi\left(\frac{t-b}{a}\right) dbda \tag{6}$$

The admissibility constant C_ψ must satisfy the second wavelet condition. A wavelet function has its own central frequency *fc* at each scale, the scale *a* is inversely proportional to that frequency. A large scale corresponds to a low frequency, giving global information of the signal. Small scales correspond to high frequencies, providing detail signal information. For the WT, the Heisenberg inequality still holds, the bandwidth-time product $\Delta t \Delta f$ is constant and lower bounded. Decreasing the scale *a*, i.e. a shorter window, will increase the time resolution Δt, resulting in a decreasing frequency resolution Δf. This implies that the frequency resolution Δf is proportional to the frequency f, i.e. wavelet

analysis has a constant relative frequency resolution [2]. The calculation of the CWT is usually performed by taking discrete values for the scaling parameter *a* and translation parameter *b*. The resulting wavelet coefficients are called wavelet series. The constant relative frequency resolution of the wavelet analysis is also known as the constant Q property. Q is the quality factor of the filter, defined as the center-frequency *fc* divided by the bandwidth *fb* [1]. For a constant Q analysis (constant relative frequency resolution), a dyadic sample-grid for the scaling seems suitable [1]. A dyadic grid discretizes the scale parameter on a logarithmic scale. The time parameter is discretized with respect to the scale parameter. The dyadic grid is one of the simplest and efficient discretization methods for practical purposes and leads to the construction of an orthonormal wavelet basis [1].

4.2 Mother Wavelet

A wavelet function ψ(t) or mother wavelet is a small wave, which must be oscillatory in some way to discriminate between different frequencies [3]. The wavelet contains both the analysing shape and the window. For the CWT several kinds of wavelet functions are developed which all have specific properties.

An analysing function ψ(t) is classified as a wavelet if the following mathematical criteria are satisfied [1] (Eq. 7):

1. A wavelet must have finite energy (Eq.7)

$$E = \int_{-\infty}^{\infty} |\psi(t)|^2 dt < \infty \tag{7}$$

   The energy E equals the integrated squared magnitude of the analysing function ψ(t) and must be less than infinity.

2. If Ψ(f) is the Fourier transform of the wavelet ψ(t), the following condition must hold (Eq.8)

$$C_\psi = \int_0^{\infty} \frac{|\widehat{\psi}(f)|^2}{f} df < \infty \tag{8}$$

This condition implies that the wavelet has no zero frequency component ($\Psi(0) = 0$), i.e. the mean of the wavelet ψ(t) must equal zero. This condition is known as the admissibility constant. The value of $C\psi$ depends on the chosen wavelet.

3. For complex wavelets the Fourier transform Ψ(f) must be both real and vanish for negative frequencies.

A mother wavelet $\psi(t)$ has the following two properties (Eq. 9, Eq. 10):

$$\int_{-\infty}^{\infty} |\psi(t)|^2 dt = 1 \tag{9}$$

$$\int_{-\infty}^{\infty} \psi(t) dt = 0 \tag{10}$$

For a mother wavelet: $\psi(t)$, the wavelet with scale *a* and translation *b* is (Eq. 11):

$$\psi_{a,b}(t) = \frac{1}{\sqrt{a}} \psi\left(\frac{t-b}{a}\right) \tag{11}$$

Eq.11 indicates that the wavelet becomes wider (has larger support) as scale *a* increases, and narrower (smaller support) as scale *a* decreases. The signal energy is normalized at every scale by dividing the wavelet coefficients by $1/\sqrt{a}$ | [2]. This ensures that the wavelets have the same energy at every scale. The mother wavelet is contracted and dilated by changing the scale parameter *a* (Fig. 4.1). The variation in scale *a* changes not only the central frequency *fc* of the wavelet, but also the window length. Therefore, the scale *a* is used instead of the frequency for representing the results of the wavelet analysis. The translation parameter *b* specifies the location of the wavelet in time, by changing *b* the wavelet can be shifted over the signal. For constant scale *a* and varying translation *b* the rows of the time-scale plane are filled, varying the scale a and keeping the translation b constant fills the columns of the time-scale plane. As reported in Fig. 4.1, for a < 1, the dilated Wavelet function contracts in time and for a > 1, the dilated Wavelet expands in time [2].

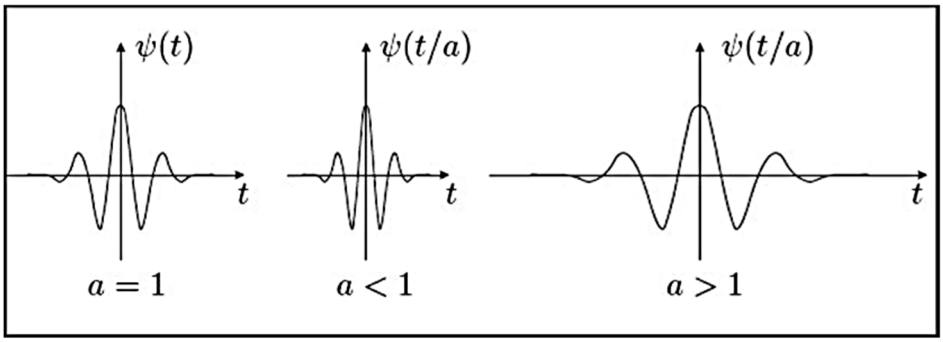

Fig. 4.1. Effect of changing the scale parameter a.

The wavelet basis function is chosen according to the application to be analysed. In choosing the wavelet function, there are several factors which should be considered.

1) Complex or real. A complex wavelet function will return information about both amplitude and phase and is better adapted for capturing oscillatory behaviour. A real wavelet function returns only a single component and can be used to isolate peaks or discontinuities.

2) Width. The width of a wavelet function is defined here as the wavelet amplitude in time domain. The resolution of a wavelet function is determined by the balance between the width in real space and the width in Fourier space. A narrow (in time) function will have good time resolution but poor frequency resolution, while a broad function will have poor time resolution, yet good frequency resolution.

3) Shape. The main idea of WT analysis is to measure the degree of similarity between the original signal and the basis function, or mother wavelet, of the WT. This similarity is found by the computation of WT coefficients. Thus, the main criteria are related to the shape of the mother Wavelet, which should be similar to the shape of the analysed biomedical signals, and to the suitability for detecting signal changes.

4.2.1 Wavelet function families

For the WT analysis, special families of wavelet functions were developed. These wavelets are compactly supported, orthogonal or biorthogonal and are characterized by low-pass and high-pass analysis and synthesis filters.

Following the criteria above mentioned, the two main wavelet function families used, in this work, for biomedical signal analysis are Daubechies and Coiflets families.

The Daubechies family, named by Ingrid Daubechies, are compactly supported orthogonal wavelets [4]. The order of the Daubechies functions denotes the number of vanishing moments, or the number of zero moments of the wavelet function. This is related to the number of oscillations of the wavelet function. The larger the number of vanishing moments, the better the frequency localization of the decomposition. The dependence between wavelet coefficients on different scales decays with increasing wavelet order. The scaling filters are minimum-phase filters. The wavelet functions for the Daubechies functions with order 1 up to 10 are reported in Fig. 4.2:

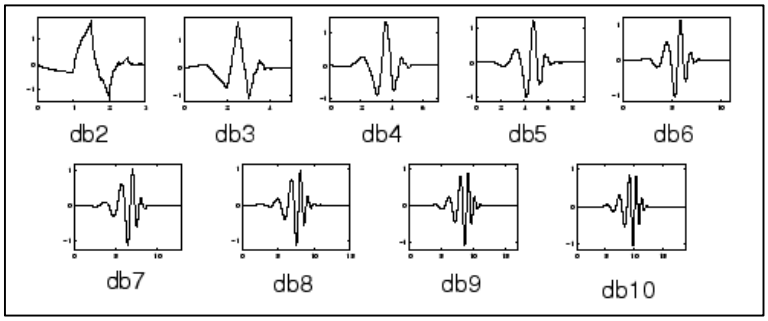

Fig. 4.2. Daubechies family.

Instead, Coiflets wavelets, built by I. Daubechies on the request of R. Coifman, are orthogonal compactly supported wavelets with the highest number of vanishing moments for both the wavelet and scaling function for a given support width [4]. The Coiflet wavelets are more symmetric and have more vanishing moments than the Daubechies wavelets. The wavelet functions for the Coiflets functions with order 1 up to 5 are shown in respectively Fig. 4.3.

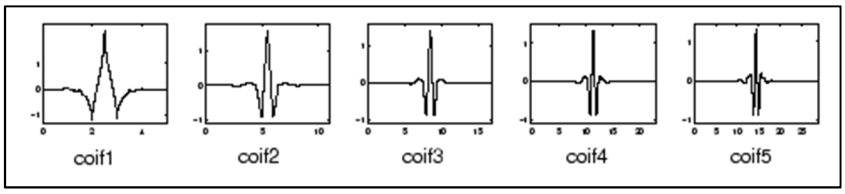

Fig. 4.3. Coiflets family.

For sEMG signal analysis, mother Wavelet Daubechies of order 4 has been chosen [5]; instead mother Wavelet Coiflets of order 4 has been selected for fetal phonocardiographic signal (fPCG) analysis [6].

4.3 Discrete wavelet transform

The CWT performs a multiresolution analysis by contraction and dilatation of the wavelet functions. The discrete wavelet transform (DWT) uses multiresolution filter banks and special wavelet filters for the analysis and reconstruction of signals [7].

4.3.1 Filter banks

A filter bank consists of filters which separate a signal into frequency bands [8]. An example of a two channel filter bank is shown in Fig. 4.4. A discrete time signal $x(k)$ enters the analysis bank and is filtered by the filters L(z) and H(z), respectively a low-pass and a high-pass filter, which separate the frequency content of the input signal in frequency bands of equal width. The output of the filters each contain half the frequency content, but an equal number of samples as the input signal. The filtered signals $c_l(k)$ and $c_h(k)$ are the output of filters L(z) and H(z) application, respectively. The two outputs together contain the same frequency content as the input signal, however the amount of data is doubled. Therefore, down-sampling by a factor two, denoted by ↓2, is applied to the outputs of the filters in the analysis bank. Reconstruction of the original signal is possible using the synthesis filter bank [8]. In the synthesis bank the signals are up-sampled (↑ 2) and passed through the filters L0(z) and H0(z). The filters in the synthesis bank are based on the filters in the analysis bank. The outputs of the filters in the synthesis bank are summed, leading to the reconstructed signal $y(k)$. The

different output signals of the analysis filter bank are called subbands, the filter-bank technique is also called subband coding [9].

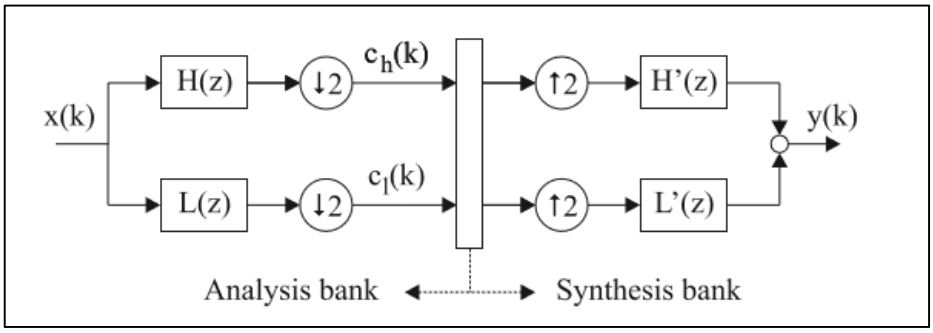

Fig. 4.4. Two channel filter banks.

4.3.2 Down- and up-sampling

The low- and high-pass filters L(z) and H(z) split the frequency content of the signal in half. If half of the samples of the filtered signals $c_l(k)$ and $c_h(k)$ are reduced, it is still possible to reconstruct the signal $x(k)$. The down-sampling operation (↓2) saves only the even-numbered components of the filter output, hence it is not invertible. In the synthesis bank the signals are first up-sampled before filtering. The up-sampling by a factor two (↑2) is performed by adding zeros in between the samples of the original signal. The first down-sampling of a signal and then up-sampling of it will not return the original signal. The transpose of (↓2) is (↑2). Since transposes come in reverse order, synthesis can be performed as the transpose of the analysis. Furthermore (↓ 2) (↑ 2) = I, since (↑ 2) is the right-inverse of (↓ 2). This indicates that it is possible to obtain the original signal again with up- and down-sampling. By first inserting zeros and then removing them, the original signal is obtained again. For perfect reconstruction to be possible, the filter bank should be biorthogonal. Furthermore, some design criteria for both the analysis and synthesis filters should be met to prevent aliasing and distortion and to guarantee a perfect reconstruction [10].

4.3.3 Multiresolution filter banks

The CWT performs a multiresolution analysis which makes it possible to analyse a signal at different frequencies with different resolutions. For high frequencies (low scales), which last a short period of time, a good time resolution is desired. For low frequencies (high scales) a good frequency resolution is more important. The multiresolution of CWT can also be obtained using filter banks, resulting in the discrete wavelet transform (DWT). The low-pass and high-pass filtering branches of the filter bank retrieve respectively the approximations and details of the signal *x(k)*. In Fig. 4.5, a three level filter bank is shown. The filter bank can be expanded to an arbitrary level, depending on the desired resolution. The coefficients *cl(k)* represent the lowest half of the frequencies in x(k), down-sampling doubles the frequency resolution. The time resolution is halved, i.e. only half the number of samples are present in *cl(k)*. In the second level, the outputs of L(z) and H(z) double the time resolution and decrease the frequency content, i.e. the width of the window is increased. After each level, the output of the high-pass filter represents the highest half of the frequency content of the low-pass filter of the previous level, this leads to a pass-band. For a special set of filters L(z) and H(z) this structure is called the DWT, the filters are called wavelet filters.

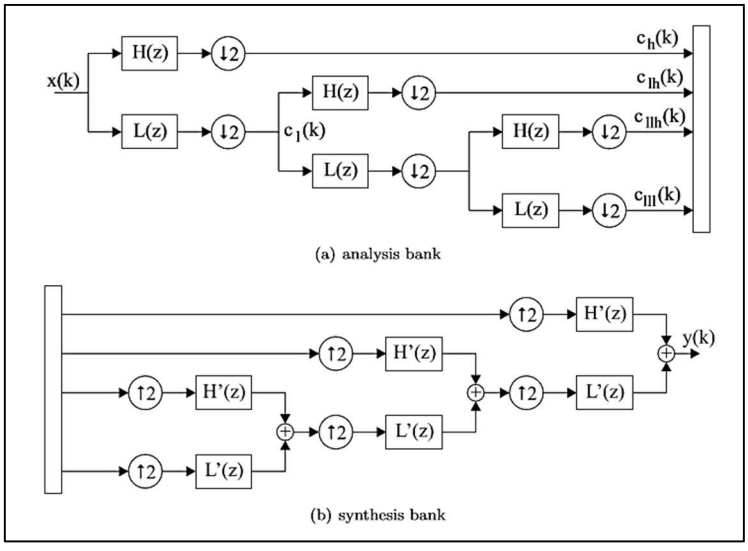

Fig. 4.5. Example of three level filter banks.

4.3.4 Wavelet filters

The wavelets in the CWT have a center frequency and act as a band-pass filter in the convolution of the wavelet function with the signal *x(k)*. The sequence of low-pass filter, down-sampling and high-pass filter also acts as a band-pass filter. In order to facilitate the comparison between the DWT and CWT, the filter bank of Fig. 4.5 is rewritten to Fig. 4.6. An increase in down-sampling rate leads to a larger time grid for lower frequencies (higher scales). The filters can be interpreted as the wavelet functions at different scales. However, they are not exact scaled versions of each other, if the number of levels is increased and the impulse responses of the equivalent filters converge to a stable waveform, the filters L(z) and H(z) are wavelet filters [4]. The subsequent filters then become scaled versions of each other. The wavelet filters represent the frequency content of a wavelet function at a specific scale.

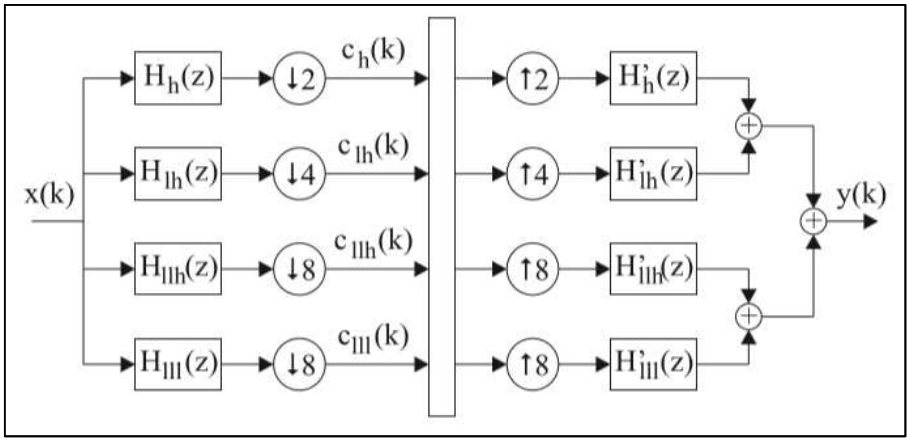

Fig. 4.6. Equivalent of three level filter banks, from CWT to DWT analysis.

The subband with wavelet coefficients c_{lll} is called the approximation subband *cA* and contains the lowest frequencies. The other subbands are called detail subbands *cD* and give the detail information of the signal. The wavelet coefficients represent the signal content in the various frequency bands. For a *p*-level decomposition, the highest frequency observed in the approximation wavelet coefficients c_{lll} can be calculated as a function of the sample frequency *fs* as (Eq. 12):

$$f_l = \frac{f_s}{2^{p+1}} \tag{12}$$

The frequency content of the approximation frequency band *cA* and detail frequency bands *cD* can be calculated as (Eq. 13 and Eq. 14, respectively):

$$f_{cA} = [0,\ 2^{-p-1} f_s] \tag{13}$$

$$f_{cDp} = [2^{-p-1} f_s,\ 2^{-p} f_s] \tag{14}$$

Thus, the success of a certain decomposition depends strongly on the chosen wavelet filters, depending on the signal properties. Also, there exists a trade-off between the order of the wavelets and the computation time. Higher order wavelets are smoother and are better able to distinguish between the various frequencies but require more computation time.

4.4 Wavelet denoising algorithm

A possible application of the discrete wavelet analysis is to remove undesired components (noise) from the signal through a denoising approach. Basically, the procedure includes decomposing the signal into the detail components, identifying the noise components and reconstructing the signal without those components. This is called the linear denoising approach. The linear denoising approach assumes that the noise can be found within certain scales, for example, at the finest scales when the coarsest scales are assumed to be noise free. More advanced denoising technique can be done by applying the non-linear thresholding approach, which involves discarding the details exceeding a certain limit. This approach assumes that every wavelet coefficient contain noise and it is distributed over all scales. The non-linear de-noising can be performed using different two types of thresholding methods, soft and/or hard, or a universal threshold [11]. The non-linear denoising algorithm uses statistical regression of noisy coefficients over time to obtain a non-parametric estimation of the reconstructed signal without noise.

The denoising of signal is performed by discrete wavelet transform (DWT) and a threshold method. The DWT and threshold-based denoising are implemented using MATLAB Wavelet toolbox. The flow chart of the algorithm denoising is showed in Fig 4.7.

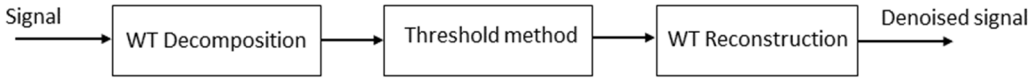

Fig. 4.7. Wavelet denoising algorithm.

4.4.1 Threshold Method

Suppose the following equation represents a simple model of the EMG or a biomedical signal (Eq. 15),

$$f(t) = s(t) + n(t) \tag{15}$$

where, s(t), n(t) denotes EMG signals and White Gaussian Noise N (0, σ^2), respectively. The energy of the original signal s(t) is effectively captured, to a high percentage, by transform values whose magnitude are all greater than a threshold, Ts >0. The noise signal's transform values all have the magnitudes while lie below a noise threshold Tn satisfy Tn < Ts. Then, the noise in f(t) can be removed by thresholding its transform. All values of its transform whose magnitude lies below the noise threshold Tn are set equal to 0.

The procedure of wavelet denoising is composed of three steps.

1. Decomposition. The DWT decomposes a signal into several multiresolution components according to a basic function or wavelet function, for a number of level *j*. The resolution of the signal, which is a measure of the amount of detail information in the signal, is determined by the filtering operations, and the scale is determined by up-sampling and down-sampling operations. The DWT is computed by successive low-pass and high-pass filtering of the discrete time-domain signal. This first step requires the choice of the mother wavelet and the level of decomposition j. The details *cDj* and approximation *cAj* coefficients for each level *j* are obtained by the multi-resolution analysis [7].

2. Thresholding. Coefficients with small magnitude can be considered as pure noise and should be set to zero. The wavelet thresholding consists in a comparison between each coefficient and a threshold in order to decide whether it constitute a desirable part of the information content of the original signal or not. The thresholding of the wavelet coefficients is usually applied only to the detail coefficients of a signal rather than to the approximation coefficients, since the latter ones represent 'low-frequency', that usually contain important components of the signal, and are less affected by the noise. The thresholding extracts the significant coefficients by setting to zero the coefficients which their absolute value is below a certain threshold level, which is to be denoted by λ. For each level of decomposition, the detail coefficients are compared with a level of threshold λ, then the signal is suppressed or transformed if it is smaller than the threshold. This second step requires the choice of the thresholds and the transformation function for the different levels of decomposition. The threshold method is applied as followed:

a) The energy of the original signal s is effectively captured, to a high percentage, by transform values whose magnitude are all greater than a threshold, Ts >0.

b) The noise signal's transform values all have the magnitudes while lie below a noise threshold Tn satisfy Tn < Ts.

Then the noise can be removed by thresholding its transform. All values of its transform whose magnitude lies below the noise threshold Tn are set equal to 0.

The selection of the threshold is of paramount importance in the Wavelet denoising algorithm. The thresholded wavelet coefficients are obtained using two different thresholding rule, hard or soft thresholding rule [12], [13] or a universal threshold [11].

In hard thresholding $\hat{Y}_{j,k}^{hard}$, the Wavelet coefficients with absolute values below or at the threshold level (λ) are affected only and they are replaced by zero value whereas others are kept unchanged, as reported in the Eq. 16. Hard thresholding maintains the scale of the

signal but introduces ringing and artifacts after reconstruction due to a discontinuity in the Wavelet coefficients.

$$\widehat{Y}_{j,k}^{hard} = \begin{cases} Y_{j,k} & for\ |Y_{j,k}| > \lambda \\ 0 & for\ |Y_{j,k}| \leq \lambda \end{cases} \tag{16}$$

In soft thresholding $\hat{Y}_{j,k}^{soft}$, coefficients above threshold level (λ) are also modified; they are reduced by particular value of the threshold, as reported in the Eq. 17. Soft thresholding eliminates this discontinuity resulting in smoother signals but decreases the magnitude of the reconstructed signal.

$$\hat{Y}_{j,k}^{soft} = \begin{cases} Y_{j,k} - \lambda & for\ Y_{j,k} \geq \lambda \\ 0 & for\ |Y_{j,k}| < \lambda \\ Y_{j,k} + \lambda & for\ Y_{j,k} \leq -\lambda \end{cases} \tag{17}$$

The shapes of hard (a) and soft (b) thresholding operators are illustrated in Fig. 4.8, respectively.

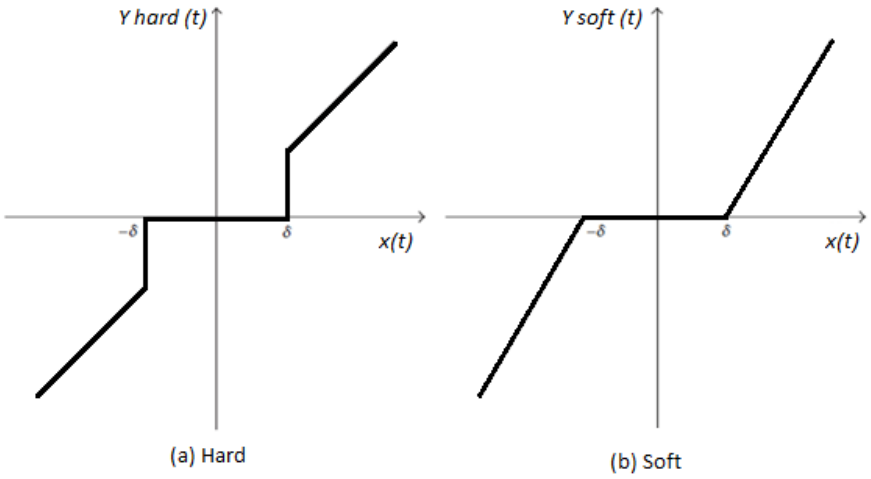

Fig. 4.8. The shapes of hard (a) and soft (b) thresholding operators.

Instead, the universal threshold estimation method proposed by Donoho and Johnstone [13] uses a fixed value, expressed as (Eq. 18):

$$THR_{uni} = \sigma\sqrt{2\log(N)} \tag{18}$$

where N is the length of the samples of the time-domain signal and σ is estimated as the median of the absolute value of the detailed coefficients at the decomposition level *j*, divided by a normalization factor used to rescale the numerator to make the estimate unbiased for the normal distribution [11].

3. Reconstruction.

   After the choice of thresholding rule, the denoised signal is reconstructed by applying the Inverse Wavelet Transform (ISWT) to the approximation coefficient at level *j* and modified detail coefficients from level 1 to *j*. Thus, the denoising algorithm uses statistical regression of noisy coefficients over time to obtain a non-parametric estimation of the reconstructed signal without noise.

Based on the selected mother Wavelet, level of decomposition and the selected thresholding technique, WT denoising is able to discard the out of band noise, providing a great time-frequency resolution for signal analysis. Thus, WT is a well-known denoising technique in the biomedical signal processing [14] [15], [16].

To remove noise from sEMG signal, the Daubechies (db) mother wavelet of 4^{th} order and six decomposition level, has been chosen in this work, in order to have the lowest mean square error [17], [18]. Instead the Coiflets (coif) mother wavelet of 4^{th} order and seven decomposition level has been chosen, in order to remove noise from fPCG signal.

4.5 Scalogram and coscalogram function

A local time-frequency energy density, which measures the energy of *x(t)* in the Heisenberg box of each wavelet $\psi_{a,b}$ is known as wavelet scalogram. The scalogram function is defined as the square of the absolute value of the CWT coefficients, as shown in Eq. 19 [19][1].

$$P_W x(a,b) = |W_x(a,b)|^2 \tag{19}$$

where $W_x(a,b)$ is the matrix of CWT coefficients at time b and scale a for the *x(t)* signal.

Scalogram function can be "translated" to the time–frequency plane (Eq. 20):

$$P_W x(a,b) = |W_x(a,b)|^2 == \sqrt{\frac{2f\sqrt{\pi}}{k}} \left| \int_{-\infty}^{+\infty} s(t) e^{-\left(\frac{1}{2}\right)((2\pi f/k)(t-u))^2} \times \left(e^{i2\pi f(t-u)}\, dt\right| \right|^2 \tag{20}$$

The scalogram highlights the signal's increasing frequency content by the presence of energy in increasingly smaller scales. The scalogram is a time-varying spectral representation, which describes the energy distribution of the signal captured in the details coefficient.

This energy is defined as the sum of the squares of the detail coefficient for each scale. The scalogram is often used to give an estimate of the wavelet spectrum. The wavelet spectrum gives a time–frequency representation, and it measures the contribution to the total energy coming from the vicinity of a point at a specific time and frequency for a given mother wavelet.

In some recent studies, the concept of the scalogram has been used to identify correlation between signals in which the squared coefficients are replaced with the product of the wavelet coefficients of two different processes [20]. This produces a view of the coincident events between the processes, revealing time-varying pockets of correlation with frequency and it is used to depict the covariance between two series, defining a cross wavelet power. Given a pair of time series a cross wavelet power may be defined to identify correlation between the two-time series using the product of their wavelet coefficients; the product is defined as follows (Eq. 21):

$$P_W\, xy(a,b) = W_x(a,b) W_y^*(a,b) \tag{21}$$

where $W_x(a,b)$ and $W_y(a,b)$ represents the CWT coefficients of the two-time series, at scale a and time b; the operator * represents the conjugate complex. The plot of $|P_W\, xy(a,b)|^2$ is called a coscalogram, which displays the coincident events of two series at the time scale plane.

For two biomedical signals, a local cross-correlation between two signals could be identified by computing WT cross-energy density [20]. Thus, WT coscalogram function $P_W\, xy(a,b)$ provides a localized statistical assessment of cross-energy density between signals, that identifies their local correlation.

Chapter references

[1] O. Rioul and M. Vetterli, "Wavelets and Signal Processing," *IEEE Signal Process. Mag.*, vol. 8, no. 4, pp. 14–38, 1991.

[2] J. R. Williams and K. Amaratunga, "Introduction to wavelets in engineering," *Int. J. Numer. Methods Eng.*, 1994.

[3] O. Christensen, "An introduction to wavelet analysis," in *Applied and Numerical Harmonic Analysis*, 2010.

[4] C. Heil, "Ten Lectures on Wavelets (Ingrid Daubechies)," *SIAM Rev.*, 1993.

[5] A. Strazza, F. Verdini, L. Burattini, S. Fioretti, and F. Di Nardo, "Time-frequency analysis of surface EMG signals for maximum energy localization during gait," *Gait Posture*, vol. 57, pp. 9–10, 2017.

[6] A. Sbrollini, A., Strazza, A., Caragiuli, M., Mozzoni, C., Tomassini, S., Agostinelli, A., Morettini, M., Fioretti, S., Di Nardo, F., "Fetal Phonocardiogram Denoising by Wavelet Transformation: Robustness to Noise," *Comput. Cardiol. (2010).*, vol. 44, pp. 1–4, 2017.

[7] M. j. Shensa, "The Discrete Wavelet Transform," *Director*, 1991.

[8] M. Vetterli and C. Herley, "Wavelets and Filter Banks: Theory and Design," *IEEE Trans. Signal Process.*, 1992.

[9] M. Vetterli and J. Kovačević, *Wavelets and subband coding*. 2007.

[10] I. Daubechies, "The Wavelet Transform, Time-Frequency Localization and Signal Analysis," *IEEE Trans. Inf. Theory*, 1990.

[11] D. L. Donoho and J. M. Johnstone, "Ideal spatial adaptation by wavelet shrinkage," *Biometrika*, 1994.

[12] D. L. Donoho, "De-Noising by Soft-Thresholding," *IEEE Trans. Inf. Theory*, 1995.

[13] D. L. Donoho and I. M. Johnstone, "Threshold selection for wavelet shrinkage of noisy data," in *Engineering in Medicine and Biology Society, 1994. Engineering Advances: New Opportunities for Biomedical Engineers. Proceedings of the 16th Annual International Conference of the IEEE*, 1994.

[14] P. B. Patil and M. S. Chavan, "A wavelet based method for denoising of biomedical signal," in *International Conference on Pattern Recognition, Informatics and Medical Engineering, PRIME 2012*, 2012.

[15] M. Aqil, A. Jbari, and A. Bourouhou, "ECG signal denoising by discrete wavelet transform," *Int. J. Online Eng.*, 2017.

[16] P. Mithun, P. C. Pandey, T. Sebastian, P. Mishra, and V. K. Pandey, "A wavelet based technique for suppression of EMG noise and motion artifact in ambulatory ECG," in *Proceedings of the Annual International Conference of the IEEE Engineering in Medicine and Biology Society, EMBS*, 2011.

[17] A. Phinyomark, C. Limsakul, and P. Phukpattaranont, "Application of wavelet analysis in EMG feature extraction for pattern classification," *Meas. Sci. Rev.*, 2011.

[18] A. Phinyomark, C. Limsakul, and P. Phukpattaranont, "EMG denoising estimation based on adaptive wavelet thresholding for multifunction myoelectric control," in *2009 Innovative Technologies in Intelligent Systems and Industrial Applications, CITISIA 2009*, 2009.

[19] O. Rioul and P. Flandrin, "Time-Scale Energy Distributions: A General Class Extending Wavelet Transforms," *IEEE Trans. Signal Process.*, vol. 40, no. 7, pp. 1746–1757, 1992.

[20] P. Sukiennik and J. T. Białasiewicz, "Cross-correlation of bio-signals using continuous wavelet transform and genetic algorithm," *J. Neurosci. Methods*, 2015.

Chapter 5

TIME-FREQUENCY ANALYSIS OF SURFACE EMG SIGNALS FOR MAXIMUM ENERGY LOCALIZATION

The processing of sEMG signals arising from muscle activities is considered as a useful tool for clinical diagnosis, rehabilitation and sport medicine [1]. Many different methods are reported to determine the amplitude of sEMG muscle activation in time domain during walking [2]. The differences among the considered methods and the consequent lack of consistency have been acknowledged as a limitation in the correct identification of the amplitude of sEMG, and in the assessment of sEMG peak value and position [2]. The peak root mean square (pRMS) uses a single value, the maximum of the RMS smoothed signal, to represent muscle activation. Its use was questioned because it is affected by inaccuracy due to motion artifacts [2]. The mean root mean square (mRMS) is a technique that limits the effects of movement artifact. On the other hand, it is less sensitive to changes in the EMG signal and may mask differences in muscle activation intensity between experimental conditions [2]. The integrated EMG or envelope (iEMG) is more robust than pRMS to movement artifact, but is sensitive to temporal changes in onset and offset of muscle activation [2]. Besides those limitations, some authors disapprove the use of amplitude parameters for inter-subject comparison, given that the effect of electrode could affect their assessment location and volume conductor inhomogeneities [3]. From this point of view, it could be more suitable identifying the time-interval where the EMG signal reached its peak value in gait cycle rather than its absolute value. In the same way, a quantification of the frequency band where the information content of the sEMG signal is contained could be meaningful. To pursue these goals, a time-

frequency approach is needed, able to represent the time behavior of the frequency spectrum. In time-frequency domain, sEMG signals can be analyzed using WT analysis. Different studies reported the suitability of WT for this task [4][5]. WT methodology is able to provide the scalogram function, a localized statistical assessment of the time-frequency energy density, that represents the information content of the sEMG signal in both time and frequency domain [6]. Thus, this work [7] was designed to assess the maximum energy localization in time-frequency domain of the sEMG signal of the main lower-limb muscles involved in able-bodied walking.

5.1 Method

5.1.1 Signal acquisition

Ten healthy young adults were recruited for the study. Mean (±SD) characteristics are: age 22.7±0.5 years; height 166±8 cm; weight 53.6±8.1 kg; body mass index (BMI) 18.9±1.5 $kg \cdot m^{-2}$. Exclusion criteria included pathological or chronic joints pain, neurological pathology, orthopedic surgery within previous year, abnormal gait or BMI ≥ 25. Participants signed informed consent. The present research was undertaken in compliance with the ethical principles of Helsinki Declaration and approved by the local expert committee.

Electromyographic signals were acquired (sampling rate: 2 kHz; resolution: 12 bit) and processed by the multichannel recording system, Step32 (Version PCI-32 ch2.0.1. DV) MedicalTechnology, Italy. Each subject was instrumented with foot-switches and sEMG probes on both lower limbs. Three foot-switches (size:11×11×0.5 mm; activation force: 3 N) were attached beneath heel, first and fifth metatarsal heads of each foot. sEMG signals were detected with single differential probes with fixed geometry constituted by Ag/Ag-Cl disks (size: 7 mm × 27 mm × 19 mm; electrode diameter:4 mm; interelectrode distance: 8 mm, gain:1000, high pass filter:10 Hz, input impedance >1.5 GΩ, CMRR > 126 dB, input referred noise ≤ 1 Vrms), and with variable geometry constituted by Ag/Ag-Cl disks (minimum interelectrode distance: 12 mm, gain:1000, high-pass filter:10 Hz, input impedance>1.5 GΩ, CMRR > 126 dB, input referred noise ≤ 200 nVrms). sEMG signals were

further amplified and low-pass filtered (450 Hz) by the recording system. Before positioning the probes, skin was shaved, cleansed with abrasive paste and wet with a soaked cloth. To assure proper electrode-skin contact, electrodes were dressed with highly-conductive gel. Probes were applied over Tibialis anterior, Gastrocnemius lateralis, Rectus femoris, and Biceps femoris (TA, GL, RF, BF), following the SENIAM recommendations for electrode location-orientation over muscles with respect to tendons, motor points and fiber direction [8]. After positioning the sensors, subjects were asked to walk barefoot over the floor for 5 min at their natural pace, back and forth over a 12-m long straight track.

5.1.2 Signal processing

Footswitch signals were debounced, converted to four levels, Heel contact (H), Flat foot contact (F), Push-off (P), Swing (S), and processed to segment and classify the different gait cycle (GC) [9]. sEMG signals were processed by means of Wavelet Transform, a time-frequency analysis method that quantifies temporal changes of the frequency content of non-stationary signals without losing resolution in time or frequency (Chapter 4). To implement WT, mother wavelet Daubechies of order 4 with 6 levels of decomposition (db4) has been chosen, because of its suitability for detecting signal changes and because of its shape is similar to the shape of motor unit action potentials [10]. WT has been applied for removing noise from sEMG, using the denoising algorithm showed in Chapter 4.

The maximum energy localization in time-frequency domain has been identified starting from CWT scalogram function. Scalogram of denoised SEMG signal was computed for each single stride and for every muscle during walking. The localization of the regions with maximum energy density has been identified as the interval in time-frequency where the scalogram is exceeding the 72% of the peak value of energy density in both time and frequency domain.

5.2 Results and discussion

The 3D color representation of the scalogram for sEMG signals from TA, GL, RF, and BF is reported in Fig. 5.1, panel A, B, C, and D, respectively. In the horizontal plane time (% of GC) and frequency (Hz) were represented, for a representative subject.

For TA, the maximum of energy density in time occurred in H-phase, from the beginning to 6 % of GC and in swing phase from 92 to 98% of GC (Fig. 5.1, A); the maximum of energy density in frequency was detected in frequency band between 60-220 Hz (Fig. 5.1, A).

For GL, the maximum of energy density in time occurred in the transition between F and P phases, from 29 to 50 % of GC. The maximum of energy density in frequency was detected in frequency band between 65 and 160 Hz (Fig. 5.1, B).

For RF, maximum energy density is localized in time during H-phase from the beginning to 5% of GC and at the end of GC, during swing phase, from 86 to 95% of GC; the maximum of energy density in frequency was detected in frequency band between 70 and 220 Hz (Fig. 5.1, C).

For BF, the maximum of energy density in time occurred during swing phase, from 80 to 93% of GC and the maximum of energy density in frequency was detected in frequency band between 70 and 180 Hz (Fig. 5.1, D).

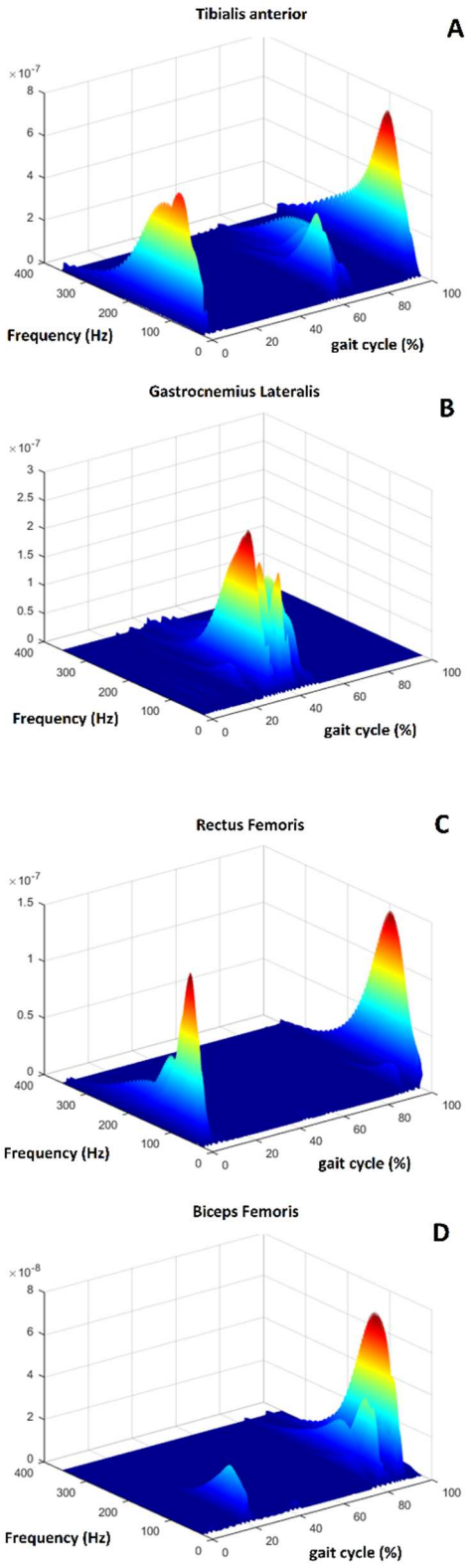

Fig. 5.1. Scalogram: 3D color representation of the wavelet coefficients for TA, GL, RF, and BF in time-frequency domain. The color-level coded scale represents the logarithm of the squared modulus of the wavelet coefficients; red: condition observed when the percentage of energy is max, dark blue: condition when the percentage of energy is minimum.

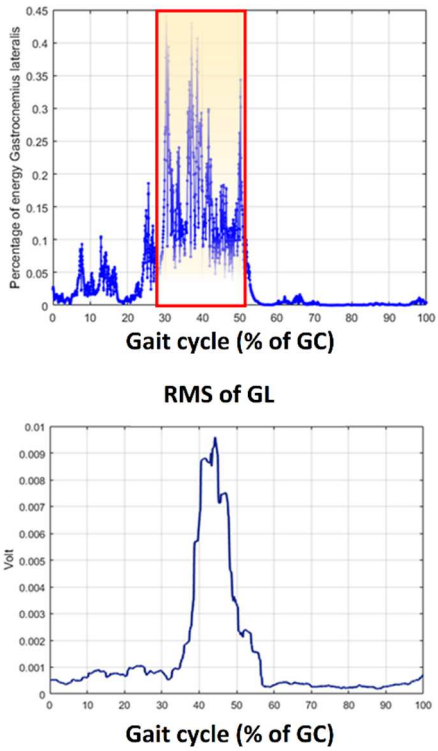

Fig. 5.2. Energy distribution for GL vs. RMS of GL during gait cycle.

Thus, the localization in time of maximum energy density could be interpreted as the time-interval where the sEMG signal reached its peak value of energy, i.e. the region of GC where the muscle is mainly recruited. For the considered muscles, the present localization of maximum muscle activity (example in Fig. 5.2) matched with the region of maximum muscle recruitment reported during walking in able-bodied adults [11][12][13].

Instead, the localization in frequency of maximum energy density, was interpreted as the frequency-band where the EMG signal showed the maximum frequency content. This region of frequency varied from muscle to muscle, but a common frequency band for all muscles could be found between 70 and 160 Hz, matching with [14].

Chapter references

[1] S. L. Pullman, "Clinical utility of surface EMG," *Neurology*, 2000.

[2] D. Renshaw, M. R. Bice, C. Cassidy, a James, and D. W. Powell, "A Comparison of Three Computer-based Methods Used to Determine EMG Signal Amplitude," *Int. J. Exerc. Sci.*, 2010.

[3] M. B. I. Reaz, M. S. Hussain, and F. Mohd-Yasin, "Techniques of EMG signal analysis: detection, processing, classification and applications (Correction)," *Biol. Proced. Online*, vol. 8, no. 1, pp. 163–163, 2006.

[4] F. Verdini, M. Marcucci, M. G. Benedetti, and T. Leo, "Identification and characterisation of heel strike transient," *Gait Posture*, vol. 24, no. 1, pp. 77–84, 2006.

[5] A. Merlo, D. Farina, and R. Merletti, "A fast and reliable technique for muscle activity detection from surface EMG signals," *Biomed. Eng. IEEE …*, vol. 50, no. 3, pp. 316–323, 2003.

[6] O. Rioul and M. Vetterli, "Wavelets and Signal Processing," *IEEE Signal Process. Mag.*, vol. 8, no. 4, pp. 14–38, 1991.

[7] A. Strazza, F. Verdini, L. Burattini, S. Fioretti, and F. Di Nardo, "Time-frequency analysis of surface EMG signals for maximum energy localization during walking," in *IFMBE Proceedings*, 2017.

[8] H. J. Hermens, B. Freriks, C. Disselhorst-Klug, and G. Rau, "Development of recommendations for SEMG sensors and sensor placement procedures," *J. Electromyogr. Kinesiol.*, vol. 10, no. 5, pp. 361–374, 2000.

[9] V. Agostini, A. Nascimbeni, A. Gaffuri, P. Imazio, M. G. Benedetti, and M. Knaflitz, "Normative EMG activation patterns of school-age children during gait," *Gait Posture*, vol. 32, no. 3, pp. 285–289, 2010.

[10] D. Lee and A. Yamamoto, "Wavelet Analysis : Theory and Applications," *Hewlett-Packard J.*, 1994.

[11] J. Perry, *Gait Analysis: Normal and Pathological Function*, vol. 12. 1992.

[12] F. Di Nardo, G. Ghetti, and S. Fioretti, "Assessment of the activation modalities of gastrocnemius lateralis and tibialis anterior during gait: A statistical analysis," *J. Electromyogr. Kinesiol.*, vol. 23, no. 6, pp. 1428–1433, 2013.

[13] F. Di Nardo and S. Fioretti, "Statistical analysis of surface electromyographic signal for the assessment of rectus femoris modalities of activation during gait," *J. Electromyogr. Kinesiol.*, vol. 23, no. 1, pp. 56–61, 2013.

[14] C. J. De Luca, "The use of surface electromyography in biomechanics," in *Journal of Applied Biomechanics*, 1997.

Chapter 6

CODE: CO-CONTRACTION DETECTION ALGORITHM

The quantitative assessment of muscle co-contractions is meaningful for deepening the comprehension of this neurophysiological mechanism and for discriminating conditions of dysfunction of the central nervous system, such as traumatic brain injury, stroke, cerebral palsy, or Parkinson's disease [1]. Despite the great importance of this physiological phenomenon, a gold standard for identifying muscle co-contraction is not available yet. Moreover, poor information is available in literature to assess the frequency band where the muscles showed the reported co-contractions. Thus, a reliable approach able to quantify the information included in the concomitant evaluation of time interval, magnitude, and frequency band of the co-contraction could be valuable. To pursue these aims, wavelet transform (WT) analysis of sEMG signals appears to be an appropriate approach. WT is an advanced signal processing technique that maps a time waveform into time-frequency domain providing a good localization in both time and frequency domains [2]. This multiresolution analysis allows to define time-frequency energy density of a signal and to provide a localized statistical assessment of the time-frequency cross-energy density between two signals [3]. Thus, a novel approach for assessing muscle co-contraction in terms of time interval, magnitude, and frequency band, using the cross-energy localization in time-frequency domain of sEMG signal is developed: CO-contraction DEtection algorithm (CODE). CODE algorithm has been developed in two following steps: Wavelet-Transform-sEMG denoising and Coscalogram-based sEMG detection.

6.1 CODE algorithm: CO-contraction DEtection algorithm

The scheme of the entire experimental processing, from data acquisition to muscle co-contraction detection is reported in Fig. 6.1.

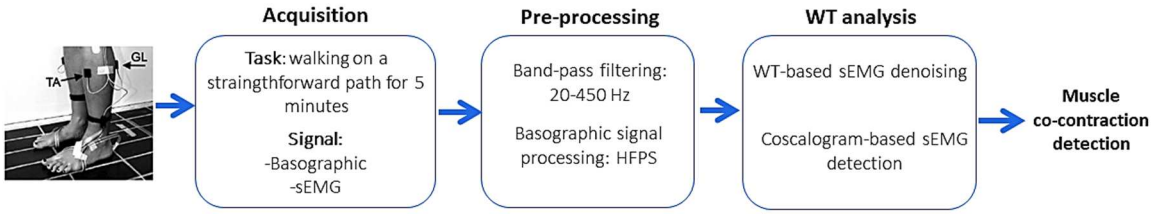

Fig. 6.1. Scheme of the entire experimental processing, from data acquisition to muscle co-contraction detection.

6.1.1 Wavelet-Transform-based sEMG denoising

WT denoising is based on decomposition of the signal, modification of detail coefficients with respect to a defined soft threshold and then signal reconstruction with respect to the new coefficients [4]. Noise coefficients are concentrated in low values of scale parameter, corresponding to high frequency ranges while the sEMG signal is distributed in high and low frequency ranges (large and low values of scale parameter). Thus, WT denoising involves adopting a statistical regression of noisy coefficients over time to obtain a nonparametric estimation of the reconstructed signal without noise. The decomposition processing allows to remove the level which seriously corrupted by noise. In level decomposition, wavelet coefficients tend to be much larger than those due to noise. Thus, coefficients below a certain level are regarded as noise and are thresholded out. The signal can then be reconstructed without significant loss of information in the signal content. In the present study, a soft threshold (Donoho threshold) was adopted for denoising procedure [5][6][7]. sEMG signal was reconstructed by revised WT coefficients. A block diagram for describing WT denoising procedure is presented in Fig. 6.2.

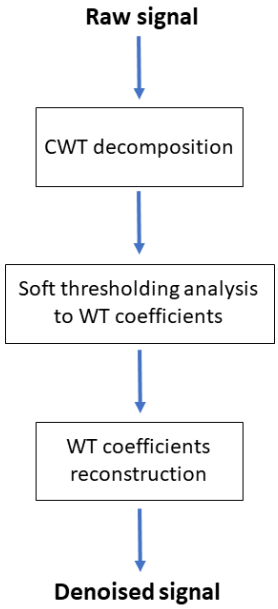

Fig. 6.2. Block diagram representing WT denoising procedure.

To evaluate the goodness of WT denoising procedure, the SNR values were computed according to the following definition (Eq. 1):

$$SNR = 10 * \log \frac{(\sigma_s^2)}{(\sigma_n^2)} \quad (1)$$

where σ_s and σ_n are the standard deviation of signal and noise, respectively. Thus, SNRraw represents the SNR values of sEMG signals before the WT denoising, while SNRclean represents the SNR values of denoised signals after the WT denoising.

6.1.2 Coscalogram-based sEMG detection

In WT analysis, the energy localization in time-frequency domain is identified by scalogram function $P_W\, x(a,b)$ [2] that is defined as the square of the absolute value of WT coefficients (Eq. 2):

$$P_W\, x(a,b) = |W_x\ (a,b)|^2 \quad (2)$$

where $W_x(a,b)$ is the matrix of WT coefficients at time b and scale a for the *x(t)* signal. Starting from the WT denoised signal, WT scalogram function in time-frequency domain of denoised sEMG signal was adopted for assessing muscular activation.

Local cross-correlation between two signals could be identified by computing CWT cross-energy density between signals [3]. WT coscalogram function $P_W\,xy(a,b)$ provides a localized statistical assessment of cross-energy density between signals, following Eq. 3:

$$P_W\,xy(a,b) = W_x(a,b)W_y^*(a,b) \tag{3}$$

where $W_x(a,b)$ and $W_y(a,b)$ represents the WT coefficients of the two denoised signals, at scale a and time b; the operator (*) represents the conjugate complex. Starting from the WT denoised signal, WT coscalogram function in time-frequency domain of denoised sEMG signals was adopted for assessing the co-contraction signal between the selected muscles. A block diagram for describing WT procedure for the assessment of muscle-co-contraction signal is presented in Fig. 6.3.

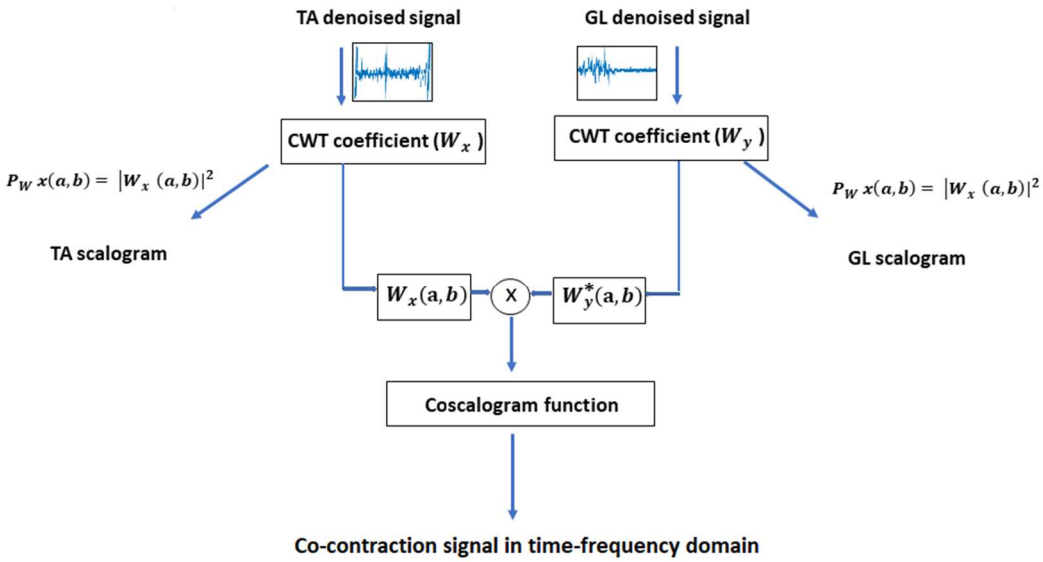

Fig. 6.3. Block diagram of CODE alghoritm.

CODE algorithm is tested on simulated and real data. Simulated sEMG signals were denoised and then processed with CODE algorithm for the assessment of co-contraction signal. Performance of CODE algorithm, for simulated sEMG signal, was evaluated in time domain. In literature, a gold standard method for the identification of muscle co-contraction is not available. Thus, to this aim, the "reference" co-contraction interval was computed as the time interval where the concomitant presence of the two-clean simulated sEMG signals (i.e. before the addition of Gaussian noise n(t))

was acknowledged [8][9]. Co-contraction interval assessed by CODE algorithm was directly compared with the "reference" co-contraction interval for evaluating the performance of the algorithm.

Experimental sEMG signals, acquired in the 'Analisi del Movimento' laboratory, were denoised and then processed with CODE algorithm for the assessment of co-contraction signal. Performance of CODE algorithm, also for experimental sEMG signal, was evaluated in time domain. The "reference" co-contraction interval was computed considering the superimposition between the activation intervals of the two sEMG signals analyzed. The activation intervals were assessed applying to each signal a double-threshold statistical detector [10]. Results were reported in terms of accuracy (bias) and precision (standard deviation, SD)[11][12].

6.2 Materials

6.2.1 Simulation study

Several studies asserted that sEMG signal is well described by a Gaussian distribution and could be assumed as a Gaussian random process [13]. It has been reported that sEMG signal could be considered also an ergodic process [14]. Thus, during muscle activity, sEMG trace was simulated by adding two uncorrelated realizations of Gaussian white noise playing, respectively, as myoelectric signal and additive noise. The first one was obtained by using a rectangular amplitude modulation and by band-pass filtering the first Gaussian series of white noise. The band-pass filter cut-off frequencies F_l and F_h were set to 80 and 120 Hz, respectively. The filter characteristics were chosen according to the model proposed by Stulen and De Luca (1981) [15], that was conceived to represent a sEMG burst by artificially generating its power spectrum (Eq. 4):

$$P(f) = \frac{F_h^4 * f^2}{(f+F_l^2)(f+F_h^2)^2} \tag{4}$$

Background uncorrelated noise was achieved by a further independent zero-mean Gaussian distribution. The power of the second noise realization, simulating the additive noise, was set to

generate sEMG signals with the following SNR values: 5,10,15,20 dB. One hundred couples of simulated signals (a total of 200 signals) were generated, varying temporal shifting and span of Gaussian distribution. Thirty epochs, 1 s long, were synthesized, and each of them passed the Anderson's whiteness test with a 95% confidence level. The sampling rate was equal to 1000 samples/s. Simulated sEMG signals representing the activity of two muscles were reported in Fig. 6.4.

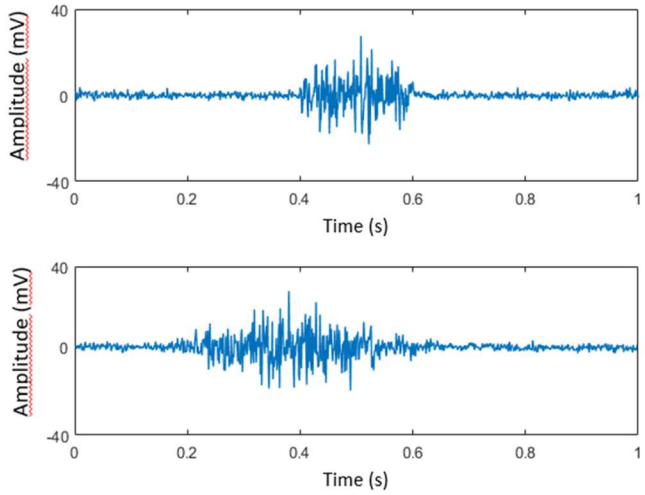

Fig. 6.4. Example of a couple of simulated EMG signals.

6.2.2 Experimental study

Validation of the presented technique was performed also on a set of experimental sEMG signals from an antagonist muscle couple during walking. Gastrocnemius lateralis (GL) and tibialis anterior (TA), antagonist muscles at ankle joint during walking [16], were considered to this aim. Thirty able-bodied young adults were recruited for the study. Mean (±SD) anthropometric characteristics of the sample population are: age 23.8 ± 1.9 years; height 173 ± 10 cm; weight 63.3 ± 12.4 kg; body mass index (BMI) 20.8 ± 2.1 $kg \cdot m^{-2}$. Participants signed informed consent. The present research was undertaken in compliance with the ethical principles of Helsinki Declaration of 2008 and approved by institutional expert committee. Subjects were asked to walk barefoot over the floor for around 5 minutes at their natural speed and cadence, such as reported in Fig. 6.5. Step32 software automatically removes outlier cycles relative to direction changes, including deceleration before the

turning and acceleration after it. More specifically, the duration of the gait phases is used by a multivariate statistical filter to discard outlier cycles, i.e. cycles with improper sequences of gait phases and strides with the proper sequence of gait phases (HFPS) but with abnormal timing (such as those relative to deceleration, reversing, and acceleration).

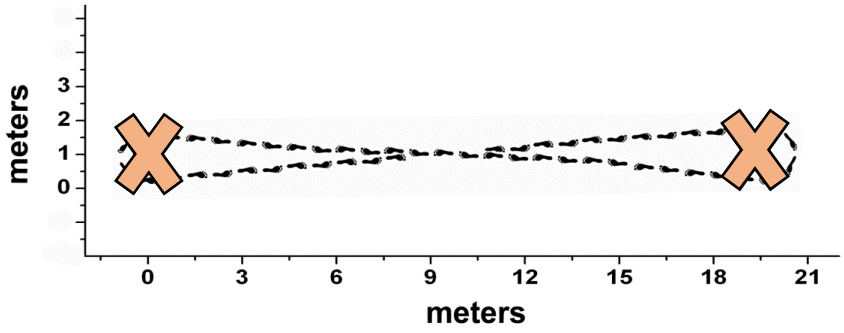

Fig. 6.5. Path of subject movement without outliers (i.e. direction changes).

6.2.3 Experimental data processing

The acquisition of sEMG signals was achieved by means of Step 32 system (Medical Technology, Italy) with a sampling rate of 2 kHz and a resolution of 12 bit. Step 32 is an electro-medical system for the simultaneous acquisition of 32 signals, 16 from sensors positioned on the patient and 16 others coming from different devices, such as force platforms. STEP32 has a complete range of sensors: basographic, accelerometric, goniometric, probes for sEMG signal. The experimental set-up is characterized by basographic sensors and probes for sEMG signal acquisition. Characteristics of the probes are: single differential probes with fixed geometry constituted by Ag/Ag-Cl disks; size: 7×27×19 mm; electrode diameter: 4 mm; interelectrode distance: 12 mm, gain: 1000, high-pass filter: 10 Hz, input impedance >1,5GΩ, CMRR >126 dB. After acquisition, sEMG signals were further amplified and low-pass filtered (450 Hz) by recording system. For a better sEMG signal acquisition, the skin was shaved, cleansed with abrasive paste and moistened. To assure proper electrode-skin contact, each electrode was dressed with highly-conductive gel. Probes were applied over GL and TA, following SENIAM recommendations for electrode location and orientation over muscle with respect to tendons and fiber direction [17]. Then, subjects walked barefoot over floor at natural pace, over a 10-m straight track. Step32 software automatically removes outlier cycles relative to direction

changes, including deceleration before the turning and acceleration after it. More specifically, the duration of the gait phases is used by a multivariate statistical filter to discard outlier cycles, i.e. cycles with improper sequences of gait phases and strides with the proper sequence of gait phases (HFPS) but with abnormal timing (such as those relative to deceleration, reversing, and acceleration).

Raw sEMG signals from TA and GL in a representative subject acquired in a selected stride during walking task were reported in Fig. 6.6.

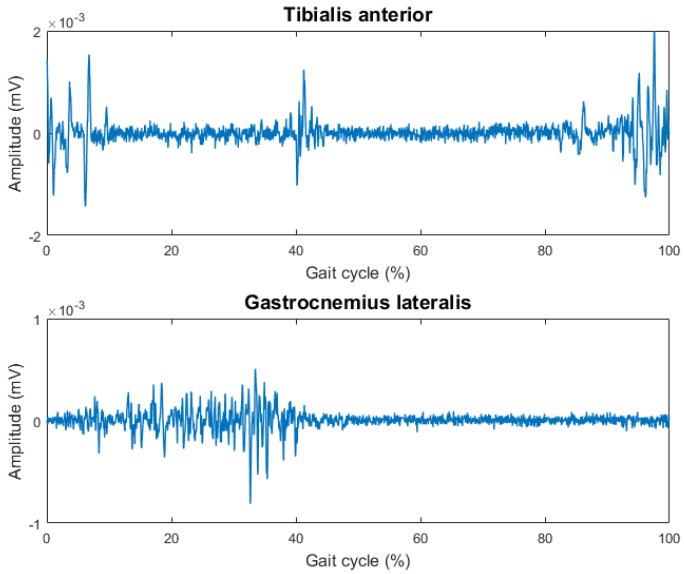

Fig. 6.6. Raw signal of TA (upper panel) and GL (lower panel).

sEMG signals from TA and GL muscles were processed with CODE algorithm for the assessment of co-contraction signal.

6.3 Results

6.3.1 Simulation Study

The two-dimensional color representation of WT scalogram function for the two simulated sEMG signals is reported in Fig. 6.7 (panel A and B, respectively). Panel C of the same figure showed the cross-energy density in time-frequency domain between denoised simulated sEMG signals, represented by WT coscalogram function, i.e. the estimated co-contraction signal.

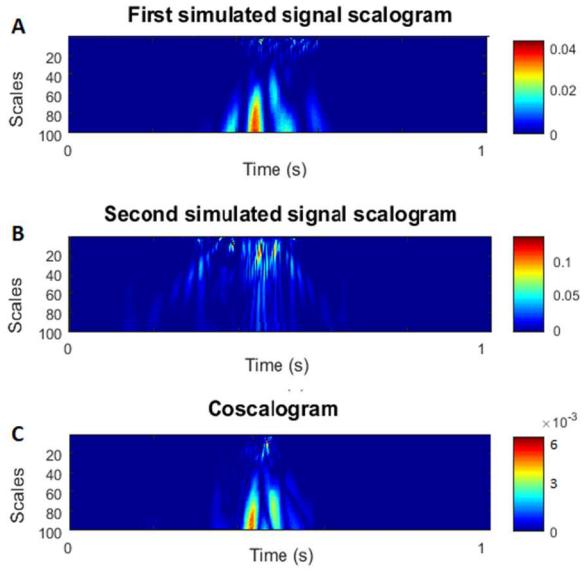

Fig. 6.7. Two-dimensional color representation of WT scalogram function for two simulated signals (panel A-B) and WT coscalogram between simulated signals (panel C).

The accuracy of CODE algorithm in providing the co-contraction time-interval was assessed considering the 100 couples of simulated signal (25 couples for each SNR value). Results were reported in Table 1 in terms of accuracy (bias) and precision (standard deviation, SD). Average bias values computed for SNR = 5 dB were significantly higher ($p < 0.05$) than all the average values computed in the other three SNR conditions, for the detection of both ON and OFF instant of the co-contraction.

Table 1 – Accuracy (bias) and precision (SD) of CODE algorithm assessed in 100 couples of simulated signals.

	5 dB		10 dB		15 dB		20 dB	
	ON	**OFF**	**ON**	**OFF**	**ON**	**OFF**	**ON**	**OFF**
Bias	11.3*	6.8+	5.4	3.9	5.2	3.6	3.5	2.6
SD	8.9	4.3	4.2	1.6	3.6	1.7	2.0	1.3

* significantly different ($p < 0.05$) from all other ON-bias.
+ significantly different ($p < 0.05$) from all other OFF-bias.

6.3.2 Experimental study

SNR values of raw sEMG signals (SNRraw) and after the WT denoising (SNRdenoised) were reported in Table 1, for the thirty subjects analyzed.

Table 2 – SNR values of raw sEMG signals (SNRraw) and after the WT denoising (SNRdenoised) for tibialis anterior and gastrocnemius lateralis.

	Tibialis anterior		Gastrocnemius lateralis	
Subjects	**SNRraw (dB)**	**SNRdenoised (dB)**	**SNRraw (dB)**	**SNRdenoised (dB)**
#1	8.9	17.7	13.1	39.1
#2	4.7	8.5	5.8	17.6
#3	13.3	17.5	16.4	17.5
#4	9.8	12.7	5.0	7.7
#5	7.3	9.1	8.7	10.5
#6	12.6	19.2	16.1	18.5
#7	24.7	30.8	10.7	15.4
#8	23.5	32.3	20.5	33.0
#9	4.5	9.3	3.3	7.3
#10	2.4	4.3	6.0	8.2
#11	27.3	35.4	16.3	21.7
#12	22.1	29.7	11.3	16.8
#13	17.2	21.7	13.1	19.4
#14	16.4	19.3	18.5	20.7
#15	5.5	9.8	13.9	18.5
#16	18.1	24.3	14.9	15.4
#17	25.3	32.9	17.4	20.5
#18	27.1	31.2	25.8	30.7
#19	11.5	18.1	12.7	15.1
#20	16.2	18.9	17.0	20.1
#21	14.2	16.7	18.1	19.4
#22	12.2	16.4	13.9	15.8
#23	20.2	25.6	12.9	17.4
#24	11.8	20.9	18.9	21.7
#25	13.1	18.8	21.0	24.4
#26	17.8	19.9	20.5	23.7
#27	14.6	17.6	15.6	18.3
#28	5.4	9.8	3.9	8.5
#29	17.3	20.5	12.5	15.1
#30	10.6	15.7	16.8	23.1
Mean±SD	14.5±6.9	19.5±8.0	14.0±5.4	18.7±7.1

Two-dimensional color representation of WT scalogram function for TA (panel A) and GL (panel B) denoised sEMG signals was reported in Fig. 6.8 for a representative stride from subject 5 (low SNR) and in Fig. 6.9 for a representative stride from subject 26 (high SNR) (Table 2). Panel C of the same figures showed the cross-energy density in time-frequency domain between denoised TA and GL sEMG signals, represented by WT coscalogram function, i.e. the estimated co-contraction signal in a representative stride of the walking task of a single subject.

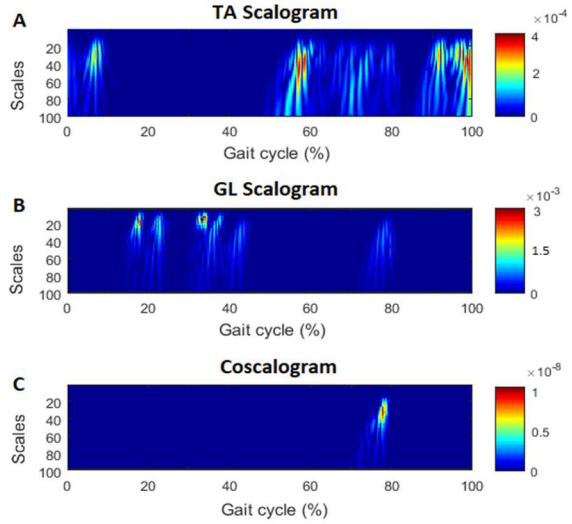

Fig. 6.8. Two-dimensional color representation of WT scalogram function for TA (panel A) and GL (panel B) denoised sEMG signals and WT coscalogram between TA and GL (panel C) for a representative stride from subject 5.

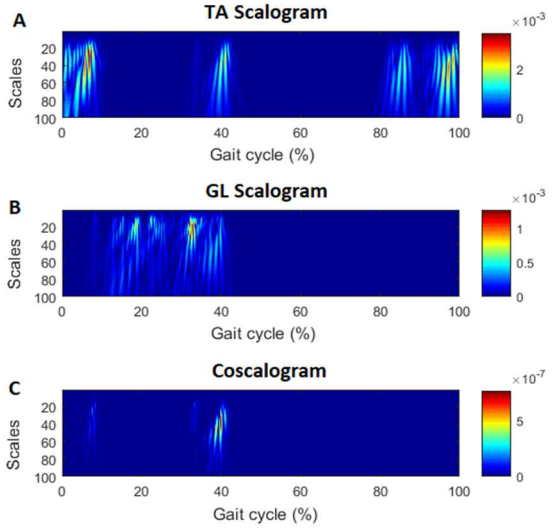

Fig. 6.9. Two-dimensional color representation of WT scalogram function for TA (panel A) and GL (panel B) denoised sEMG signals and WT coscalogram between TA and GL (panel C) for a representative stride from subject 26.

A 3D color representation of WT coscalogram was reported in Fig. 6.10, for each representative subject (panel A-B).

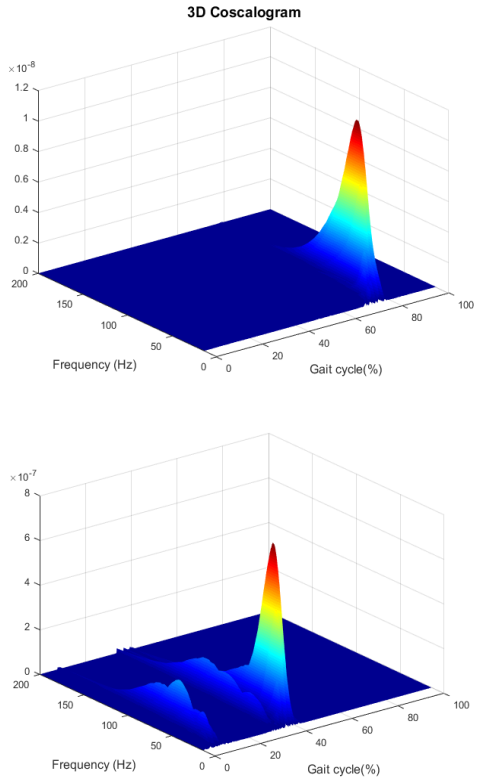

Fig. 6.10. Three-dimensional color representation of WT coscalogram function for subject 5 (panel A) and subject 26 (panel B). Frequency range of 0-200 Hz has been reported to graphically highlight the co-contraction.

The accuracy of CODE algorithm was evaluated in time domain. The "reference" co-contraction interval was assessed considering the superimposition between the activation intervals of the two sEMG signals analyzed. The activation intervals were assessed applying to each signal a double-threshold statistical detector [10]. Results of CODE algorithm accuracy for experimental study was reported in Table 3 in terms of accuracy (bias) and precision (standard deviation, SD).

Table 3 – Accuracy (bias) and precision (SD) of CODE algorithm assessed in experimental data.

	ON	**OFF**
Bias	6.9	9.6
SD	2.9	2.4

6.4 Discussion

CODE algorithm is a novel approach for assessing muscle co-contraction in terms of time interval, magnitude, and frequency band, based on WT cross-energy localization in time-frequency domain of two sEMG signals. WT coscalogram function, a localized statistical assessment of the time-frequency cross-energy density between two sEMG signals, was proposed as representative of the muscular co-contraction signal in time-frequency domain. WT coscalogram function has been successfully used for testing cross-correlation between two different bio-signals [3]. This is the first attempt to interpret WT coscalogram function between sEMG signals from two antagonist muscles as the muscular co-contraction activity in time-frequency domain. Accuracy of CODE algorithm in the detection of muscular co-contraction was estimated for both simulated and real data. Since no reference data or technique were available in time-frequency domain, validation was performed in time domain, where co-contraction is typically quantified as the temporal interval where sEMG activity of the two muscles superimposed [8][9]. Practically, for simulated sEMG bursts, a direct comparison of the co-contraction interval provided by CODE algorithm was performed with the time interval where the two clean simulated sEMG signals superimposed. Then, bias and SD were computed (Table 1). Vannozzi et al. reported a performance ranging from 6.5 to 7.1 ms (onset) and from 4.1 to 11.0 ms (offset) for bias for their wavelet-based algorithm for sEMG onset/offset detection [11]. Associated SD ranged from 5.3 to 8.7 ms. Similar values were reported by Staude et al. [18], in their systematic comparison of techniques for sEMG onset detection. Higher values were indicated by Merlo et. al [19], but in different (lower) SNR condition. Considering that CODE algorithm needed to concomitantly process two different sEMG signals (and not only one, as in the reported studies) and the different SNR range of the simulated signals among studies, results on bias and standard deviation are consistent with the aforementioned studies. Thus, the accuracy of CODE algorithm could be considered widely satisfactory within the tested SNR range. Moreover, statistical analysis showed that different SNR values within the range of 10-20 dB did not modify the performance of CODE algorithm in the detection of both onset and offset instants. This result

matched with [11]. The significant increase of the bias detected for SNR values of 5 dB (Table 1) indicated a worsening of the algorithm performance for so low SNR values. This worsening, however, did not affect the reliability of the detection since bias (11.3 for ON, 6.8 for OFF) and SD (8.9 for ON, 4.3 for OFF) are comparable with values reported by others [11][19], for similar or higher SNR. Moreover, CODE algorithm was tested also on a set of experimental sEMG signals (walking data from able-bodied subjects) from ankle-antagonist muscles. As indicated in [20], wavelet approach guaranteed a reliable denoising of sEMG signals (Table 2). Fig. 6.8 and Fig. 6.9 showed as the application of CODE algorithm to real signals is able to represent the co-contraction between TA and GL activity in function of time (x-axis), frequency (y-axis), and magnitude (colored scale at the left of the figure). In particular, this representation allowed a simple and direct identification of co-contraction in time domain (% of gait cycle). 3D graph (Fig. 6.10) appeared to be more suitable for an overall representation of the co-contraction, including the magnitude and the frequency band. For experimental sEMG bursts, a direct comparison of the co-contraction interval provided by CODE algorithm was performed with a "reference" co-contraction interval, assessed considering the superimposition between the activation intervals of the two sEMG signals analyzed. The activation intervals were calculated applying to each signal a double-threshold statistical detector [10]. Then, bias and SD were computed (Table 3). CODE algorithm is able to reveal the timing of muscular co-contraction with performance comparable to the literature [11]. Application of the algorithm to the whole population of 30 subjects provided, also, findings that are totally consistent with what reported by reference studies on ankle-muscle co-contraction detected on a large number of strides (more than ten thousand) [9]. The co-contraction between TA and GL activity identified in Fig. 6.8 (panel C) matched, indeed, with the region of co-contraction detected by the aforementioned reference study in swing phase and centered in the 80% of gait cycle [9]. In the same way, co-contractions estimated by CODE algorithm in Fig. 6.9 (panel C) fell in the region of co-contraction detected during weight acceptance and in the second half of the stance phase between 40% and 60% of gait cycle [9]. Similar consideration could be done for each of the strides analyzed in the present study, suggesting the algorithm being suitable for experimental applications. Thus, the reliability of CODE algorithm could be considered task independent, although it has been experimentally tested only on sEMG signal

acquired during walking. However, studies for a direct validation on different motor task (jump, squat, running) are evoked.

The representation provided by WT coscalogram function is able to quantify muscular co-contraction, in terms of time interval, magnitude, and frequency band. This is a relevant improvement over techniques that provided only a numerical co-contraction index [21][22][23][24] or dynamic information in time domain, at best [8][25][26][9]. CODE algorithm, indeed, is able to characterize each co-contraction with three features (time, magnitude and frequency), monitoring possible changes of this range, and correlating the relative role of each abovementioned feature in the phenomenon. This could be particularly valuable since changing in the co-contraction picture of a subject was acknowledged as a marker of neurological impairment [1]. Moreover, recent rehabilitation techniques aimed to modify co-contraction patterns in order to get to positive long-term clinical outcomes [27]. CODE algorithm could be considered a reliable tool for monitoring possible co-contraction changes during long-term follow-up.

The present study was designed to propose a novel method for assessing co-contraction between two antagonist muscles, based on WT cross-energy localization in time-frequency domain of surface EMG signal. The algorithm is able to provide a quantification of co-contraction in terms of time interval, magnitude, and frequency band. The satisfactory algorithm accuracy and precision in co-contraction detection and physiological reliability of experimental results support the suitability of the present tool for clinical applications.

Chapter references

[1] M. C. N. Rosa, A. Marques, S. Demain, C. D. Metcalf, and J. Rodrigues, "Methodologies to assess muscle co-contraction during gait in people with neurological impairment - A systematic literature review," *Journal of Electromyography and Kinesiology*, vol. 24, no. 2. pp. 179–191, 2014.

[2] O. Rioul and P. Flandrin, "Time-Scale Energy Distributions: A General Class Extending Wavelet Transforms," *IEEE Trans. Signal Process.*, vol. 40, no. 7, pp. 1746–1757, 1992.

[3] P. Sukiennik and J. T. Białasiewicz, "Cross-correlation of bio-signals using continuous wavelet transform and genetic algorithm," *J. Neurosci. Methods*, 2015.

[4] S. G. Mallat, "A Theory for Multiresolution Signal Decomposition: The Wavelet Representation," *IEEE Trans. Pattern Anal. Mach. Intell.*, vol. 11, no. 7, pp. 674–693, 1989.

[5] D. L. Donoho and J. M. Johnstone, "Ideal spatial adaptation by wavelet shrinkage," *Biometrika*, 1994.

[6] D. L. Donoho, "De-Noising by Soft-Thresholding," *IEEE Trans. Inf. Theory*, 1995.

[7] M. Vetterli and J. Kovačević, *Wavelets and subband coding*. 2007.

[8] A. Strazza, A. Mengarelli, S. Fioretti, L. Burattini, V. Agostini, M. Knaflitz, and F. Di Nardo, "Surface-EMG analysis for the quantification of thigh muscle dynamic co-contractions during normal gait," *Gait Posture*, vol. 51, pp. 228–233, 2017.

[9] F. Di Nardo, A. Mengarelli, E. Maranesi, L. Burattini, and S. Fioretti, "Assessment of the ankle muscle co-contraction during normal gait: A surface electromyography study," *J. Electromyogr. Kinesiol.*, vol. 25, no. 2, pp. 347–354, 2015.

[10] P. Bonato, T. D'Alessio, and M. Knaflitz, "A statistical method for the measurement of muscle activation intervals from surface myoelectric signal during gait," *IEEE Trans. Biomed. Eng.*, vol. 45, no. 3, pp. 287–299, 1998.

[11] G. Vannozzi, S. Conforto, and T. D'Alessio, "Automatic detection of surface EMG activation timing using a wavelet transform based method," *J. Electromyogr. Kinesiol.*, 2010.

[12] G. Severini, S. Conforto, M. Schmid, and T. D'Alessio, "Novel formulation of a double threshold algorithm for the estimation of muscle activation intervals designed for variable SNR environments," *J. Electromyogr. Kinesiol.*, 2012.

[13] E. Kwatny, D. H. Thomas, and H. G. Kwatny, "An Application of Signal Processing Techniques to the Study of Myoelectric Signals," *IEEE Trans. Biomed. Eng.*, 1970.

[14] J. G. Proakis and D. G. Manolakis, "Digital Signal Processing Principoles, Algorithms and Applications," *Digital Signal Processing*. 1996.

[15] F. B. Stolen, and C. J. De Luca, "Frequency Parameters of the Myoelectric Signal as a Measure of Muscle Conduction Velocity," *IEEE Trans. Biomed. Eng.*, 1981.

[16] J. Perry, *Gait Analysis: Normal and Pathological Function*, vol. 12. 1992.

[17] H. J. Hermens, B. Freriks, C. Disselhorst-Klug, and G. Rau, "Development of recommendations for SEMG sensors and sensor placement procedures," *J. Electromyogr. Kinesiol.*, vol. 10, no. 5, pp. 361–374, 2000.

[18] G. Staude, C. Flachenecker, M. Daumer, and W. Wolf, "Onset Detection in Surface Electromyographic Signals :," *J. Appl. Signal Process.*, 2001.

[19] A. Merlo, D. Farina, and R. Merletti, "A fast and reliable technique for muscle activity detection from surface EMG signals," *Biomed. Eng. IEEE*, vol. 50, no. 3, pp. 316–323, 2003.

[20] A. Phinyomark, C. Limsakul, and P. Phukpattaranont, "A comparative study of wavelet denoising for multifunction myoelectric control," in *Proceedings - 2009 International Conference on Computer and Automation Engineering, ICCAE 2009*, 2009.

[21] G. Frost, J. Dowling, K. Dyson, and O. Bar-Or, "Cocontraction in three age groups of children during treadmill locomotion," *J. Electromyogr. Kinesiol.*, vol. 7, no. 3, pp. 179–186, 1997.

[22] S. Hesse, B. Brandl-Hesse, U. Seidel, B. Doll, and M. Gregoric, "Lower limb muscle activity in ambulatory children with cerebral palsy before and after the treatment with Botulinum toxin A," *Restor. Neurol. Neurosci.*, 2000.

[23] U. F. Ervilha, T. Graven-Nielsen, and M. Duarte, "A simple test of muscle coactivation estimation using electromyography," *Brazilian J. Med. Biol. Res.*, 2012.

[24] H. Souissi, R. Zory, J. Bredin, and P. Gerus, "Comparison of methodologies to assess muscle co-contraction during gait," *J. Biomech.*, 2017.

[25] K. S. Rudolph, M. J. Axe, and L. Snyder-Mackler, "Dynamic stability after ACL injury: Who can hop?," *Knee Surgery, Sport. Traumatol. Arthrosc.*, 2000.

[26] M. Mohr, K. Lorenzen, L. Palacios-Derflingher, C. Emery, and B. M. Nigg, "Reliability of the knee muscle co-contraction index during gait in young adults with and without knee injury history," *J. Electromyogr. Kinesiol.*, 2018.

[27] S. J. Preece, R. K. Jones, C. A. Brown, T. W. Cacciatore, and A. K. P. Jones, "Reductions in co-contraction following neuromuscular re-education in people with knee osteoarthritis," *BMC Musculoskelet. Disord.*, 2016.

Chapter 7

SIDE STUDY: WAVELET TRANSFORM ANALYSIS OF FETAL PHONOCARDIOGRAPHY SIGNAL

Wavelet analysis is applied not only for the detection of muscular co-contraction during walking, showed in the previous chapter, but also for the extraction of the main features of fetal phonocardiography signal. Thus, in this work, a WT-based side study is developed to propose a novel and efficient algorithm to achieve a clear separation and detection of the fetal heart sound from fetal phonocardiography signals.

Continuous and long-term fetal monitoring has become an essential approach for better accuracy in diagnosis [1][2]. A passive alternative for long-term monitoring of the fetus is the fetal heart auscultation. Auscultation [3] is a non-invasive method that records the vibroacoustic signals from the abdominal surface and it is used by gynecologists and obstetricians to evaluate fetal well-being during pregnancy and to detect the presence of abnormalities. The acoustic signal produced by the fetal heart sound (fHSs) can be visually depicted in the fetal phonocardiograph [4]. Phonocardiogram acquisition, analysis and processing of fHSs from the maternal body is known as fetal phonocardiography (FPCG). FPCG is a low-cost and non-invasive technique for the detection of fHSs, recording the vibroacoustic signals from the maternal abdomen [4]. Under normal condition, fHSs can be characterized by two major audible sounds for each cardiac cycle: the first heart sound (S1) and the second heart sound (S2). The S1 sound, marking ventricular systole onset, is due to the sudden closure of atrioventricular valves. This sound is characterized of two internal components: the mitral component, associated with the closure of the mitral valve, and the tricuspid component,

associated with the closing of the tricuspid valve. The S2 sound, marking diastole onset, is made up of two components: the aortic component, corresponding to the closure of the aortic valve, and the pulmonary component, corresponding of the closure of the pulmonary valve. S1 sound typically contains low frequency with longest duration and highest intensity. Indeed, S2 sound presents smoother morphology with high frequency and shorter duration than the S1, making harder the detection of its location [5]. The intensity of S1 is generally increased by greater pressure within the left ventricle as the resistance within the pulmonary artery increases and as the blood passes from the left atrium. This greater pressure results in the closure of the mitral valve with greater force, thus producing a more intense sound. On the other hand, S2 is considered to be more useful when diagnosing cardiac disease and is produced by the ejection of blood from the ventricles out through the aorta and pulmonary artery. The significant information in the main components of fHSs signal is contained in the frequency spectrum between 0.1 Hz and 70 Hz. Unfortunately, fHSs are very weak acoustic signals. The heart sound S1 belongs to low frequency band (20-40 Hz) and it is usually the longest and loudest heart sound. Similarly, S2 belongs to high frequency band (50-70 Hz) and its duration is shorter than S1 [6]. Moreover, FPCG is a linear summation of fetal heart sounds, internal noise and external noise. The internal noise is a random signal caused by fetal movement, fetal breathing, maternal respiratory sounds, maternal digestive sound, maternal heart sound, placental blood turbulence. These noises are of low amplitude with main frequency components from DC to 25 Hz [7]. Similarly, the external noise is a combination of shear noise from movement of the sensor during recording and environmental noise such as sound produced by fan, hue and cry of the nearby people, additional components result from powerline interference, and background noise [4]. It has high amplitude and the frequency ranges between 100-20000 Hz. Thus, as it is heavily contaminated by noise, determination of fHSs raises serious signal processing issues, due also to non-stationary nature of FPCG signals. In literature, many methods have been developed for FPCG segmentation. Amplitude and time threshold-based methods [8], probabilistic models-based methods [9][10], and energy-based methods [11] are developed to detect fHSs, but not considering the noisy environment of the FPCG signals. Thus, in a noisy environment, fHSs detection remains a challenging task and it is difficult to detect them accurately. Indeed, it is necessary to erase noise from the signals in order

to make FPCG clinically usable. For this purpose, wavelet transformation (WT), a well-known denoising technique, have been proposed to filter FPCG [12][13]. In time-frequency analysis, WT processing is a useful tool for extracting local time-frequency information from a nonstationary signal, such as FPCG. Thus, a novel and efficient algorithm to achieve a clear separation and detection of the fHSs from WT denoised FPCG signal is developed: PCG-Delineator [14].

Another approach, based on the WT scalogram function, is implemented to detect S1 sound, feature useful to extract the fetal heart rate (fHR). fHR represents one of the most important parameters used nowadays in hospitals for clinical assessment of fetal-wellbeing during pregnancy. The WT scalogram function provides the localization of S1 sounds in a time-frequency plane. After the detection of S1 using the two-different approaches and the segmentation of FPCG signal in windows of 10 s, fetal heart rate (fHR) and the meah fHR are extracted, considering the difference between two consecutive S1 peaks of each window [15].

7.1 Material and Methods

7.1.1 Simulated Data

Clinical data consisted of 37 fPCG simulated tracings corrupted by different levels of noise (i.e. characterized by different signal-to-noise ratios; SNR), as in real recordings. The recordings are 8 min long, characterized by a fHR of 140 bpm and belong to the "Simulated Fetal PCGs database" of PhysioNet [16] freely accessible on the web under the ODC Public Domain Dedication and License v1.0. SNR included between -26.7 dB and -4.4 dB. Simulated FPCG were generated (sampling frequency: 1kHz) as sequences of simulated S1 and S2 heart sounds to which corrupting noise was added. Noise is a sum of different contributions: maternal heart sounds, maternal body organs sounds, fetal movements, surrounding environment and additive white Gaussian noise.

7.1.2 Experimental Data

Experimental data are taken from the Shiraz University (SU) fetal heart sounds database of PhysioNet [16] freely accessible on the web under the ODC Public Domain Dedication and License v1.0., which contains fetal and maternal PCG recordings from 109 pregnant women [17], but only fetal ones are considered in this thesis. This database was constructed using recordings made from 109 pregnant women (mothers aged from 16 to 47 years) with a digital JABES Electronic stethoscope (GS Technology Co. Ltd., South Korea) placed on the lower maternal abdomen [16]. In the case of twins (seven cases) the data were collected twice according to the locations advised by an expert gynecologist. Audacity cross-platform audio software was used for recording and editing the signals on a PC. In total, 99 subjects had one signal recorded, 3 subjects had two and seven cases of twins were recorded individually, resulting in 119 total recordings. The average duration of each record is about 90 seconds. The sampling rate was generally 16 kHz with 16-bit quantization. The data was recorded in wide-band mode of the digital stethoscope, with a frequency response of 20 Hz to 1 kHz.

7.2 PCG-Delineator algorithm

PCG-Delineator is an efficient algorithm for automatic HSs detection in FPCG. It is characterized by two consecutive steps: noise removal by WT filtering and fHSs iterative detection. A detailed description of each step is reported below.

Wavelet Transformation Filtering: PCG-Delineator performed a FPCG filtering by means of a WT-based procedure, a time-frequency approach to signal decomposition. WT is a processing method that quantifies temporal changes of the frequency content of non-stationary signals, such as reported in chapter 4. WT approach offers better temporal resolution and scale (frequency) resolution when analyzing high frequency component and low frequency components respectively. WT decomposes a signal into several multiresolution coefficients and performs a series of high- and low-pass filter operations followed by down-sampling. WT preserves signal by operating only on those selected regions of the bandwidth that need filtering. Denoising algorithm uses statistical regression of noisy

coefficients over time to obtain a nonparametric estimation of the reconstructed signal without noise. Thus, PCG-Delineator for denoising decomposed the corrupted signal into several levels. The decomposition processing allows to remove the level which seriously corrupted by noise. In level decomposition, wavelet coefficients tend to be much larger than those due to noise. Thus, coefficients below a certain level are regarded as noise and they are thresholded out. Then, the signal can be reconstructed without significant loss of information in the signal content. As WT is sensitive to noise level, WT-procedure requires appropriate selection of wavelet family, level of decomposition, and threshold for having better accuracy. In this work, decomposition, denoising and reconstruction were performed by mother wavelet Coiflets of 4th order with 7 levels of decomposition and soft threshold, providing the higher result for signal to noise ratio for all types of FPCG signal. Details of wavelet denoising algorithm are reported in [13].

fHSs Iterative Detection. According to PCG-Delineator, S1 and S2 sounds are detected from WT-denoised FPCG. PCG-Delineator allowed to recognize all heart spikes and to identify which of them are S1 and which are S2. The PCG-Delineator algorithm to detect S1 and S2 sounds is a threshold-based. Initially, S1 detection procedure set an amplitude threshold as 30% of the filtered FPCG signal maximum amplitude, under the condition that at least 40ms separate two consecutive S1 sounds. This time condition allows to remove possible S1 detections with no physiological meaning. In literature, it has been reported that, in non-pathological cases, S2 follow S1 in a heart cycle [7]. Consequently, S2 identification procedure, which is also based on a time-threshold, is performed after S1 detection. Specifically, S2 identification is based on the consideration that diastolic duration (i.e. time distance between S2 and S1 sounds) is longer than systolic duration (i.e. time distance between S1 and S2 sounds) [18]. Thus, S2 detection procedure is threshold-based in both time and amplitude, under the conditions that S2 has to fall at least 100ms after preceding S1 and at most 200ms before successive S1, and that S2 has to have an amplitude lower than 80% that of preceding S1.

PCG-Delineator works iteratively: first, all potential S1 peaks are identified; then, distances between S1 peaks are computed to make a further control in time, in order to find all the S1 peaks

that were not included in the first evaluation; once all S1 peaks have been localized and confirmed, S2 peaks are identified; eventually, S2 are confirmed by verifying their amplitude.

Block diagram of PCG-Delineator is depicted in Fig. 7.1.

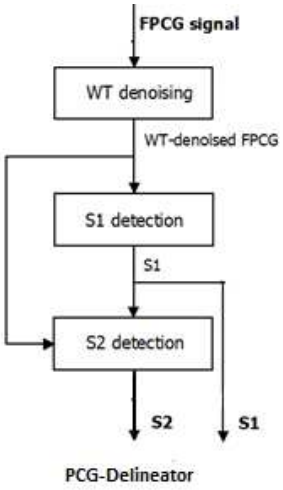

Fig. 7.1. The block diagram of PCG-Delineator.

7.3 Detection of S1 sound using WT scalogram function

The S1 sounds are also detected using the WT-Scalogram function. The WT coefficients of the FPCGs are computed using the scale interval 1:100. Then, a contour representation of the Scalogram, which represents the percentage of energy for each coefficient, is performed for each window. The scalogram function allow to detect S1, considering the minimum peak-to-peak distance of S1 is long 0.4 s. Block diagram of the detection of S1 sound using WT scalogram function is depicted in Fig. 7.2:

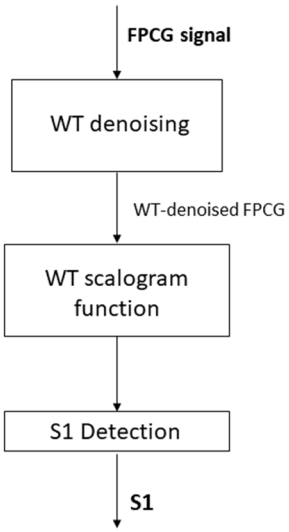

Fig. 7.2. The block diagram of the detection of S1 sound using WT scalogram function.

7.4 Fetal Heart Rate extraction

The FHR extraction and the mean FHR for each window are performed for both the PCG-Delineator and the WT-Scalogram. The FHR is computed as reported in the Eq.1 where 'fs' is the sampling frequency and 'cardiaccycle' is the difference between two consecutive S1 peaks of each window.

Then, among all the extracted FHR in each window, the mean FHR is found.

$$FHR = 60 * fs/cardiaccycle \quad (1)$$

The validation of PCG-Delineator and WT-Scalogram is performed considering the mean fHR for both simulated and experimental signals. For simulated recordings, PCG-Delineator and WT-Scalogram are compared between themselves and each algorithm with the so-called annotations. The annotations are done by an accurate visual inspection of the windows in order to find and correct all the missing S1 peaks, allowing the right extraction of the fHRs. For experimental recordings, PCG-Delineator and WT-Scalogram are compared between themselves and each algorithm is compared to

the annotations, given by the average fHR over windows of 10 seconds using a simultaneous cardiotocography analysis (CTG), reported in [17].

Moreover, a percentage of the elaborated windows is calculated by applying the Eq.2, in which '#W' stands for the percentage of the elaborated windows, 'NTOT' indicates the total number of the windows and 'NaN' is the number of windows containing a not-a-number value.

$$\#W = [(NTOT - NaN)/NTOT] * 100 \quad (2)$$

In addition, the annotations, the PCG-Delineator signals and the WT-Scalogram signals are also described in terms of 50^{th} [25^{th};75^{th}] percentiles.

7.5 Statistics

Since original simulated signals and noise amplitudes were not available to reproduce the signal-to-noise ratio (SNR) values reported in the database, they were recomputed according to the following definition [13] (Eq.3):

$$\mathrm{SNR} = 20 \cdot \mathrm{Log}\left(\frac{\mathrm{PeaktoPeak\ \ fPCG}}{4 \cdot \mathrm{std(fPCG)}}\right) \quad (3)$$

where PeakToPeakfPCG is a signal-measure representing maximum-minus minimum amplitudes of the S1 and std(fPCG) is a noise-measure representing the fPCG standard deviation. SNR values were computed before (SNRbefore) and after (SNRafter) WT filtering. In order to evaluate their correctness, the Pearson correlation coefficient (ϱ) was computed. Automatic S1 and S2 detections were compared against provided manual annotations and then they were classified as true positives, false positives and false negatives in order to quantify detection accuracy by means of

sensitivity (SE) and positive predictive value (PPV). To compare the fHR extracted by PCG-Delineator, WT-Scalogram function and annotations, a Wilcoxon two-sided Rank-Sum test is performed, after verifying the non-normality of some distributions with Lilliefors test (it is sufficient that, at least, one distribution is non-normal). Statistical difference was set at $p< 0.05$.

7.6 Results

7.6.1 Simulation study: PCG-Delineator

Computed SNR values ranged from -1.1dB to 7.4dB and were strongly correlated ($\varrho=1.0$; $P<10^{-200}$) with those provided in the database. PCG-Delineator was able to drastically reduce noise. Indeed, after its application, SNR increased significantly (12.9÷17.9dB; $P<10^{-14}$). A qualitative example of raw and denoised FPCG signal is reported in Fig. 7.3 that displays raw FPCG signals with three different level of SNR (-4.4, -16.6, and -22.6 dB, grey line) and corresponding denoised FPCG signals after WT filtering (black line), respectively. Moreover, PCG-Delineator reliably detected location and morphology of the fHSs. Quantitative results relative to the performance of fHSs detection are reported in Table 1. SE and PPV values are both 100% for S1, and 91% and 80%, respectively for S2. Eventually, for S1, SE and SNR are associated by a low but significant ($\varrho=0.66$, $P<0.05$) correlation.

Table 1. Statistics of fHSs detection by PCG-Delineator. SE, PPV and ϱ (for SEvsSNR and PPVvsSNR) values for S1 and S2 are reported. *: P<0,05

	S1	S2
SE (%)	100 [99 ; 100]	91[88;99]
PPV (%)	100[100 ; 100]	80[65;85]
SNR (dB)	15.9 [15.2; 16.3]	15.9 [15.2; 16.3]
SEvsSNR (ϱ)	0.18	0.66*
PPVvsSNR (ϱ)	0.23	0.20

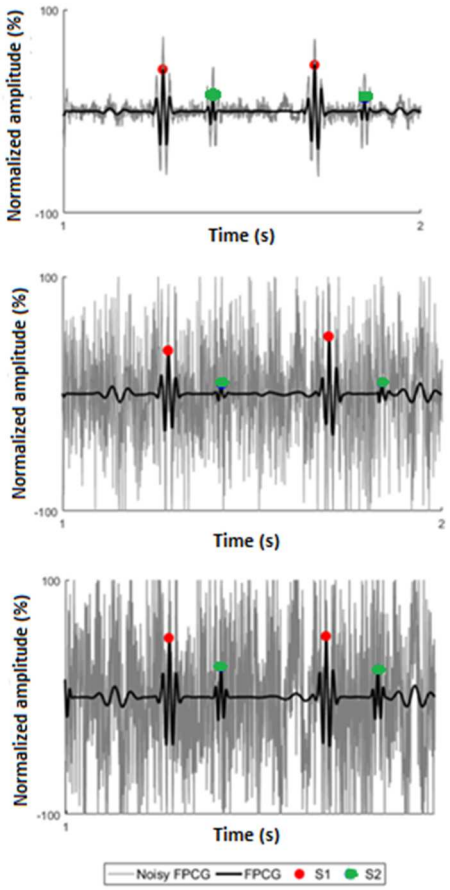

Fig. 7.3. S1 and S2 sound detection (red and green bullets, respectively), after the noise level was drastically reduced.

7.6.2 S1 extraction with PCG-Delineator and WT-Scalogram: Fetal Heart Rate assessment

For the extraction of fHR, PCG-Delineator was applied to detect S1 in a window of 10 s (Fig. 7.4) for a representative signal of simulation study. In the y axis there is the normalized signal. The samples are reported in x axis: since the sampling frequency is 1000 Hz, a window of 10 s corresponds to a window of 10000 samples.

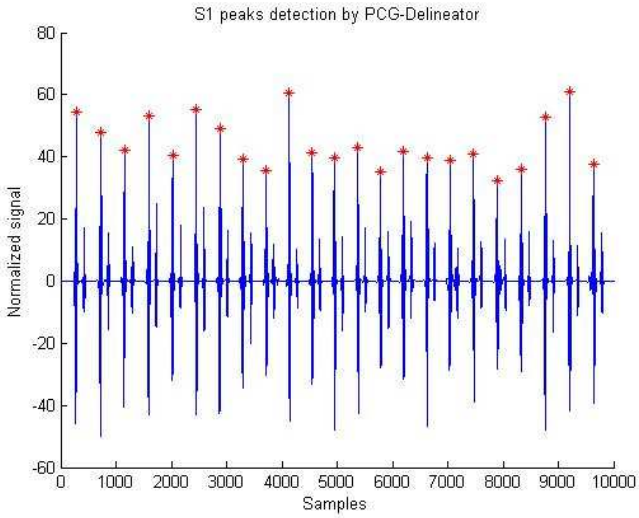

Fig. 7.4. S1 peaks detection by PCG-Delineator in a window of 10 s.

Instead, S1 peaks are detected by means of the Scalogram function in a window of 10 s (Fig. 7.5), for a representative signal of simulation study. The scales a, related to frequency, are reported in y-axis. The samples are reported in x-axis: since the sampling frequency is 1000 Hz, a window of 10 s corresponds to a window of 10000 samples.

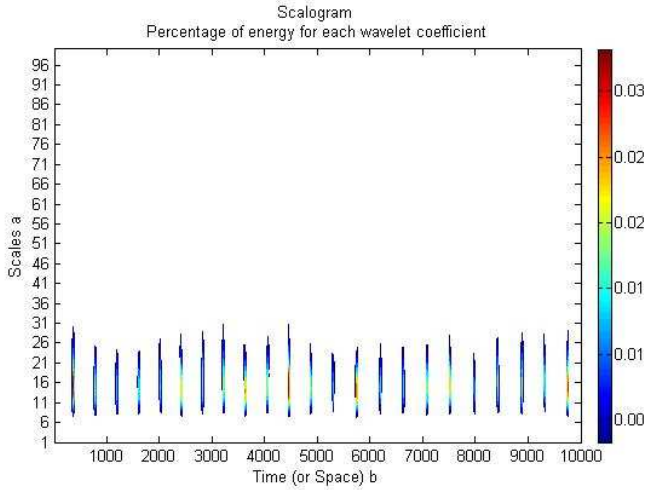

Fig. 7.5. S1 peaks detection by Scalogram in a window of 10 s.

For a representative signal of experimental study, PCG-Delineator was applied to detect S1 in a window of 10 s (Fig. 7.6). In the y-axis there is the normalized signal. The samples are reported in x-axis: since the sampling frequency is 16000 Hz, a window of 10 s corresponds to a window of 160000 samples.

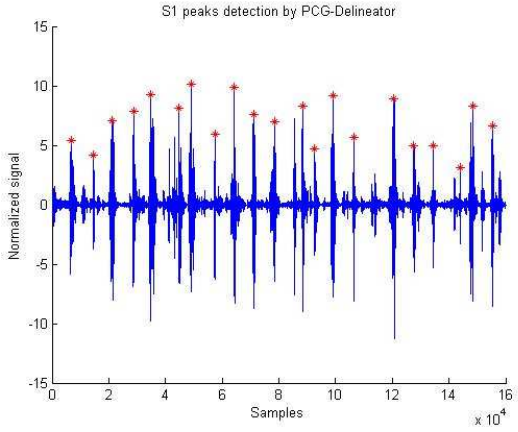

Fig. 7.6. S1 peaks detection by PCG-Delineator in a window of 10 s length.

Instead, S1 peaks are detected by means of the Scalogram function in a window of 10 s (Fig. 7.7), for a representative signal of simulation study. The scales a, related to frequency, are reported in y-axis. The samples are reported in x-axis: since the sampling frequency is 16000 Hz, a window of 10 s corresponds to a window of 160000 samples.

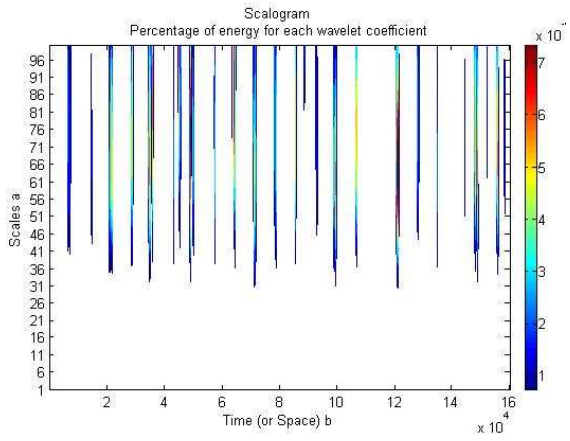

Fig. 7.7. S1 peaks detection by Scalogram in a window of 10 s length.

The validation of PCG-Delineator and WT-Scalogram is performed considering the mean fHR for both simulated and experimental signals. For simulated recordings, PCG-Delineator and WT-Scalogram are compared between themselves and each algorithm with the so-called annotations. The annotations are done by an accurate visual inspection of the windows in order to find and correct all the missing S1 peaks, allowing the right extraction of the fHRs. For experimental recordings, PCG-Delineator and WT-Scalogram are compared between themselves and each algorithm is compared to the annotations, given by the average fHR over windows of 10 seconds using a simultaneous CTG, reported in [17].

After the estimation of percentage of the elaborated windows #W, the comparison between fHR extracted from PCG-Delineator, WT-Scalogram and annotation is performed, such as reported in Table 2 for simulation study and Table 3 for experimental study, respectively.

Table 2: Percentage of the elaborated windows #W, the comparison between fHR extracted from PCG-Delineator, WT-Scalogram and annotation.

		#W	FHR	ANN.	PCG-D.	SCAL.
SIMULATION STUDY	ANN.	100%	141 [140 ; 141]	1		
	PCG-D.	100%	140 [140 ; 141]	P=0,3091	1	
	WT- SCAL.	100%	140 [137 ; 144]	P=0,7913	P=0,7854	1

Table 3: Percentage of the elaborated windows #W, the comparison between fHR extracted from PCG-Delineator, WT-Scalogram and annotation.

		#W	FHR	ANN.	PCG-D.	SCAL.
EXPERIMENTAL STUDY	ANN.	62,27%	141 [135 ; 149]	1		
	PCG-D.	90,91%	140 [136 ; 144]	P=0,6018	1	
	WT- SCAL.	81,97%	136 [135 ; 145]	P=0,4555	P=0,7962	1

7.7 Discussion and Conclusion

The non-invasive measurement of fHSs is of great clinical relevance to assess fetal wellbeing. Its automatic analysis allows to overcome issues related to subjectivity and physician experience, which may bias diagnoses.

The first part of the study is the application of PCG-Delineator to FPCG signals affected by varying levels of noise, in order to test the goodness of this algorithm for automatic fHSs detection. First of all, PCG-Delineator has been applied to "Simulated Fetal PCGs database" of PhysioNet [16] containing 37 simulated FPCG affected by different levels of noise (original SNR ranged from -26.7 dB and -4.4 dB). Original and recomputed SNR values were perfectly correlated (ϱ=1.0; P<10-200), indicating that they provide the same amount of information. To denoise FPCG signals, PCG-Delineator was based on WT approach, using Coiflets mother wavelet (4th order, 7 levels of decomposition). WT filtering significantly increased SNR values ($P<10^{-14}$) and SNR values before and after WT filtering were associated by a low correlation coefficient, indicating that WT filtering is very robust to noise. Denoised FPCG were perfectly aligned (same S1 and S2 location); thus, WT filtering introduces no signal delay and maintains unaltered FPCG characteristics. As shown in Fig. 7.3, noise level was drastically reduced and fHSs becomes always visible; still, some noise survived to filtration, especially in signals initially characterized by very low SNR. In spite of this, PCG-Delineator application provided to accurately detect both S1 and S2 from WT-filtered FPCG.

Moreover, S1 sound are also identified using PCG-Delineator and WT-Scalogram approach, for both simulated and experimental data. Experimental data are taken from the Shiraz University (SU) fetal heart sounds database of PhysioNet [16] freely accessible on the web under the ODC Public Domain Dedication and License v1.0., which contains fetal and maternal PCG recordings from 109 pregnant women [17]. The detection of S1, through PCG-Delineator and WT-Scalogram, allow to assess the fHR. These two methods are compared with the annotation given by simultaneous CTG, reported in [17]. For simulation study, annotation, PCG-Delineator and WT-Scalogram showed the same percentage of elaborated window and a comparable value of fHR. For experimental study, PCG-Delineator and WT-Scalogram were able to detect a higher percentage of elaborated

window than annotation and a comparable value of fHR. Thus, these techniques can be a promising fHSs segmentation tool, in order to evaluate the fetal heart functionality.

Chapter references

[1] S. B. Thacker, D. Stroup, and M. Chang, "Continuous electronic heart rate monitoring for fetal assessment during labor," in *Cochrane Database of Systematic Reviews*, 2006.

[2] E. Ryo, K. Nishihara, S. Matsumoto, and H. Kamata, "A new method for long-term home monitoring of fetal movement by pregnant women themselves," *Med. Eng. Phys.*, 2012.

[3] "Fetal Heart Monitoring," *Nurs. Womens. Health*, 2015.

[4] F. Kovács, C. Horváth, Á. T. Balogh, and G. Hosszú, "Fetal phonocardiography-Past and future possibilities," *Comput. Methods Programs Biomed.*, 2011.

[5] A. K. Tiwari and V. Chourasia, "A review and comparative analysis of recent advancements in fetal monitoring techniques," *Crit. Rev. Biomed. Eng.*, 2008.

[6] P. J. Arnott, G. W. Pfeiffer, and M. E. Tavel, "Spectral analysis of heart sounds: Relationships between some physical characteristics and frequency spectra of first and second heart sounds in normals and hypertensives," *J. Biomed. Eng.*, 1984.

[7] P. Várady, L. Wildt, Z. Benyó, and A. Hein, "An advanced method in fetal phonocardiography," *Comput. Methods Programs Biomed.*, 2003.

[8] S. Sun, Z. Jiang, H. Wang, and Y. Fang, "Automatic moment segmentation and peak detection analysis of heart sound pattern via short-time modified Hilbert transform," *Comput. Methods Programs Biomed.*, 2014.

[9] S. E. Schmidt, C. Holst-Hansen, C. Graff, E. Toft, and J. J. Struijk, "Segmentation of heart sound recordings by a duration-dependent hidden Markov model," *Physiol. Meas.*, 2010.

[10] D. B. Springer, L. Tarassenko, and G. D. Clifford, "Logistic regression-HSMM-based heart sound segmentation," *IEEE Trans. Biomed. Eng.*, 2016.

[11] X. Wang, Y. Li, C. Sun, and C. Liu, "Detection of the first and second heart sound using heart sound energy," in *Proceedings of the 2009 2nd International Conference on Biomedical Engineering and Informatics, BMEI 2009*, 2009.

[12] S. R. Messer, J. Agzarian, and D. Abbott, "Optimal wavelet denoising for phonocardiograms," *Microelectronics J.*, 2001.

[13] B. Sbrollini, A., Strazza, A., Caragiuli, M., Mozzoni, C., Tomassini, S., Agostinelli, A., Morettini, M., Fioretti, S., Di Nardo, F., "Fetal Phonocardiogram Denoising by Wavelet Transformation: Robustness to Noise," *Comput. Cardiol. (2010).*, vol. 44, pp. 1–4, 2017.

[14] A. Strazza, A. Sbrollini, V. Battista, R. Ricci, L. Trillini, I. Marcantoni, M. Morettini, S. Fioretti, and L. Burattini, "PCG-Delineator: an Efficient Algorithm for Automatic Heart Sounds Detection in Fetal Phonocardiography," in *Computing in Cardiology*, 2018.

[15] D. D. Taralunga and M. Ungureanu, "Fetal Heart Rate Estimation from Phonocardiograms Using an EMD Based Method," in *RECENT ADVANCES in COMPUTER SCIENCE*, 2015, no. July.

[16] A. L. Goldberger, L. A. N. Amaral, L. Glass, J. M. Hausdorff, P. C. Ivanov, R. G. Mark, J. E. Mietus, G. B. Moody, C.-K. Peng, and H. E. Stanley, "PhysioBank, PhysioToolkit, and PhysioNet : Components of a New Research Resource for Complex Physiologic Signals," *Circulation*, 2000.

[17] M. Samieinasab and R. Sameni, "Fetal phonocardiogram extraction using single channel blind source separation," in *ICEE 2015 - Proceedings of the 23rd Iranian Conference on Electrical Engineering*, 2015.

[18] E. Koutsiana, L. J. Hadjileontiadis, I. Chouvarda, and A. H. Khandoker, "Fetal Heart Sounds Detection Using Wavelet Transform and Fractal Dimension," *Front. Bioeng. Biotechnol.*, 2017.

Part 2

Chapter 8

STATISTICAL GAIT ANALYSIS

A novel and efficient technique, CODE algorithm, has been developed for assessing co-contraction between two antagonist muscles, based on WT cross-energy localization in time-frequency domain of sEMG signal, during walking (Part I). The satisfactory algorithm accuracy and precision in co-contraction detection and physiological reliability of experimental results could support the suitability of CODE tool for future clinical applications.

This second part of the study is aimed at providing a physiological picture of muscular co-contraction mechanism during walking in different populations. The Statistical Gait Analysis technique seemed to be suitable to this purpose. Statistical Gait Analysis is a recent and efficient technique, able to provide a statistical characterization of gait, by averaging spatial-temporal and sEMG-based parameters over hundreds of strides during the same walking trial of each subject. In the present study, Statistical Gait Analysis has been adopted to provide reference data on lower-limb-muscle co-contraction during heathy adult and child walking. Thigh muscle co-contraction, also evaluated for gender, are assessed for adult walking. For child, the analysis performed is based on the quantification of gender-related differences in myoelectric activity of ankle muscle, of thigh muscle co-contraction, and of intrinsic and extrinsic muscle co-contraction, for a global understanding of muscular recruitment during school-age children walking.

8.1 Introduction

Co-contraction activity of lower limb muscles during walking allows to enhance the ligament maintenance of joint stability, providing resistance to rotation at a joint and equalizing pressure distribution at the articular surface [1]. The development of torque by a single, unopposed agonist muscle group about a joint creates an uneven pressure distribution over the articular surfaces. Co-contraction of an antagonist muscle group would, therefore, aid in the distribution of forces at the articular surface and simultaneously increase joint stability by increasing the degree of bone-to-bone fit of the articular ends. It is acknowledged that muscle co-contraction has an important role in movement regulation during motor learning activities, enhancing joint stability [2], in particular ankle and knee joint stability. The analysis of ankle muscle co-contraction is very extensive in literature, including previous studies of the present research group that provided normative data stratified also by gender [3] [4]. A similar analysis is missing for antagonist knee muscles. Knee joint is worth to be analyzed since it is relatively weak and susceptible to injury [2], for its anatomical position and complexity. Knee joint relies on muscles and ligaments to ensure stability. During walking, the knee joint is primarily regulated by the hamstrings and quadriceps femoris (QF) groups [5]. Contraction of quadriceps muscles represents the primary absorbing mechanism of impact during weight acceptance. In stance, extensors act to decelerate knee flexion, while in swing they contribute to limb progression [5]. At knee joint, hamstrings are mainly involved in knee flexion control. During walking, hamstrings serve as a useful protective function in preventing knee hyperextension in terminal swing and in following early stance [5]. QF and hamstring are antagonist muscle groups for knee joint during walking. Thus, one of the main purposes of this second part of the present study has been providing reference data on co-contraction activity of also QF vs. hamstrings muscles, in order to complete the information achieved at ankle joint [6]. In a second phase, a gender-related analysis of these co-contractions was also accomplished, as for ankle joint.

Triceps surae muscles have been investigated regarding their effect on the knee joint [7], despite their principal function is exerted on the ankle joint. It is well-known that heads of gastrocnemius (GL) originate on medial and lateral femur condyles, inserting on the calcaneus, and its proximal tendon

covers the posterior side of the tibia and exerts a direct flexor activity on the knee joint [7]. Many works investigated the way gastrocnemius activity affects anterior cruciate ligament (ACL) elongation, reporting a clear antagonist function [8][9]. Moreover, co-contraction of GL and thigh muscles is recognized as a fundamental mechanism for both stabilizing the knee joint and reducing the reliance on ACL [10][11]. Nevertheless, to authors' knowledge no previous studies investigated the possible co-contraction activity between gastrocnemius and knee-extensor muscles during able-bodied walking. Thus, the third phase of this study on lower-limb-muscle co-contraction in adults focused on assessing the co-contraction activity between GL and VL during walking in a young healthy adult population, attempting to provide a reference frame for this co-contraction, able to include the physiological variability of the phenomenon [12]. For this study, VL was chosen as representative of QF group because of its pure knee extensor function.

Muscle co-contractions are particularly relevant in analyzing also children pathologies such as spastic cerebral palsy [13][14]. In typically-developing subjects, co-contraction occurred in tasks requiring motor coordination and joint stability [15]. In pathologic conditions, co-contraction was also implicated as a cause of inefficient or abnormal movement, especially in neuromuscular pathologies [14]. To provide a deeper comprehension of children neuromuscular pathologies, a systematic study on muscle activity and co-contraction would be suitable. To correctly interpret surface electromyography in pathological conditions, indeed, reliable normative data in non-pathological children are required for direct comparison. Recent studies provided an attempt for developing a normative surface-EMG dataset for ankle-muscle co-contractions during school-age-children walking [16]. For a global understanding of muscular co-contraction activity in healthy school-age children, it is useful to quantify also co-contractions between quadriceps femoris (QF) and hamstring muscles during walking. This has been one of the purposes of this part of the present study focused on children [17]. The analysis of muscular co-contraction in lower limbs in children has been completed in the present study, focusing on the foot, and in particular on the reciprocal role of intrinsic (extensor digitorum brevis, EDB) and extrinsic foot muscles (tibialis anterior and gastrocnemius lateralis) [18].

Normative data on muscular activation/co-activation in children could be used for studying the different stages of gait maturation. The role of gender in the evolution of gait could be a further factor

worth of investigation. To this aim, the final part of the present study on school-age children has involved an analysis of sEMG signal stratified for gender and a consequent comparison with same data assessed in adults [19].

8.2 Materials and methods

8.2.1 Subjects

Assessment of thigh muscle co-contractions and consequent gender-related differences during adult walking.

Thirty able-bodied young adults were recruited. Mean (±SD) anthropometric characteristics of the sample population are: age 23.8±1.9 years; height 173±10 cm; weight 63.3±12.4 kg; body mass index (BMI) 20.8±2.1 $kg \cdot m^{-2}$ [6] . The same population is also recruited for the detection of co-contraction patterns of gastrocnemius and quadriceps femoris in controlling the knee joint during walking [12].

Assessment of thigh muscle co-contractions during child gait.

For the analysis of thigh muscle co-contractions in children walking, gait data from 100 healthy children (49 females and 51 males) were retrospectively analyzed (age 9.0 ± 1.4years; age-range 6.5–11.4 years; height 133 ± 9cm; mass 30.6 ± 6.7kg; BMI- range 13.7±24.1 kg/m^{-2}) [3]. Children group was characterized by following age distribution: 10 children of 6–7 years (mean age 80.3 ± 2.1months); 19 children of 7–8 years (90.7 ± 3.7months); 22 children of 8–9 years (102.9 ± 2.9months); 22 children of 9–10 years (115.4 ± 3.2months); and 27 children of 10–11.5 years (127.4 ± 4.6months) [17].

Assessment of the reciprocal role of intrinsic and extrinsic muscles of the foot.

Data from 23 healthy school-age children were analyzed. The children were carefully selected to consider only able-bodied subjects, to analyze a specific, narrow age-range (school-age children from 6–10 years old, mean ± SE, age 8.2 ± 1.1 years), to preserve a balanced male/female ratio (12 females

and 11 males), and to avoid overweight and obesity as confounders (height 129 ± 3 cm; mass 28.4 ± 1.9 kg) [18].

Evaluation of gender effect on muscular recruitment during children walking.

For the analysis of gender effect on ankle muscle co-contractions in children walking, a retrospective study was performed, analyzing gait data from 133 healthy subjects. Subjects were divided into two groups. C-group was composed of one hundred children (49 females and 51 males, 6–11 years), originally presented in Agostini et al. [12]. YA- group was composed of and 33 young adults (17 females and 16 males, 20-30 years). Mean (± standard deviation) characteristics are: age 108.2 ± 16.3 months, height 133 ± 9 cm and, mass 30.6 ± 6.7 kg for C-group; age 23.9 ± 1.9 years, height 174 ± 10 cm, and mass 63.3 ± 12.4 kg for YA-group [19].

Participants with a previous medical history involving foot or ankle surgery, inflammatory arthritis, neuromuscular disease, balance disorders, or an inability to walk unaided were excluded from the study. Adult participants signed informed consent. For children, parental consent and child assent were obtained. Children are not able to provide true informed consent until they turn 18. Thus, before taking part in trials, they are asked for their assent. Assent means that they agree to take part. They may also dissent, which means they do not agree. In that case, the child was excluded from the study. All the research was undertaken in compliance with the ethical principles of the Helsinki Declaration and approved by the Institutional Expert Committee.

8.2.2 Signal acquisition

sEMG signal was acquired (sampling rate: 2 kHz, resolution: 12 bit) by a multichannel recording system, Step32 (Version PCI-32 ch2.0.1. DV), Medical Technology, Italy. The employed sampling rate ensures, according to the Nyquist criterion, the detection of the full spectrum of the sEMG signal, that spans up to 500 Hz. Each lower limb was instrumented with an electro-goniometer, three footswitches and two sEMG probes. The electro-goniometer (accuracy: 0.5 deg) was placed on the lateral side of the

limb, to measure knee joint angle in the sagittal plane. The foot-switches (surface: 1.21 cm2, activation force: 3 N), were pasted beneath the heel, the first and the fifth metatarsal heads of the foot. Single differential sEMG probes with fixed geometry were placed on the muscle belly to detect the sEMG signals (Ag/Ag-Cl disk; electrode diameter: 0.4 cm; inter-electrode distance: 0.8 cm; gain: 1000; high-pass filter: 10 Hz; input impedance: 1.5 GΩ; CMRR: 126 dB; input referred noise: ≤ 1μVrms). sEMG signals were further amplified and low-pass filtered (linear-phase FIR filter, cut-off frequency: 450 Hz) by Step32. Skin was shaved, cleansed with abrasive paste and wet with a soaked cloth. Probes were placed over ankle (TA,GL) and thigh (RF,VL,MH) muscle and EDB muscle following the SENIAM recommendations [20] for electrodes location with respect to tendons, motor points and fiber orientation. Each volunteer walked barefoot at preferred speed for about 5 minutes, following an eight-shaped path.

8.2.3 Signal processing

Footswitch signals were debounced, converted to four levels corresponding to Heel Strike (H), Flat Foot Contact (F), Push-off (P) and Swing (S) and processed to identify the different gait cycles (GC) [21] . Stride interval has been computed as the distance (in a number of samples) between the initial samples of the heel contact phase and the initial samples of the heel contact phase of the following stride. Electro-goniometric signals were low-pass filtered (FIR filter, 100 taps, cut-off frequency 15 Hz). Step32 software automatically removes outlier cycles relative to direction changes, including deceleration before the turning and acceleration after it. More specifically, the electro-goniometric signal and the duration of the gait phases are used by a multivariate statistical filter to discard outlier cycles, i.e. cycles with improper sequences of gait phases and strides with the proper sequence of gait phases (HFPS) but with abnormal timing (such as those relative to deceleration, reversing, and acceleration). The algorithm has the following steps:

(1) A total of six variables are considered to build the multivariate data set: duration of H, F, P, and S gait phases and knee-joint angle at 70% and 95% of the gait cycle.

(2) The multivariate (Mahalanobis) distance between each gait cycle and the average gait cycle is calculated.

(3) Outlier cycles are discarded, i.e. cycles that have a very high Mahalanobis distance with respect to the average gait cycle: this is determined using a Hotelling t-test for multivariate data, choosing a confidence level $\alpha = 0.05$.

(4) The average gait cycle is re-calculated.

(5) The previous steps are iterated until all outlier cycles are removed.

sEMG signals were processed by a high-pass, linear-phase FIR filter (100 taps, cutoff frequency: 20 Hz), in order to avoid phase distortion effects. The cut-off frequencies of the resulting band-pass filtering (20 – 450 Hz) were chosen in order to remove movement artifact noise and avoid loss of information from the sEMG signal full bandwidth. Moreover, the sEMG signals were processed by a double-threshold statistical detector, to identify muscle activation intervals [22]. The double-threshold algorithm first selects two threshold values, ζ and r0 and then considers m successive samples. The probability that at least r0 samples out of m cross ζ, is given by (Eq.1):

$$Pr_0\ (r \geq r_0; m) = \sum_{k=r0}^{m} \binom{m}{k} P^k (1-P)^{m-k} \quad (1)$$

where P is the probability that a single sample crosses the threshold [22]. Whether at least r_0 out of m consecutive samples are above the ζ value, the presence of muscle activation is acknowledged. The probability that noise samples are recognized as signal is defined by (Eq.2):

$$Pf_a\ (r \geq r_0; m) = \sum_{k=r0}^{m} \binom{m}{k} P_\zeta^k (1-P_\zeta)^{m-k} \quad (2)$$

where P_ζ is the probability that a specific noise sample is above the fixed threshold [22] and depends on the noise variance σ_n^2 (Eq. 3)

$$P_\zeta = e^{-\zeta/2\sigma n^2} \quad (3)$$

A main improvement of a double threshold statistical detector is that, for a given P_{fa} and m value, it provides a higher detection probability P_d respect to a single threshold detector [22] (Eq. 4):

$$P_d\ (r \geq r_0; m) = \sum_{k=r0}^{m} \binom{m}{k} P_{dk}^{k}(1 - P_{dk})^{m-k} \quad (4)$$

P_{dk} is the probability that a single sample crosses the threshold [22] and it is related to both σ_n^2 and the SNR, according to (Eq. 5):

$$P_{dk} = e^{-\zeta/2\sigma_n^2(1+\frac{10SNR}{10})} \quad (5)$$

The value of the first threshold (ζ) is related to the background noise level, while r_0 is based upon the SNR. Background noise level and SNR are estimated, following the approach reported in [23].

The mean noise power P_{noise} and the mean signal power P_{signal} are computed averaging the histogram bins of an auxiliary time series, obtained considering the sEMG signal as a Gaussian process (Eq.6):

$$P = \sum \frac{bins_i \quad Freq_i}{Freq_i} \quad (6)$$

Depending on which local maximum of the bimodal distribution histogram is considered, P represents the calculated power of noise or signal. The root mean square value of the background noise is computed as follows (Eq.7):

$$e_{noise=\sqrt{P_{noise}}} \quad (7)$$

whereas the SNR is estimated as (Eq.8):

$$SNR = 10 * \log\frac{(\sigma_s^2)}{(\sigma_n^2)} \quad (8)$$

σ_s^2 and σ_n^2 are the variance of signal and noise, respectively.

Footswitch and goniometric signal processing, sEMG-signal filtering, identification of muscle activation intervals and statistical gait analysis in each single subject were off-line performed by Step32 system. Muscular co-activations (including the occurrence frequencies) were assessed as the overlapping periods among activation intervals of the considered muscles in the same strides [24]. A muscular activity shorter than 30 ms does not yield an active control on a joint motion during gait, thus overlapping periods with a time length lower than 30 ms were discarded.

8.2.4 Statistical gait analysis

The statistical gait analysis [25] describes human walking considering the spatial-temporal and sEMG parameters over hundreds of consecutive strides, belonging to the same walking trial. Statistical gait analysis relies on the cycle-dependency of muscle-activation during gait. Thus, sEMG parameters should be averaged considering each single activation modality by itself, i.e. only over onset/offset instants of cycles including the same number of activations. An activation modality is defined as the number of times a single muscle activates during a single gait cycle (GC), i.e. the n-activation modality consists of n active intervals for the considered muscle during a single GC. To get the mean activation intervals for each activation modality, the muscle activations relative to every GC were identified, obtaining their onset/offset instants in temporal space [26]. Then muscle activations were grouped according with the number of active intervals, i.e. relative to their activation modality. Eventually, the onset/offset time instants of each activation modality were averaged separately over the two populations. Averaged onset/offset percentage time instants were normalized with respect to GC, providing mean activation intervals in percentage of GC. The statistical gait analysis allowed quantifying muscle co-contractions not only in terms of the onset-offset muscular activation, but also in terms of the occurrence frequency (OF). The OF is a new parameter for the evaluation of the variability of the myoelectric activity and it is defined as the frequency each muscle activation occurs with, quantified by the number of strides in which the muscle is recruited with that specific activation modality [27] (Eq. 9).

$$\boldsymbol{OF(n) = \frac{Number\ of\ gait\ cycles\ with\ n\ activation\ intervals}{Total\ number\ of\ gait\ cycles}} \tag{9}$$

Thus, the OF allows quantifying if each specific muscle activation is recurrent or negligible during walking. The features extracted from the analyzed EMG signal from each muscle are (1) the onset time instants for each activation interval and co-contraction interval; (2) the offset time instants for each activation interval and co-contraction interval; (3) the occurrence frequency for each activation interval and co-contraction interval; and (4) mean (±SE) onset/offset time instants and the corresponding mean (±SE) occurrence frequency for each activation modality.

8.2.5 Statistics

All data are reported as mean ± standard deviation (SD). Shapiro-Wilk test was used to evaluate the normality of each data distribution. Comparisons between data distributions were performed with two tailed, non-paired Student's t-test between normally distributed samples and with Mann-Whitney U-test between non-normally distributed samples. The analysis of variance (ANOVA) was used to compare the different activation modalities within each gender group for normally distributed samples. Kruskal-Wallis test was used for non-normally distributed samples. ANOVA and Kruskal-Wallis tests were followed by multiple comparison test, according to the Tukey's procedure. To determine the power of an observed effect based on the sample size and parameter estimates derived from data set, the statistical power analysis was performed. To quantify correlations, Pearson's product-moment correlation coefficient and Spearman's rank correlation coefficient were used for populations that were normally and not normally distributed, respectively. Statistical significance was assumed at $p<0.05$.

8.3 Results

8.3.1 Assessment of thigh muscle co-contractions during walking

The assessment of thigh muscle co-contraction during walking provide the following results. For each subject, a mean (± standard deviation, SD) of 454 ± 112 strides has been considered. All the recruited subjects were heel strikers and only gait cycles with the proper sequence of gait phases (H-F-P-S) were considered. Thus, from the total of 16315 strides considered, 1315 strides (8% of total strides) have been removed from the analysis because being outlier cycles relative to deceleration, reversing, and acceleration. The mean (±SD) duration of H, F, P and S phases over our population was computed; the H-phase lasts 5.6 ± 1.7% of the gait cycle, the F-phase 28.9 ± 6.0%, the P-phase 23.4 ± 4.8% and the S-phase 44.1 ± 2.8%. The mean results are reported with data from right and left lower limb considered all together. Statistical gait analysis of the myoelectric signal showed that muscles show a different number of activation intervals in different strides of the same walking. Activation modalities for each muscle are reported in Fig. 8.1.

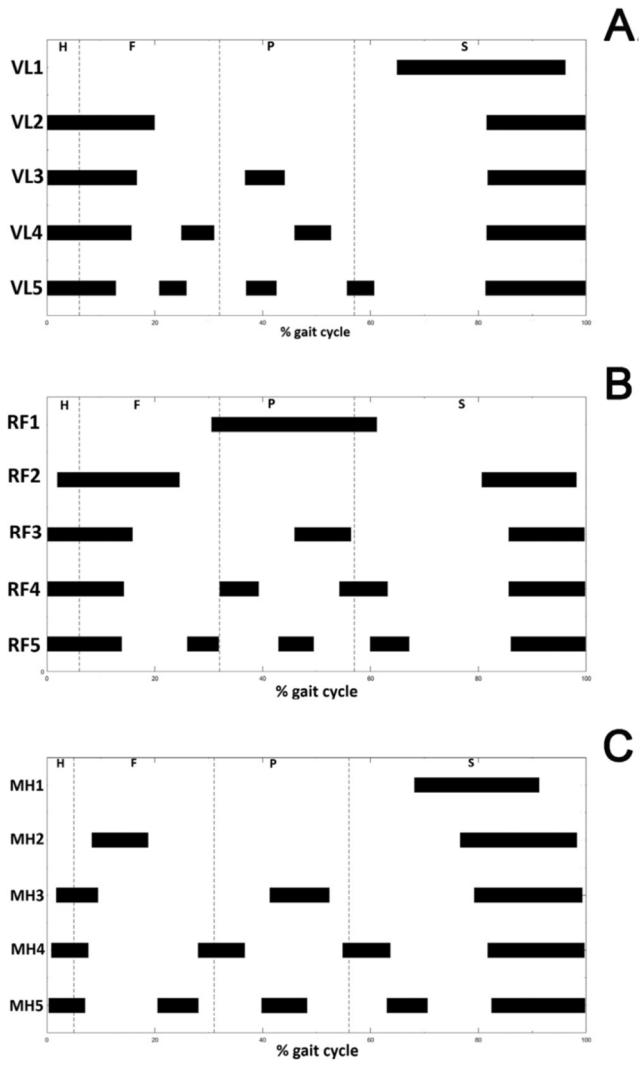

Fig. 8.1. Mean activation intervals vs. percentage of gait cycle for modalities with 1, 2, 3, 4 and 5 activations detected during walking for VL (panel A), RF (panel B), and MH (panel C). H, F, P and S phases are delimited by dashed vertical lines.

Information on muscle co-contraction was given in terms of on-off activation instants, excitation intensity and occurrence frequency. A mean muscle excitation intensity, quantized in three levels, over population was achieved by Step32. The purpose of this quantization is mainly to identify the peak regions of myoelectric activity. The three intensity levels, considered in ascending order, were associated with the value of 1, 2 and 3, respectively. A global quantized mean signal over all subjects, ranging from 0 (no signal) to 90 (maximum value), was obtained for each percentage unit of GC, as the sum of intensity levels of every single mean signal. This global mean signal was subdivided in four intervals ranging from 0 to 12 (no muscle activation), from 13 to 30 (low-level activation), from 31 to 60

(medium-level activation), and from 61 to 90 (high-level activation). Mean activation intervals are then represented by horizontal bars using a three-level grey scale for the excitation intensity; darker shadowing corresponds to increasing intensity of the mean signal, i.e. low-level (light grey), medium-level (dark grey), and high level (black) activation.

Different superimposition intervals between VL and RF activities were detected during GC. In strides characterized by RF double activation (Fig. 8.2, A), superimpositions between RF and VL activation intervals were observed in early stance (1.9 ± 5.4 to 23.3 ± 14.1% of GC) and in terminal swing (81.4 ± 2.9% to GC end). These superimpositions were detected in the two main activation modalities for VL. Also in strides where RF adopted the 3- and 4-activation modalities, superimpositions were observed from terminal swing to the following early stance, for all VL activation modalities (from the beginning to 15.9 ± 5.0% and from 85.6 ± 3.3 to 99.6 ± 0.8% of GC for RF triple activation, Fig. 3B; for RF 4-activation from the beginning to 14.3 ± 3.3% and from 85.6 ± 3.2% to the end of GC, Fig. 8.2, C). In strides characterized by RF 4-activation (Fig. 8.2, C), a further superimposition between VL and RF activation intervals was observed during mid-stance from 36.2 ± 6.8% to 39.3 ± 4.4% of GC, in 6.9 ± 4.9% of considered strides. Occurrence frequencies of RF/VL co-contractions are reported in Fig. 8.2, D.

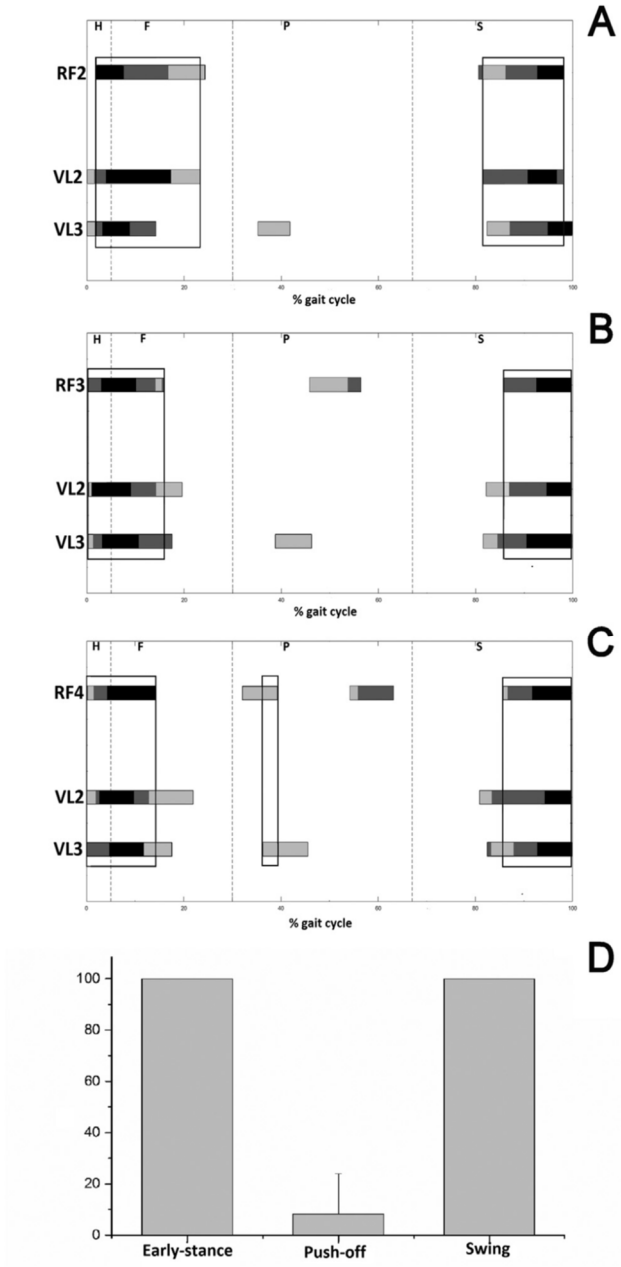

Fig. 8.2. Mean values of VL activation intervals vs. percentage of gait cycle, detected in strides where RF shows 2-activation modality (panel A), 3-activation modality (panel B), and 4-activation modality (panel C). VL activation intervals are reported for modalities with 2 and 3 activations. Mean excitation intensity are represented by using a three-level grey scale; darker shadowing corresponds to increasing intensity of the mean signal, i.e. low-level (light grey), medium-level (dark grey), and high-level (black) activation. VL/RF co-contractions are highlighted by box. Mean (+SD) percentage occurrence frequency of each of the three different VL/RF co-contractions are reported in panel D. H, F, P and S phases are delimited by dashed grey vertical lines.

Different superimposition intervals were detected also between VL and MH activity. In strides with VL double activation (Fig. 8.3, A), superimpositions with the two main MH activation intervals were observed from the beginning to 14.5 ± 10.2% of GC) and from 81.5 ± 3.3% to GC end. Also in strides where VL adopted 3- (Fig. 8.3, B) and 4-activation modality (Fig. 8.3, C), VL/MH superimpositions

were observed from terminal swing to the following early stance, for all MH activation modalities (from the beginning to 15.5 ± 15.1% and from 81.8 ± 3.8 to 99.9 ± 0.1% of GC for VL triple activation; for VL 4-activation from the beginning to 14.8 ± 14.2% and from 81.5 ± 4.1% to the end of GC). In strides with VL triple activation (Fig. 8.3, B), a further VL/MH superimposition was observed from 38.6 ± 12.8% to 44.1 ± 9.6% of GC. Occurrence frequencies of VL/MH co-contractions are reported in Fig. 8.3, D.

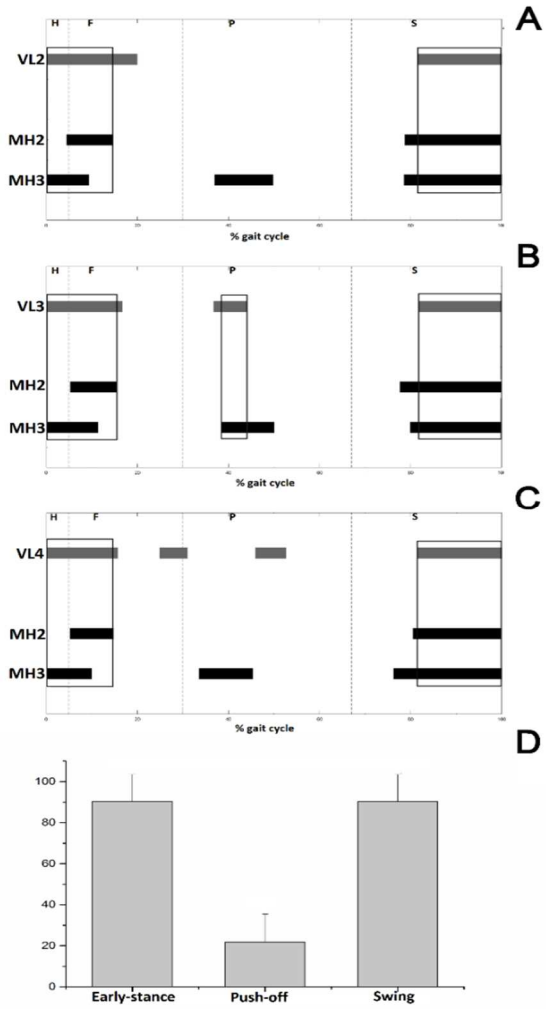

Fig. 8.3. Mean values of MH activation intervals (black bars) vs. percentage of gait cycle, detected in strides where VL (grey bars) shows 2-activation modality (panel A), 3-activation modality (panel B), and 4-activation modality (panel C). MH activation intervals are reported separately for modalities with 2 and 3activations. Mean excitation intensity are represented by using a three-level grey scale; darker shadowing corresponds to increasing intensity of the mean signal, i.e. low-level (light grey), medium-level (dark grey), and high-level (black) activation. VL/MH co-contractions are highlighted by box Mean (+SD) percentage occurrence frequency of each of the three different VL/MH co-contractions are reported in panel D. H, F, P and S phases are delimited by dashed grey vertical lines.

Superimpositions between sEMG activity of RF and MH were also quantified. In strides where RF presented a double, triple, and quadruple activation (Fig. 8.4), a RF/MH superimposition was observed during early stance, for 2-activation (from 1.9 ± 5.4% to 12.5 ± 8.6%), 3-activation (from the beginning of GC to 12.8 ± 6.3%) and 4-activation (from the beginning of GC to 14.3 ± 3.3%) modalities of MH and during swing, for 2-activation (from 80.6 ± 10.7% to 98.2 ± 4.8%), 3-activation (from 85.6 ± 3.3% to the end of GC) and 4-activation (from 85.6 ± 3.2% to 97.8 ± 4.2%) modalities of MH. When RF increases to 3-activation modality, a co-contraction with MH occurs from 45.9 ± 5.3% to 50.7 ± 9.7 of GC (Fig. 8.4, B). Occurrence frequencies of RF/MH co-contractions are reported in Fig. 8.4, D.

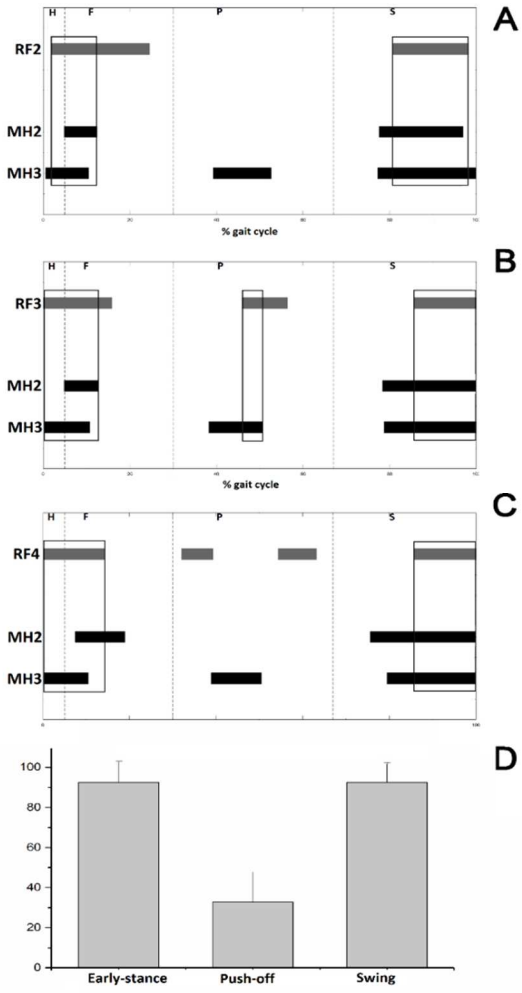

Fig. 8.4. Mean values of MH activation intervals (black bars) vs. percentage of gait cycle, detected in strides where RF (grey bars) shows 2-activation modality (panel A), 3-activation modality (panel B), and 4-activation modality (panel C). MH activation intervals are reported separately for modalities with 2 and 3 activations. Mean excitation intensity are represented by using a three-level grey scale; darker shadowing corresponds to increasing intensity of the mean signal, i.e. low-level (light grey), medium-level (dark grey), and high-level (black) activation. VL/MH co-contractions are highlighted by box. Mean (+SD) percentage occurrence frequency of each of the three different RF/MH co-contractions are reported in panel D. H, F, P and S phases are delimited by dashed grey vertical lines.

Further information on muscle co-contraction was given in terms of excitation intensity. Mean values over 30 subjects of muscle excitation intensity were computed following the procedure reported in "Assessment of excitation intensity" section and depicted by means of a three-level grey scale in Figs. 8.2–8.4. Percentage occurrence frequencies of co-contractions were compared. No significant difference was detected among occurrence frequencies of RF/VL (100%), VL/MH (90.3±13.3%), and RF/ MH (92.4±16.6%) co-contractions in early stance and in swing. RF/ MH co-contraction in push-off showed a significant higher occurrence frequency respect to the other push-off co-contractions. Results of statistical power analysis showed that number of participants (30) guarantees a power>0.90 for every difference tested in the study.

8.3.2 Influence of gender on thigh muscle co-contractions during normal gait

The assessment of gender-related differences on thigh muscle co-contractions provides the following results. For both groups, RF, VL and MH presented three main modalities, covering about 90% of strides and characterized by different occurrence frequencies. Small differences were found between groups in onset/offset instants of activation for each muscle; details were reported in Table 1.

Table 1. Activation intervals of rectus femoris, vastus lateralis and medial hamstrings in its main modalities of activation, expressed as the timing, in the percentage of gait cycle, of signal onset and offset. Values are expressed for female and male population as mean ± standard deviation (SD). **p<0.01 and *p<0.05 between correspondent value in F-group and M-group.

Rectus Femoris	First activation (% of GC)		Second activation (% of GC)		Third activation (% of GC)		Fourth activation (% of GC)	
M-group (n=15)	ON	OFF	ON	OFF	ON	OFF	ON	OFF
2-activation mod	1.9±0.6	22.5±14.5	82.1±9.7	98.1±0.7				
3-activation mod	0±0	15.5±3.9	47.8±4.0*	57.1±5.0**	86.2±2.9	99.9±0.1		
4-activation mod	0.1±0.1	15.0±3.0	34.3±4.8	40.7±4.7	55.8±5.2	64±5.2	85.9±3.1	99.9±0.1
F-group (n=15)								
2-activation mod	1.9±0.4	26.6±14.0	79.1±11.6	98.3±5.0				
3-activation mod	0.2±0.1	16.4±5.9	43.9±5.7*	55.6±6.2**	84.9±3.7	99.6±0.2		
4-activation mod	0.1±0.1	13.5±3.4	29.6±3.9	37.9±3.6	52.6±6.0	62.4±6.3	85.3±3.3	99.7±0.2
Vastus Lateralis	First activation (% of GC)		Second activation (% of GC)		Third activation (% of GC)		Fourth activation (% of GC)	
M-group (n=15)	ON	OFF	ON	OFF	ON	OFF	ON	OFF
2-activation mod	0.2±0.1	20.2±10.6	81.1±3.6	99.8±0.1				
3-activation mod	0±0	17.7±5.9	37.1±9.7	43.8±10.7	81.2±3.8	100±0.0		
4-activation mod	0±0	17.7±5.6**	26.6±6.6	32.5±6.9	47.9±9.9	53.9±10.1	80.9±4.1	99.9±0.1
F-group (n=15)								
2-activation mod	0.6±0.4	19.8±11.2	81.9±2.9	99.7±0.3				
3-activation mod	0.1±0.1	15.8±6.0	36.3±8.4	44.3±8.6	82.3±3.9	99.8±0.2		
4-activation mod	0.1±0.1	13.8±3.8**	23.4±3.8	29.7±4.6	44.1±7.9	51.6±7.9	81.9±4.0	99.9±0.1
Medial Hamstrings	First activation (% of GC)		Second activation (% of GC)		Third activation (% of GC)		Fourth activation (% of GC)	
M-group (n=15)	ON	OFF	ON	OFF	ON	OFF	ON	OFF
2-activation mod	6.8±0.3*	16.4±9.9**	78.5±6.1	98.5±1.4				
3-activation mod	1.7±0.8	9.9±3.5	42.9±14.2**	53.1±13.3	80.7±6.5	99.4±0.6		
4-activation mod	0.4±0.4	7.8±2.9	28.3±10.1	35.7±69.6	54.1±9.3	62.5±9.1	81.2±6.6	99.6±0.1
F-group (n=15)								
2-activation mod	9.8±4.4*	21.5±13.7**	74.9±6.1	97.8±3.5				
3-activation mod	1.7±0.5	8.9±3.2	39.2±10.8**	51.3±7.8	77.6±5.0	99.1±0.6		
4-activation mod	1.2±3.3	7.6±3.0	26.9±8.7	37.1±8.4	54.7±11.16	4.2±11.6	80.9±7.6	99.8±0.2

Present study compared M- and F- groups in also terms of occurrence frequency of muscle activations. For all activation modalities of RF and MH, no significant differences in occurrence frequencies were detected between two groups. For VL, F-group showed a higher occurrence frequency for 3- activation modality (37.0 ± 1.8% vs. 34.5 ± 3.7%, p = 0.039) and 4-activation modality (16.2 ± 2.2% vs. 12.6 ± 3.1%, p = 0.0045), and a lower occurrence frequency in 2-activation modality (43.1 ± 4.2 vs. 53.4 ± 6.2, p = 0.0082), compared to M-group. Results on concomitant recruitment of thigh muscles showed that the same co-activations were found in both groups: during the early stance (ES), push-off (PO) and swing phase (SW) for RF/VL, RF/MH, and VL/MH. To clarify the meaning of muscles co-contraction, examples of surface EMG signals of a single subject from QF/MH co-contraction were reported in Fig. 8.5, for ES phase (Fig. 8.5, A), PO phase (Fig. 8.5, B) and for SW phase (Fig. 8.5, C); co-activations have been highlighted using a box.

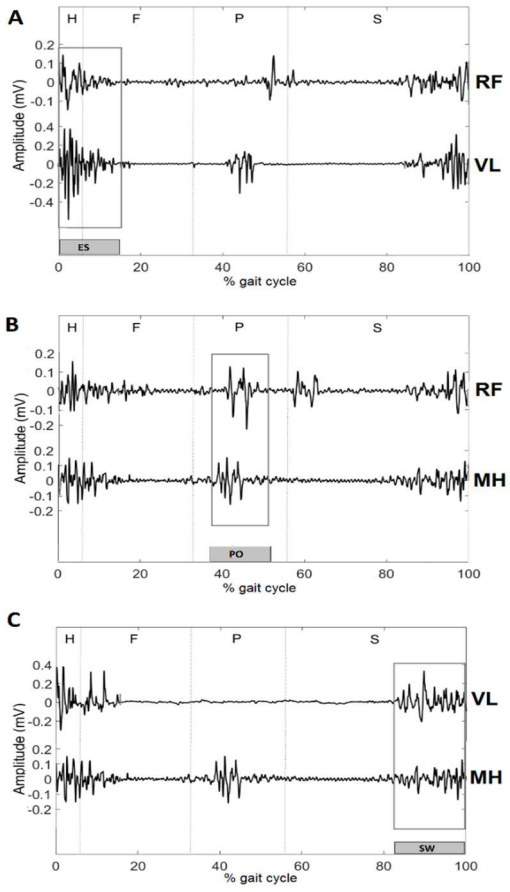

Fig. 8.5. Examples in a representative subject of ES co-activation between RF and VL (panel A), PO co-activation between RF and MH (panel B), and SW co-activation between VL and MH (panel C). Superimpositions between sEMG signals are highlighted by a box. H, F, P and S phases are delimited by vertical dashed lines. ES, PO, and PS phases are highlighted in dark grey in the bottom of the figure.

Small differences were found between groups in onset/offset instants of co-contraction for each couple of muscles (RF/VL, RF/MH, and VL/MH); details were reported in Table 2.

Table 2. Mean onset/offset for the three co-contraction intervals for the two populations. Values are expressed for female and male population as mean ± standard deviation (SD). **p<0.01 and *p<0.05 between correspondent value in F-group and M-group.

RF/VL co-contraction	**ES**		**PO**		**SW**	
	ON	OFF	ON	OFF	ON	OFF
M- group	0.6±0.4	18.3±5.3	47.8±4.0 **	45.2±9.6	84.7±2.2	99.4±0.4
F-group	0.5±0.2	18.1±5.7	38.4±7.7 **	42.4±6.3	83.9±2.1	99.3±0.6
VL/MH co-contraction						
	ON	OFF	ON	OFF	ON	OFF
M- group	0.5±0.3	14.0±3.2	37.1±9.7	43.8±10.6	81.1±0.1	99.3±0.6
F-group	0.9±0.2	15.3±3.4	34.9±2.7	46±2.4	82.0±0.2	99.1±0.1
RF/MH co-contraction						
	ON	OFF	ON	OFF	ON	OFF
M- group	2.7±2.0	13.8±1.1	48.4±2.8*	51.7±12.2	85.1±2.2	99.4±0.5
F-group	1.2±1.0	12.3±1.1	39.6±6.0*	43.8±8.4	83.1±3.5	99.3±0.4

However, no significant differences ($p > 0.05$) were observed in co-contraction duration. Occurrence frequency of every co-contraction was reported in Fig. 8.6 (panel A, B, and C), differentiated between males and females. The analysis of occurrence frequency showed that F-group adopted significantly higher occurrence-frequency values in: RF/VL co-activation during PO phase (25.8 ± 12.1% vs. 17.3 ± 14.2%, $p = 0.00697$, Fig. 8.6, A); and VL/MH co-activation during PO phase (21.9 ± 13.6% vs. 11.3 ± 8.6%, $p = 0.0025$, Fig. 8.6, B). No further gender differences were detected in occurrence frequency of the other co-contractions.

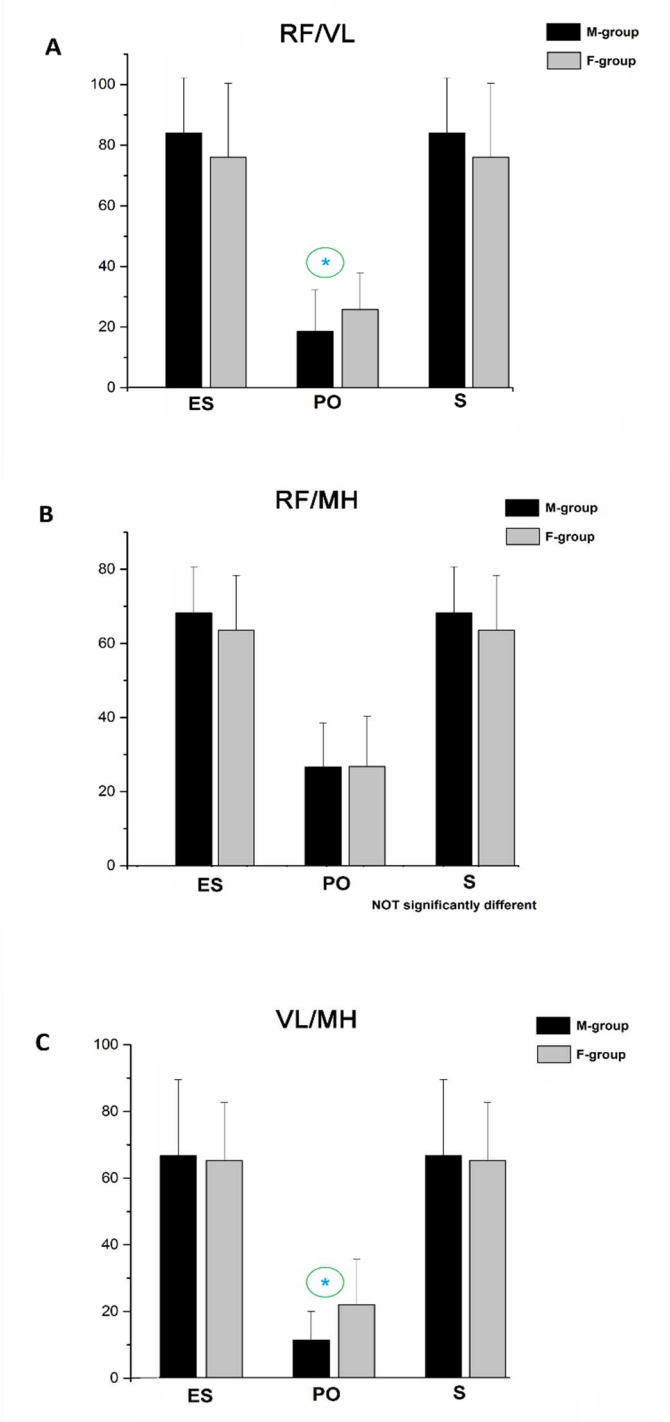

*Fig. 8.6. Occurrence frequency of RF/VL, RF/MH, VL/MH (panel A, B, C respectively) co-contractions, divided by gender. Data are expressed in percentage of total strides. Black bars represent the frequency of muscle occurrence in the M-group and grey bars represent the frequency of muscle occurrence in the F-group. * indicates that differences between F and M groups are statistically significant ($p < 0.05$).*

8.3.3 Co-activation patterns of gastrocnemius and quadriceps femoris in controlling the knee joint during walking

The quantification of co-activation patterns of gastrocnemius and quadriceps femoris in controlling the knee joint during walking provide the following results. From a total of 14,760 strides presenting the physiological phase sequence (H-F-P-S), 9723 straight-walking strides were considered, resulting in a mean of 324 ± 84 for each subject. H-phase lasted 6.0 ± 2.0%, F-phase 27.0 ± 5.6%, P-phase 24.0 ± 4.6% and S-phase 43.0 ± 3.0% of GC. Myoelectric data analysis showed a high variability in GL and VL activation patterns: each muscle exhibited five activation modalities during walking, characterized by a different OF (Table 3).

Table 3. Occurrence frequency of all the detected activation modalities for GL and VL. Values are reported in percentage of total number of strides.

	1-activation modality (%)	2-activation modality (%)	3-activation modality (%)	4-activation modality (%)	5-activation modality (%)
GL	30.6 ± 20.3	38.2 ± 10.2	23.8 ± 12.3	6.5 ± 5.7	0.9 ± 1.5
VL	1.4 ± 4.0	49.6 ± 25.2	33.7 ± 15.1	11.9 ± 10.9	2.7 ± 4.2

However, the 5-activation modality of GL and the 1- and 5activation modality of VL were observed only in 0.9%, 1.4% and 2.7% of strides, respectively. Thus, only four (GL) and three (VL) activation modalities were considered. During walking, five co-contraction intervals were detected. When GL presented a single activation, an overlapping period, from 11.7 ± 7.1% to 22.7 ± 6.1% of GC, arose during the early foot-contact phase (EFC co-contraction) when VL adopted all its considered activation modalities (Fig. 8.7, A). When VL showed the 4-activation modality, another co-activation occurred during the late foot-contact (LFC EFC co-contraction), from 27.6 ± 5.5% to 35.3 ± 4.9% of GC and in the push-off phase (PO EFC co-contraction), from 37.4 ± 10.4% to 47.2 ± 2.6% of GC. Considering the GL 2-activation modality (Fig. 8.7, B), the EFC co-activation arose from 6.6 ± 4.2% to 19.1 ± 11.6% of GC, for all the considered VL activation modalities. The LFC co-contraction happened only when VST adopted its 4-activation modality, from 27.5 ± 1.1% to 34.7 ± 0.6% of GC. An EFC co-contraction arose also when GL adopted the 3-activation modality (2.8 ± 2.4% to 18.9 ± 9.4% of GC, Fig. 8.7, C). Further, when VL presented its 3- and 4-activation modality, the

PO co-activation lasted from 35.3 ± 8.7% to 53.0 ± 7.0% of GC (Fig. 8.7, C). Eventually, a superimposition during the swing phase (SW co-activation) arose from 87.7 ± 6.3% to 94.1 ± 5.2% of GC, with all the VL activation modalities (Fig. 8.7, C). In those strides where VL showed all the considered activation modalities and GL simultaneously presented its 4activation modality, a co-contraction occurred from 1.1 ± 1.5% to 12.0 ± 10.0% of GC, during the early stance (ES co-activation) and at the end of the swing (92.6 ± 4.9 to 98.3 ± 3.4% of GC, Fig. 8.7, D). Further, the LFC co-activation occurred from 24.4 ± 3.7% to 30.8 ± 6.1% of GC. Knee angle and OCF of each co-activation, averaged over all the considered strides, are reported in Figs. 8.8 and 8.9.

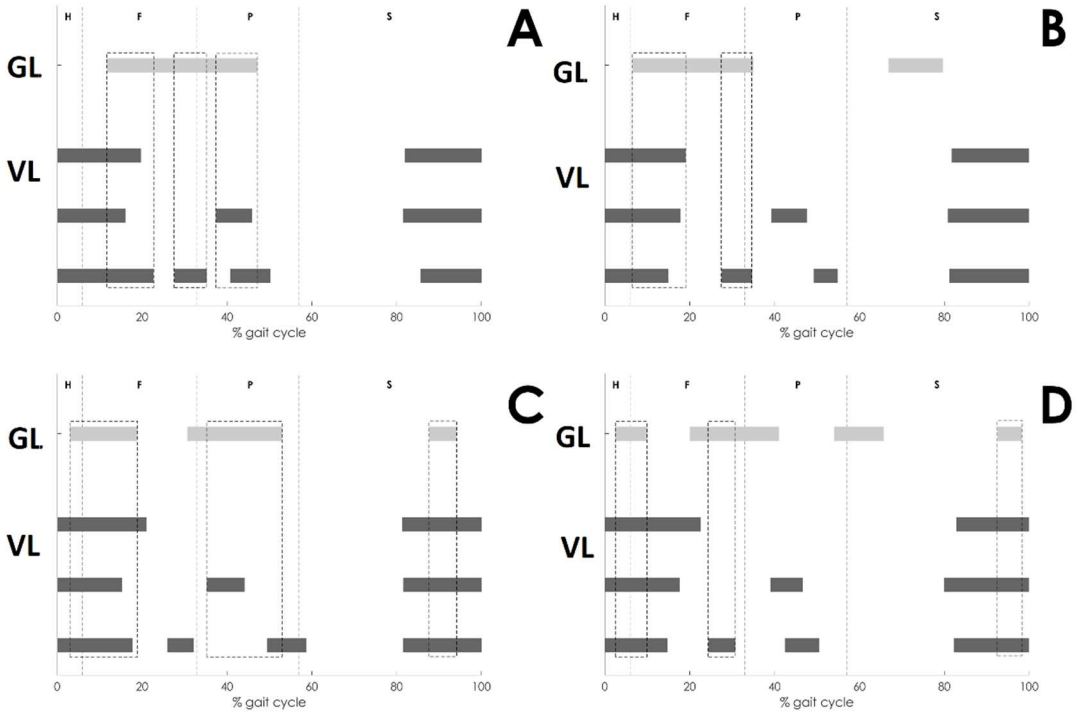

Fig. 8.7. Mean activation intervals of VL (dark bars) detected in those strides where GL (grey bars) showed 1- (A), 2- (B), 3- (C) and 4-activation modality (D). For the VL, the 2-, 3- and 4-activation modality are reported. Co-contractions intervals are highlighted by vertical dashed boxes. Gait phases (H-F-P-S) are indicated by vertical dashed lines.

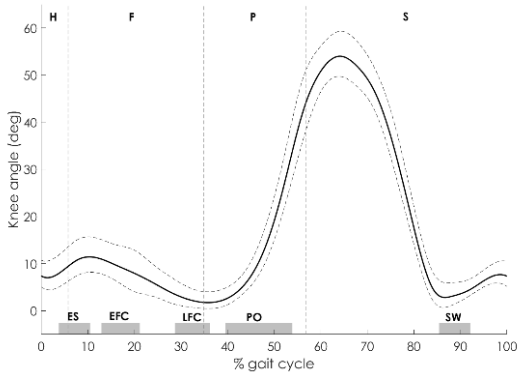

Fig. 8.8. Knee angle values versus percentage of GC, averaged over the total number of strides. Co-activation intervals are indicated by horizontal grey bars.

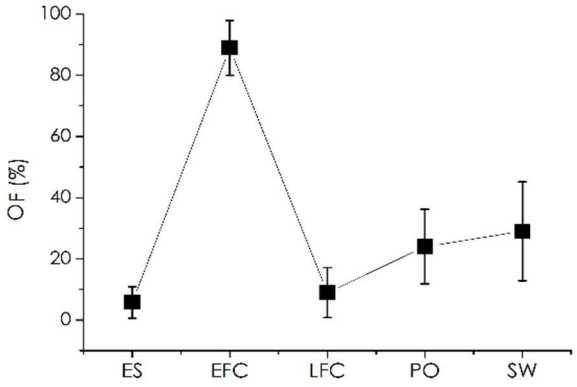

Fig. 8.9. OF of all the detected co-activation periods, reported as mean ±standard deviation. OCF of a co-activation is computed as the ratio between the number of strides where the considered co-activation has been detected and the total number of strides.

8.3.4 Assessment of thigh muscle co-contractions during child gait

The assessment of thigh muscle co-contraction during child gait provide the following results. For each subject, a mean of 165 ± 27 strides was considered, after discarding strides not following the H-F-P-S foot-switch pattern and/or being outlier cycles relative to deceleration, reversing, and acceleration of gait direction changes. Thus, a total of 16401 strides were selected. H-phase lasted 5.9 ± 1.8%, F-phase 32.5 ± 5.6%, P-phase 22.1 ± 5.4% and S-phase 39.6 ± 3.2% of gait cycle. Mean activation modalities for each muscle are reported in Fig. 8.10, considering data from right and left lower limb considered all together.

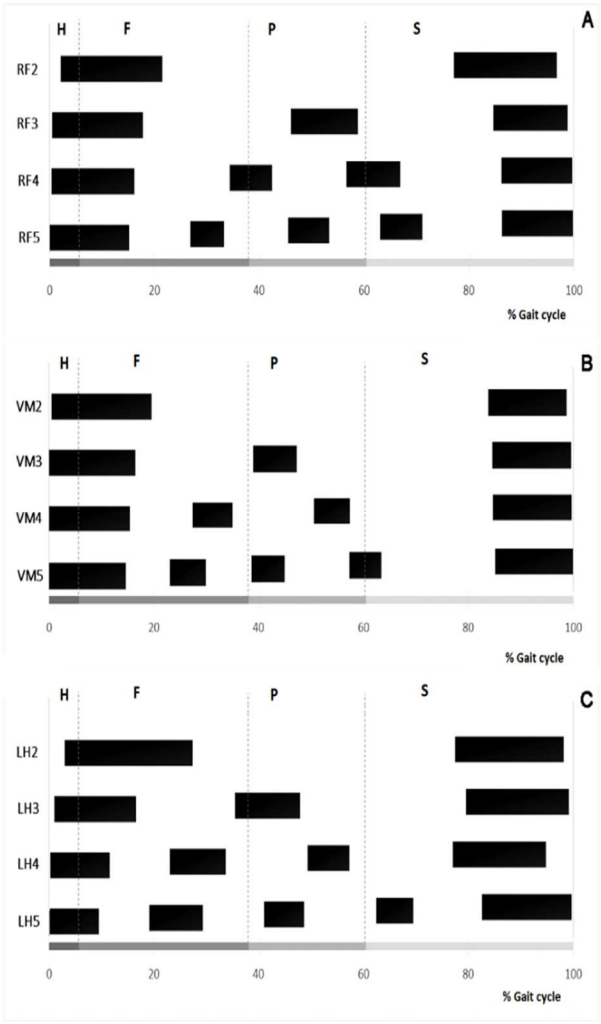

Fig. 8.10. Mean activation intervals vs. percentage of gait cycle for modalities with 2, 3, 4, and 5 activations detected during children walking for RF (panel A), VM (panel B), and LH (panel C). H, F, P and S phases are delimited by dashed vertical lines.

Three different superimposition intervals between RF and VM activities were detected during gait cycle, as follows;

- when RF adopted 2-activations modality (Fig. 8.11, A), superimpositions between RF and VM activation intervals were observed between 2.2 ± 2.2 and 18.3 ± 6.1% and between 84.2 ± 6.4 and 96.8 ± 3.2% of gait cycle. These superimpositions were detected in the three main activation modalities for VM (modalities with 2, 3 and 4 activations, respectively);

- when RF adopted 3-activations modality (Fig. 8.11, B), superimpositions between RF and VM activation intervals were observed between 0.5 ± 0.5 and 17.9 ± 5.7% and between 84.7 ± 7.3 and 98.9 ± 1.1% of gait cycle. These superimpositions were detected in the three main activation modalities for VM. A further superimposition was observed during push-off phase from 46.1 ± 5.8% to 53.2 ± 1.0% of gait cycle; - when RF adopted 4-activations modality (Fig. 8.11, C), superimpositions between RF and VM activation intervals were observed from beginning to 16.2 ± 5.4% of gait cycle and from 86.3 ± 7.1 to the end of gait cycle. These superimpositions were detected in the three main activation modalities for VM. A further superimposition was observed during push-off phase from 37.5 ± 8.78 to 42.5 ± 7.5% of gait cycle. Occurrence frequencies of RF/VM superimposition intervals are reported in Fig. 8.11, D.

Four different superimposition intervals between VM and LH activities were detected during gait cycle, as follows; when VM adopted 2-activations modality (Fig. 8.12, A), superimpositions of LH with VM activity was detected from the beginning to 19.6 ± 8.6% of gait cycle and from 83.9 ± 5.0% to the end of gait cycle. These superimpositions were detected in the three main activation modalities for LH (modalities with 2, 3 and 4 activations, respectively); when VM adopted 3-activations modality (Fig. 8.12, B), superimpositions of LH with VM activity was detected from the beginning to 16.6 ± 5.8% of gait cycle and from 85.6 ± 4.3% to the end of gait cycle). These superimpositions were detected in the three main activation modalities for LH. A further co-contraction was observed during flat-foot-contact phase from 39.0 ± 9.5 to 47.3 ± 10.0% of gait cycle; - when VM adopted 4-activations modality (Fig. 8.12, C), superimposition of LH with VM activity was detected from the beginning to 15.4 ± 5.4% of gait cycle and from 84.7 ± 5.3% to the end of gait cycle. These superimpositions were detected in the three main activation modalities for LH. Two further co-contractions were observed from 27.5 ± 7.5

to 35.8 ± 7.6% of gait cycle and from 50.6 ± 10.7 to 56.1 ± 15.2% of gait cycle. Occurrence frequencies of VM/LH superimposition intervals are reported in Fig. 8.12, D.

Four different superimposition intervals between RF and LH activities were detected during gait cycle, as follows; when RF adopted 2-activations modality (Fig. 8.13, A), superimpositions of LH with RF activity were observed between 2.2 ± 2.2 and 21.5 ± 8.7% of gait cycle and between 77.2 ± 13.9 and 96.8 ± 3.2 of gait cycle. These superimpositions were detected in the three main activation modalities for LH (modalities with 2, 3 and 4 activations, respectively); when RF adopted 3-activations modality (Fig. 8.13, B), superimpositions of LH with RF activity were observed between 0.5 ± 0.5 and 17.9 ± 5.7%of gait cycle and between 84.7 ± 7.3 and 98.9 ± 1.1 of gait cycle. These superimpositions were detected in the three main activation modalities for LH. Two further superimpositions were observed from 46.1 ± 5.0% to 49.8 ± 9.5% of gait cycle and from 53.9 ± 4.1 to 58.8 ± 7.1% of gait cycle. - when RF adopted 4-activations modality (Fig. 8.13, C), superimpositions of LH with RF activity were observed from beginning to 16.2 ± 5.4% of gait cycle and from 86.3 ± 7.1% to the end of gait cycle. These superimpositions were detected in the three main activation modalities for LH. Two further superimpositions were observed from 34.4 ± 7.0 to 42.5 ± 7.5% of gait cycle and from 56.7 ± 6.7 to 62.1 ± 4.3% of gait cycle.

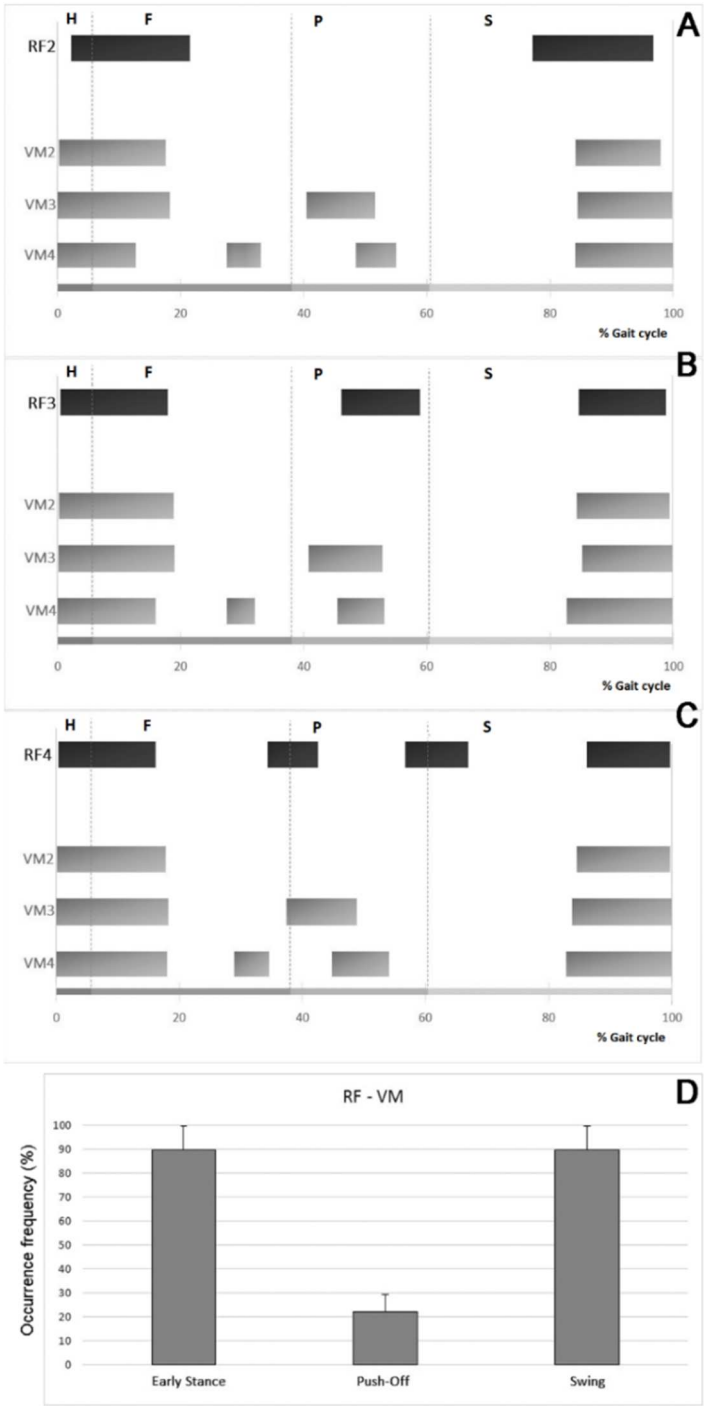

Fig. 8.11. Mean values of VM activation intervals (gray bars) vs. percentage of gait cycle, detected in the strides where RF (black bars) shows 2-activation (panel A), 3-activation (panel B), and 4-activation (panel C) modality, respectively. VM activation intervals are reported separately for the modalities with 2, 3 and 4 activations. Mean (+SD) percentage occurrence frequency of each of the three different RF/VM co-contractions are reported in panel D. H, F, P and S phases are delimited by dashed gray vertical lines.

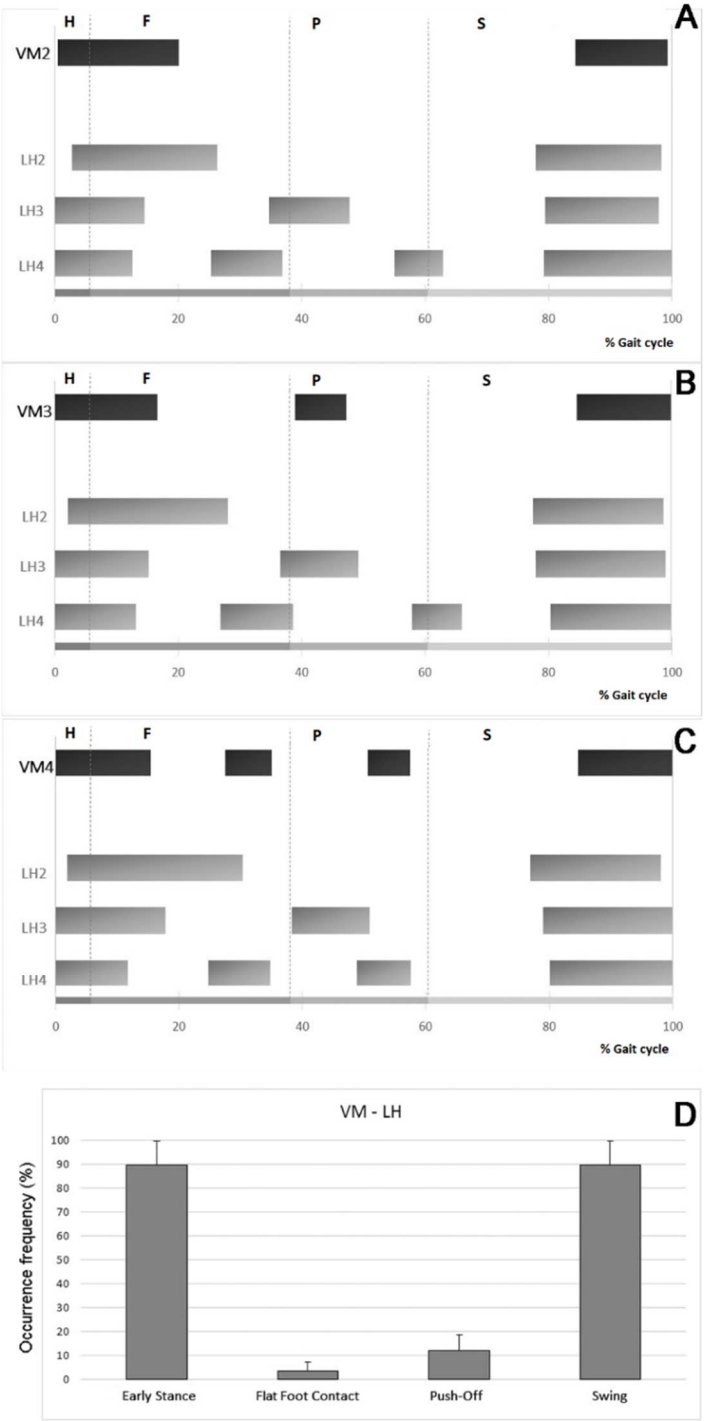

Fig. 8.12. Mean values of LH activation intervals (gray bars) vs. percentage of gait cycle, detected in the strides where VM (black bars) shows 2-activation (panel A), 3-activation (panel B), and 4-activation (panel C) modality, respectively. LH activation intervals are reported separately for the modalities with 2, 3 and 4 activations. Mean (+SD) percentage occurrence frequency of each of the three different VM/LH co-contractions are reported in panel D. H, F, P and S phases are delimited by dashed gray vertical lines.

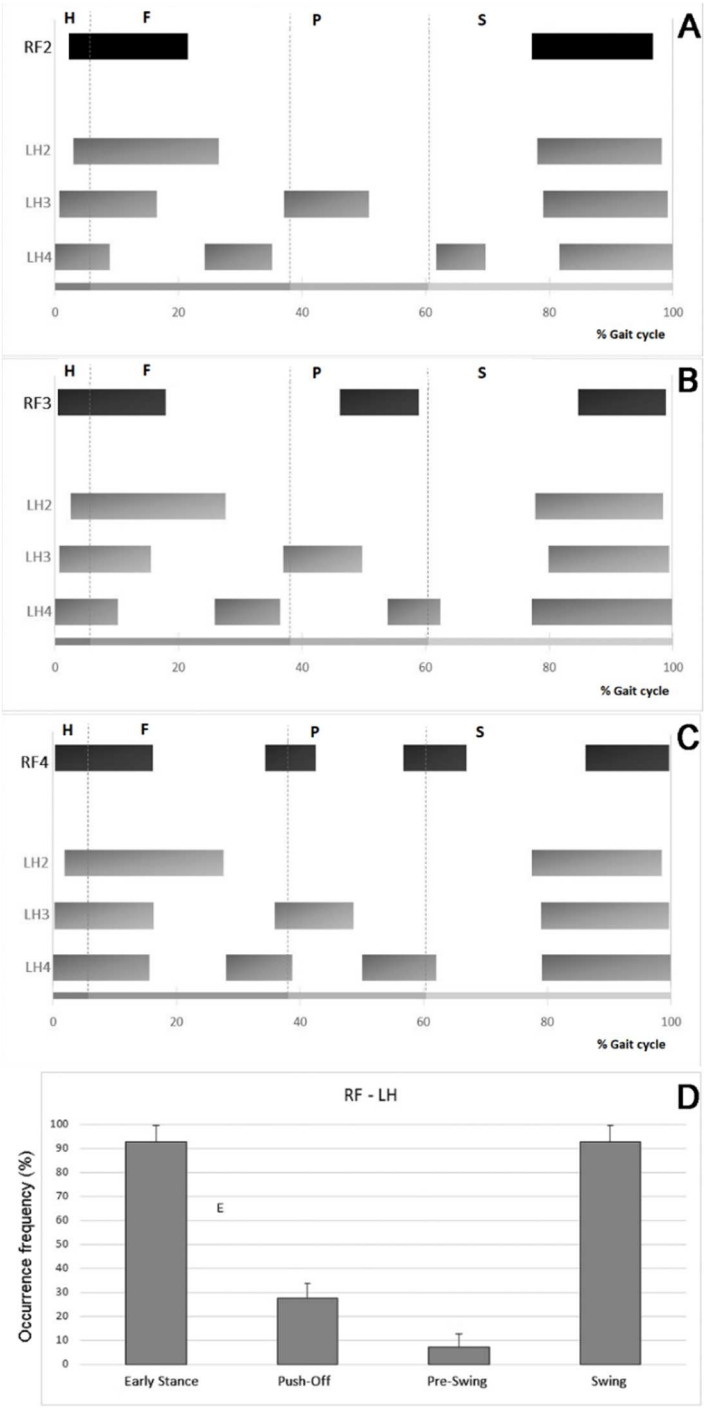

Fig. 8.13. Mean values of LH activation intervals (gray bars) vs. percentage of gait cycle, detected in the strides where RF (black bars) shows 2-activation (panel A), 3-activation (panel B), and 4-activation (panel C) modality, respectively. LH activation intervals are reported separately for the modalities with 2, 3 and 4 activations. Mean (+SD) percentage occurrence frequency of each of the three different RF/LH co-contractions are reported in panel D. H, F, P and S phases are delimited by dashed gray vertical lines.

Occurrence frequencies of RF/LH superimposition intervals are reported in Fig. 8.13, D. Effect of age on co-contractions was also analyzed across the age range. All the children showed the same four main activation modalities for each muscle (Fig. 8.14), irrespective of age. No significant correlation was found between occurrence frequency of co-contractions and age of children ($p>0.05$, Fig. 8.14).

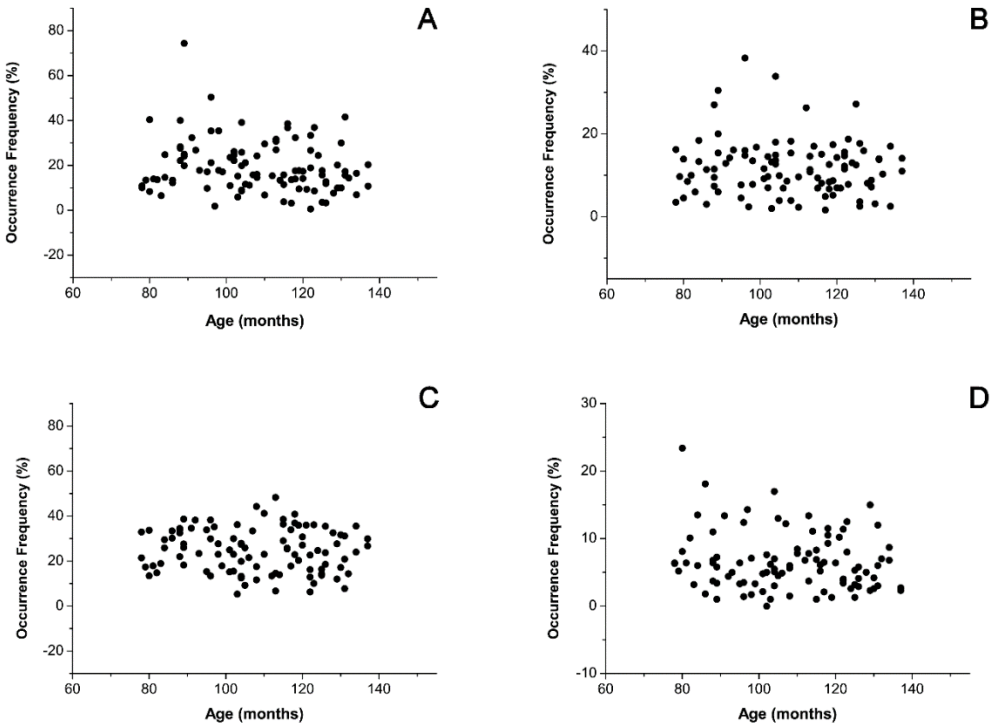

Fig. 8.14. Effect of age on co-contractions across the age range.

8.3.5 Interaction between EMG activity of intrinsic and extrinsic foot muscles during child walking

For the assessment of interaction between EMG activity of intrinsic and extrinsic foot muscles during child walking, it is necessary to provide a normal reference data for the EDB activation. For each subject, a mean (±standard error, SE) of 382 ± 25 strides were considered. From the total of 8423 strides considered, 927 strides (11% of total strides) were removed from the analysis because they did not follow the H-F-P-S footswitch pattern and/or were outlier cycles relative to deceleration, reversing, and acceleration. The mean results are reported with data from the right and left lower limbs considered together. The SGA of the myoelectric signals indicated that muscles show different numbers of activation intervals in different strides of the same walking session. As an example, raw sEMG signals from the EDB muscle of a subject are depicted in Fig. 8.15.

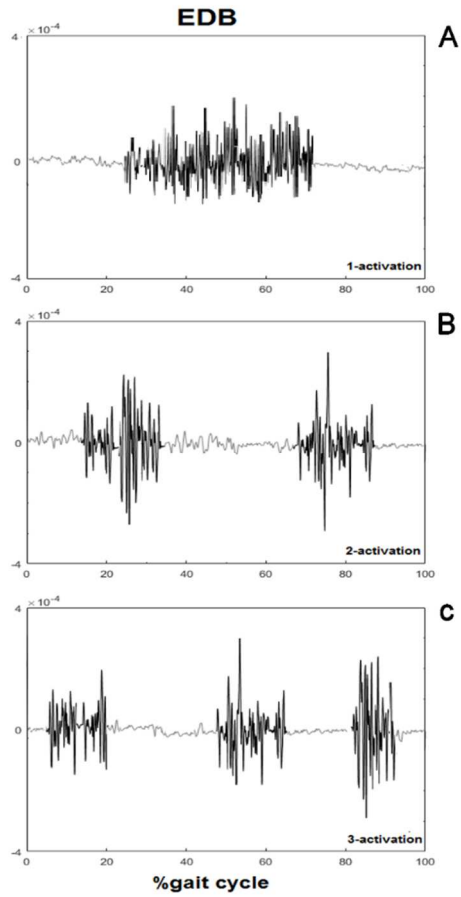

Fig. 8.15. Example of raw sEMG signals of the EDB muscle showing one activation (panel (A)), two activations (panel (B)) and three activations (panel (C)), respectively.

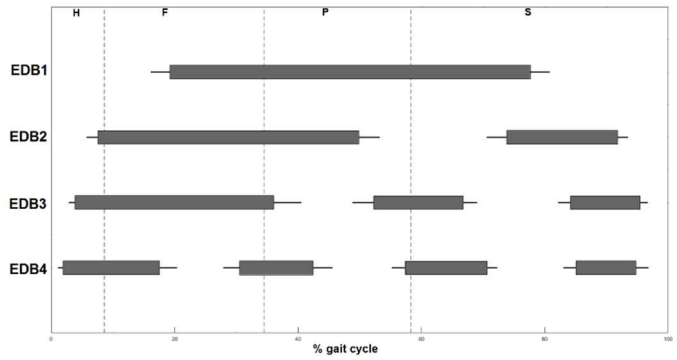

Fig. 8.16. EDB: mean (+SE) activation intervals versus percentage of gait cycle for the modalities with one, two, three and four activations, respectively, detected during children walking. Each activation modality has been detected in each subject. H, F, P, S phases are denoted by dashed light-grey vertical lines.

Fig. 8.16 reports mean (+SE) EDB activation intervals over all the considered strides versus percentage of gait cycle for the modalities with one, two, three and four activations, respectively. The most recurrent modality of activation for EDB consists of two activations (2-activation modality, EDB2), observed in 42.9 ± 2.9% of total strides (mean±SE); the first occurs in early mid-stance (from 7.6 ± 1.9% to 49.8 ± 3.2% of the gait cycle), and the second activation in the swing phase, from 73.8 ± 3.0% to 92.0 ± 1.7% of the gait cycle. Instead, in 30.8 ± 4.5% of total strides 1-activation modality was detected (EDB1); this activation modality was observed from 18.2 ± 3.2% to 79.0 ± 3.4% of the gait cycle. In a further 20.1 ± 3.1% of total strides, three activations were detected for EDB (EDB3): from 3.9 ± 1.1% to 36.3 ± 4.3% of the gait cycle, from 51.9 ± 3.3% to 67.1 ± 2.1% of the gait cycle and during the swing phase from 84.1 ± 2.0% to 95.7 ± 1.2 % of the gait cycle. The remaining 5.5 ± 1.2% of total strides was characterized by two activations during the stance and two activations during the swing (4-activation modality). The most recurrent modality of activation for the GL (Fig. 8.17, A) consists of two activations (2-activation modality), observed in 33.1 ± 1.5% of total strides; the first occurs in the transition between flat foot contact and push-off phases (6.7–36.5% of the gait cycle), and the second during the mid-swing. The second most recurrent modality of activation is characterized by three activations for the GL: in the flat foot contact phase, push-off phase and terminal swing (3-activation modality). This 3-activation modality was observed in 31.2 ± 2.2% of total strides. In a further 23.9 ± 3.3% of total strides, a single activation was observed for the GL; this 1-activation modality is

similar to the 2-activation modality but with no activation during the swing. The remaining 10.6 ± 1.7% of total strides was characterized by four activations, two activations during the stance and two activations during the swing (4-activation modality). For the TA (Fig. 8.17, B), the most recurrent modality of activation during the gait cycle consists of three activations (3-activation modality), observed in 49.6 ± 1.5% of total strides: the first occurs at the beginning of the gait cycle, the second around stance-to swing-transition and the third in the terminal swing. In 22.8 ± 2.2% of total strides, only two activations were observed: from the beginning up to 15.5 ± 1.8% of the gait cycle, and during the whole swing (2-activation modality). In 21.9 ± 1.4% of total strides a 4-activation modality was observed, similar to the 3-activation modality but with a further activation in the transition between flat foot contact and push-off phases. The remaining 4.3 ± 0.5% of total strides was characterized by five activations, three during the stance and two during the swing (5-activation modality). The 5-activation modality for the EDB and GL and the 1-activation modality for the TA were observed only in 1.5% of the total stride and showed a large variability; thus, they are not considered in the present analysis.

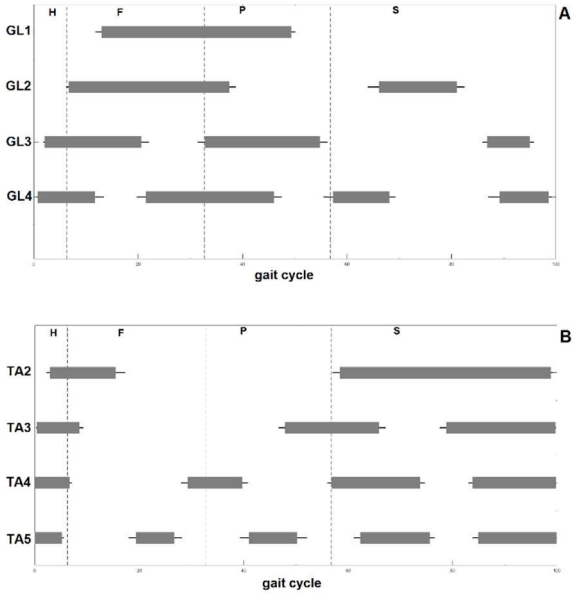

Fig. 8.17 Panel (A): GL. Mean (+SE) activation intervals versus percentage of the gait cycle for the modalities with one, two, three and four activations, respectively, detected during children walking. Each activation modality has been detected in each subject. Panel (B): TA. Mean (+SE) activation intervals versus percentage of the gait cycle for the modalities with two, three, four and five activations, respectively, detected during children walking. Each activation modality has been detected in each subject. H, F, P, S phases are delimited by dashed light-grey vertical lines.

The interaction between EMG activity of intrinsic and extrinsic foot muscles during child walking provide the following results. 265±30 (mean±SD) strides were analyzed for each child, nearly 2500 in total. EDB activity was localized in two separate regions of gait cycle (GC): mid-stance (from 8.2±7.0 to 50.3±15.0% of GC) and swing phase, from 73.8±13.8 to 95.1±4.7%. Main GL activity occurred in the same regions: mid-stance (from 5.7±2.5 to 49.7±4.6% of GC) and swing phase, from 69.2±18.7 to 95.4±5.4%. Differently, TA activity was detected from the beginning of GC to 18.2±16.9% of GC and from 56.4±9.2% to the end of GC. Summarizing pattern for sEMG activity of each muscle was reported in Fig. 8.18.

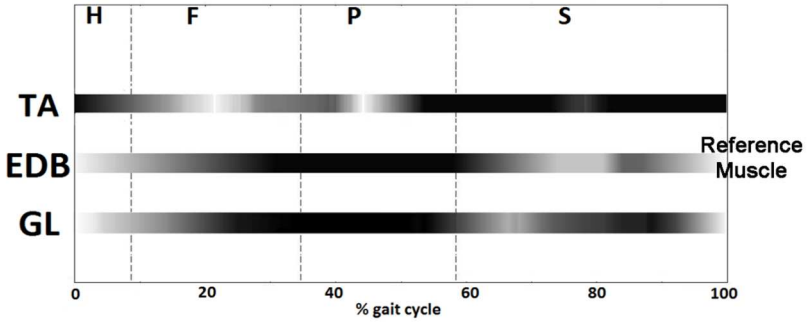

Fig. 8.18. Activation intervals in the whole population summarized in terms of number of children where muscular activity was acknowledged. Horizontal bars are grey-level coded, according to the number of children where a certain condition is observed; black: condition observed for all subjects in the considered activation modalities, white: condition never met. Dashed lines delimited H, F, P, and S phases.

8.3.6 Evaluation of gender effect on muscular recruitment during children walking

The quantification of gender-related differences in myoelectric activity of gastrocnemius lateralis and tibialis anterior during walking at self-selected speed and cadence in school-age children is performed in terms of muscle activation patterns and occurrence frequencies of sEMG signal and in terms of direct gender-related comparison with young to get possible novel insight in maturation of gait. In C-group, no significant differences were detected between females and males in age (107.6 ± 15.5 vs. 108.8 ± 17.3 months, p = 0.72), height (133 ± 10 vs. 134 ± 9 cm, p = 0.57), and mass (30.7 ± 7.2 vs. 30.6 ± 6.2 kg, p = 0.91). In YA-group, height (164 ± 3 vs. 180 ± 6 cm, p = 0.014) and mass (51.8 ± 3.2 vs. 72.5 ± 8.5 kg, $p = 3.2*10^{-6}$) were significantly lower in females, compared with males. No significant differences were observed in age (23.5 ± 1.3 vs. 24.2 ± 2.3 years, p = 0.21). For each subject, a mean of 301 ± 110 strides was considered for the study, after discarding the strides not following the H-F-P-S foot-switch pattern and/or being outlier cycles relative to deceleration, reversing, and acceleration of gait direction changes. For children, H-phase lasted 5.9 ± 1.8%, F-phase 32.5 ± 5.6%, P-phase 22.1 ± 5.4% and S-phase 39.6 ± 3.2% of the gait cycle. For young adults, H-phase lasted 6.3 ± 3.0%, F-phase 26.4 ± 6.4%, P-phase 24.1 ± 4.6% and S-phase 43.1 ± 3.0% of the gait cycle. In C-group no significant differences between females and males were detected in cadence (60.1 ± 6.0 vs. 60.6 ± 5.5 cycle/min, p = 0.53) and in walking speed (0.99 ± 0.13 vs. 1.00 ± 0.11 m/s, p = 0.81). In YA-group, cadence was significantly higher in females, compared with males (57.8 ± 2.5 vs. 55.3 ± 3.7 cycle/min, p = 0.002); no significant differences in walking speed were detected (1.19 ± 0.19 vs. 1.20 ± 0.09 m/s, p = 0.42). The SGA of myoelectric signal indicated that muscles show a different number of activation intervals in different strides of the same trial. Details of mean activation intervals in C-group and YA-group are reported in Table 1 for GL and in Table 2 for TA. In C-group, no significant differences were observed in onset/offset instants of activation between males and females, for all the detected modalities of GL and TA activation (Tables 4 and 5).

Table 4. Activation Intervals of gastrocnemius lateralis in its main modalities of activation, expressed as the timing, in the percentage of gait cycle, of signal onset and offset. Values are expressed in C-group and in YA-group, for female and male population, as mean ± standard deviation (SD). No statistically significant differences were detected between gender groups.

Gastrocnemius lateralis	First activation (% gait cycle)		Second activation (% gait cycle)		Third activation (% gait cycle)	
	ON	OFF	ON	OFF	ON	OFF
C-group – Females (n=49)						
1-activation mod	13.9±7.9	49.7±7.2				
2-activation mod	7.2±4.3	37.4±7.6	67.5±12.1	80.6±9.8		
3-activation mod	2.7±3.1	20.8±9.4	32.9±9.2	55.2±6.4	86.8±8	94.5±5.5
C-group – Males (n=51)						
1-activation mod	14.3±8.2	49.7±6.3				
2-activation mod	7.3±3.9	36.6±7.7	66.6±12.2	79.3±10.2		
3-activation mod	2.8±3.2	19.9±10.7	32.5±10.1	55.3±6.8	87.7±8.5	94.7±5.3
YA-group – Females (n=17)						
1-activation mod	13.1±7.3	47.2±2.6				
2-activation mod	7.1±4.9	36.0±6.7	68.1±10.6	80.6±8.9		
3-activation mod	2.5±2.5	17.9±7.1	29.6±7.9	52.3±5.6	87.7±5.4	94.7±4.6
YA-group – Males (n=16)						
1-activation mod	10.5±6.8	46.9±2.5				
2-activation mod	6.9±4.6	35.4±5.9	67.1±11.2	79.4±8.3		
3-activation mod	3.9±3.3	21.1±10.8	33.8±13.7	55.2±7.9	87.5±6.9	93.4±5.6

Table 5. Activation intervals of tibialis anterior in its main modalities of activation, expressed as the timing, in the percentage of gait cycle, of signal onset and offset. Values are expressed in C-group and in YA-group, for female and male population, as mean ± standard deviation (SD). *indicates statistically significant difference between gender groups.

Tibialis anterior	First activation (% gait cycle)		Second activation (% gait cycle)		Third activation (% gait cycle)		Fourth activation (% gait cycle)	
	ON	OFF	ON	OFF	ON	OFF	ON	OFF
C-group – Females (n=49)								
2-activation mod	2.1±1.8	15.2±10.5	61.6±10.1	98.6±1.4				
3-activation mod	0.1±0.1	9.5±4.5	49.3±7.2	65.7±8.3	79.9±7.9	99.7±0.3		
4-activation mod	0.0±0.2	7.5±3.4	28.5±7.6	37.9±8.0	57.2±5.7	73.2±5.3	83.7±5.6	99.8±0.2
C-group – Males (n=51)								
2-activation mod	2.1±2.0	14.3±11.5	59.4±8.8	99.0±1.0				
3-activation mod	0.1±0.4	9.1±4.3	48.1±7.8	64.8±9.3	78.1±8.9	99.8±0.2		
4-activation mod	0.2±0.2	7.7±13.2	30.6±8.1	40.3±8.7	57.8±6.1	73.9±7.2	83.4±5.9	99.7±0.3
YA-group – Females (n=17)								
2-activation mod	2.5±1.3	19.5±16.7*	62.2±12.7*	98.3±1.8				
3-activation mod	1.3±1.1	7.8±3.5	48.6±8.2*	65.1±9.0*	80.1±7.8*	99.8±0.2		
4-activation mod	0.3±0.2	5.9±2.2	30.4±9.0*	39.7±9.8*	57.7±6.9*	72.5±7.3*	83.6±6.9*	99.9±0.1
YA-group – Males (n=16)								
2-activation mod	0.8±0.7	11.5±12.5	55.5±5.2*	99.9±0.1				
3-activation mod	0.1±0.05	5.7±3.0	37.3±9.11*	52.2±13.3*	66.4±10.7*	99.9±0.1		
4-activation mod	0.1±0.1	4.7±1.8	24.5±7.7*	32.3±9.5*	47.4±9.9*	63.7±12.8*	73.2±10.2*	99.9±0.1

Differences between males and females in YA-group were reported in Table 5; no significant differences were detected in onset/offset instants of activation between males and females, for all detected modalities of GL (Table 4). In both C-group (Fig. 8.19) and YA-group (Fig. 8.20), females and males were compared also in terms of occurrence frequency, quantified by the number of strides (%), over total subjects, where muscle is recruited with the specific activation modality. No significant differences were detected in C-group between males and females for both GL and TA mean occurrence frequencies (Fig. 8.19). In YA-group, males presented for GL a higher ($p < 0.001$) occurrence frequency in 1-activation modality and a lower occurrence frequency in 3-activation modality ($p < 0.001$), 4-activation modality ($p < 0.001$) and 5-activation modality ($p < 0.005$) (Fig. 8.20, A). Similarly, males showed for TA a higher ($p < 0.001$) occurrence frequency in 2-activation modality and a lower

occurrence frequency in 4-activation modality ($p < 0.01$) and 5-activation modality ($p < 0.05$) (Fig. 8.20, B).

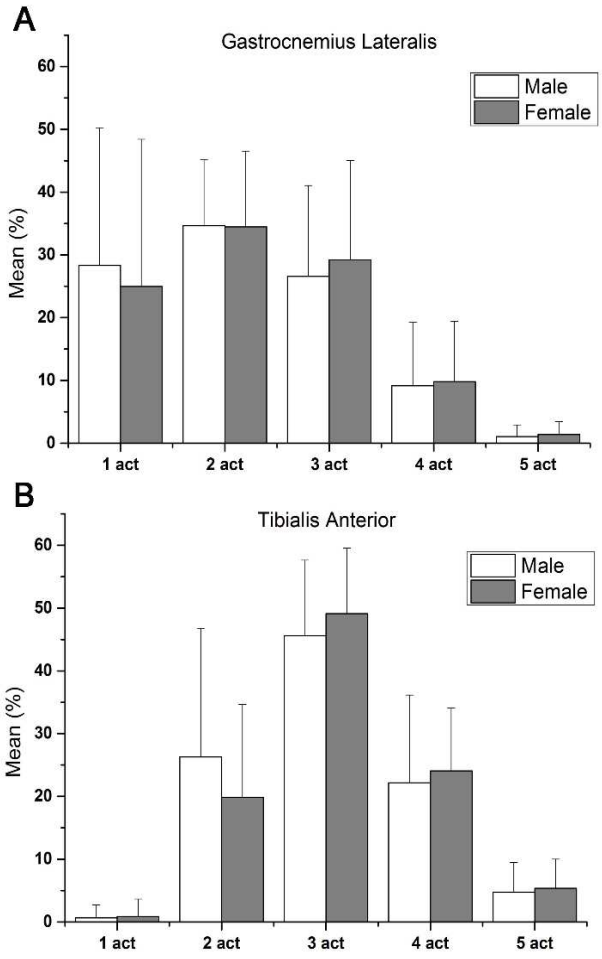

Fig. 8.19. Mean (+SD) percentage frequency of each of the five different activation modalities of GL (panel A) and TA (panel B), detected during walking in C-group for females (gray-colored bars) and males (white-colored bars). No statistically significant differences were detected between gender groups.

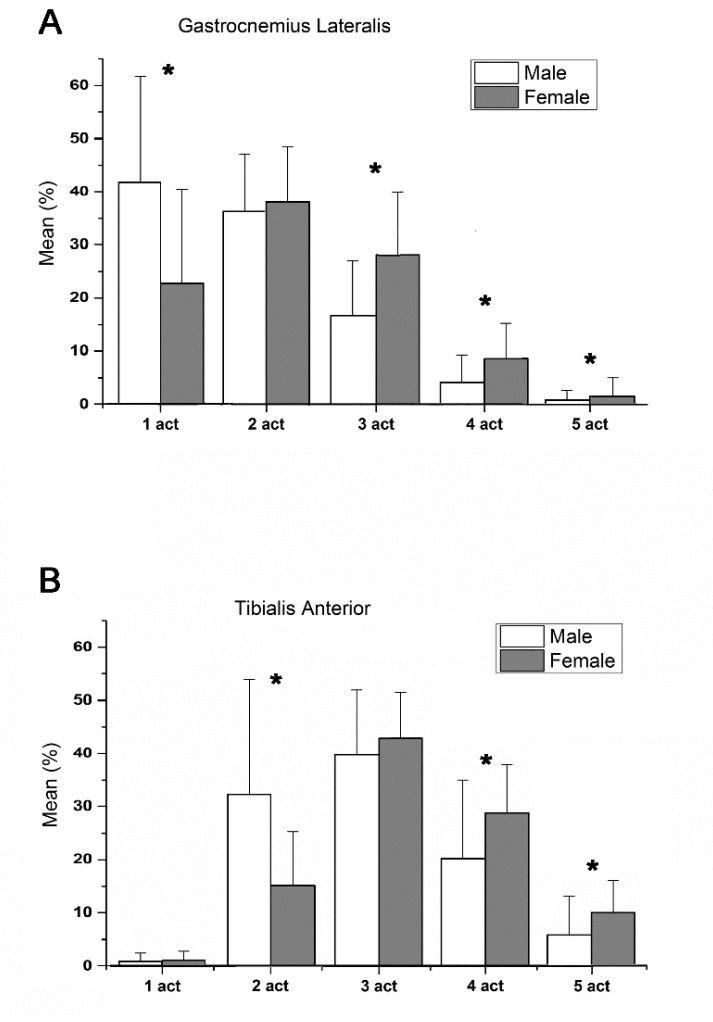

*Fig. 8.20. Mean (+SD) percentage frequency of each of the five different activation modalities of GL (panel A) and TA (panel B), detected during walking in YA-group for females (gray-colored bars) and males (white-colored bars). *Indicates statistically significant difference between gender groups.*

To analyze the effect of age on gender-related differences in children, two sub-groups were extracted from C-group: YC-group (youngest children group, 16 females and 12 males, 6–8 years, 86.2 ± 5.1 months; height 124 ± 7 cm; mass 25.7 ± 5.8 kg) and OC-group (oldest children group, 15 females and 15 males, 10–12 years, 127 ± 5 months; height 141 ± 6 cm; mass 34.5 ± 5.5 kg). In both YC-group and OC-group, no significant differences were observed in onset/offset instants of activation between males and females, for all the detected modalities of GL and TA. No significant differences were

detected in YC-group between males and females for both GL and TA mean occurrence frequencies (Fig. 8.21 A and B). In OC-group, males presented for GL a higher ($p < 0.05$) occurrence frequency in 1-activation modality and a lower occurrence frequency in 3-activation modality ($p < 0.05$), 4-activation modality ($p < 0.05$) (Fig. 8.21, C); no significant gender-related differences were detected for TA mean occurrence frequencies (Fig. 8.21, D).

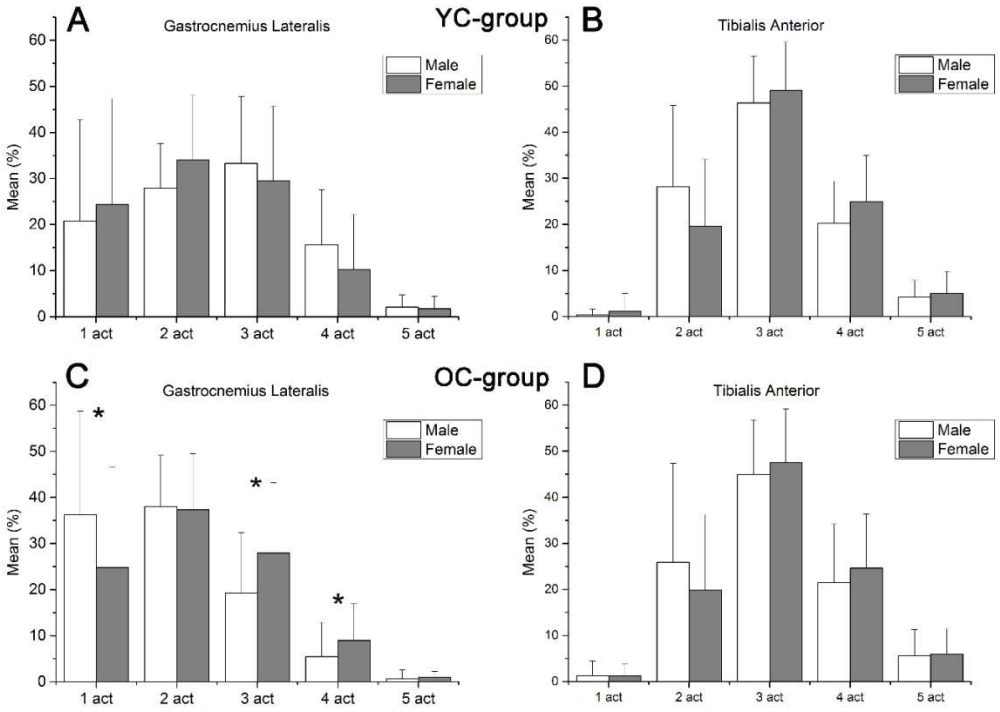

*Fig. 8.21. Mean (+SD) percentage frequency of each of the five different activation modalities of GL and TA, detected during walking in YC-group (panels A and B) and in OC-group (panels C and D) for females (gray-colored bars) and males (white-colored bars). *Indicates statistically significant difference between gender groups.*

8.4 Discussion

An extensive literature has been focused on the analysis of sEMG signal in order to assess muscle activation and co-activation, also stratified for gender [1][2][28]. However, most of the reported studies are limited by the small number of gait cycles considered for each subject; this may encumber the quantification of the natural variability associated with muscle activity during free walking. To overcome this limitation, in the present work a high number of consecutive strides per subject was considered. For this purpose, SGA was used, in order to manage a large amount of data from a single subject, to extract a large amount of information on the variability of sEMG signal and to summarize mean results in a user-friendly way. SGA allow to consider the information on stride-to-stride variability, by means of the identification of the different activation modalities [25]. Muscles showed different modalities in number of activations and timing of signal onset/offset, in different strides of the same walking, for both adult and children population. Thus, following the literature [5], the activation modalities are presented in function of the typical GC, which starts with initial contact and ends with terminal swing. Numerous strides allow to describe the large variability of muscle recruitment. This suggests that it is worth considering not only the activation patterns of each muscle, but also how frequently they are observed, i.e. their occurrence frequency.

Co-contractions during adult walking

The study of the whole variability of thigh muscles allowed to provide a complete picture of co-contractions among VL, RF and MH during young adult walking. RF-activity from terminal swing to the following loading response was detected in the nearly totally of strides. Main VL-activity occurred at the same relative percentage in GC as RF (Fig. 8.2), determining a superimposition in 100% of strides. The superimposition during early stance could be intended as a synergic action of muscles for controlling weight bearing; this matches with [9]. Similarly, the synergic action of VL and RF in terminal swing is suggested to be present to assist knee extension and develop muscle tension for weight acceptance during loading response. However, RF-signal, detected from terminal swing to the following loading response, could also be due to cross-talk from vastii [30][31]. High levels of muscle

excitation intensity (Fig. 8.2) in these gait phases could support both hypotheses. MH was also recruited in the same percentage of GC where the above-cited activity of QF muscles was detected. This determined a superimposition of MH with both VL and RF activity in more than 90% of considered strides (Figs. 8.3–8.4). While it is reasonable indicating that mono-articular vastii muscles influence actions about the knee, it is real hard isolating the influence of a bi-articular muscle (MH) to a single joint. Thus, interpretation of superimposition in early stance and swing needs to be deepened. However, superimposition in terminal swing could be reasonably intended as an action of muscles across the knee. It likely occurs in this gait phase to assist knee extension, developing muscle tension for weight acceptance during loading response [2][5]. This is the co-contraction with the highest level of muscle excitation intensity (Figs. 8.3–8.4). Moreover, it is involved in assisting ACL to prevent excessive anterior tibial displacement and in protecting ACL itself from injury [2]. RF and VL overlapped their activity also in push-off phase. RF and VL are likely working in synergy for modulating rapid knee flexion, although in only 8.14±15.7% of considered strides and with low levels of muscle excitation intensity. At the same time, VL is able to contribute to patella stabilization before entering pre-swing phase and RF participates to hip flexion. During push-off phase, uncommon and variable activities of VL and MH were detected (Fig. 8.3). VL is likely recruited to modulate rapid knee flexion and to stabilize the patella before entering pre- swing phase [32]. MH acts as hip extensor to propel body forward [5]. These activities implied the appearance of a superimposition between VL and MH (Fig. 8.3, B). It was detected in a low percentage of strides (21.9 ± 13.6%) and with low levels of muscle excitation intensity (Fig. 8.3, B) and showed a large variability both intra- and inter-subjects, covering the entire push-off phase (around 30–50% of GC). This superimposition should not be considered as a real co-contraction, because VL and MH are working mainly on different joints. Differently, the superimposition between sEMG signals from RF and MH (Fig. 8.4, B), detected in 32.7±15.1% of strides, could be intended as an actual co-contraction for the control of rapid knee extension and it could play a role also in stabilization of pelvis during body progression. The levels of excitation intensity appeared to be higher than those reported for VL/MH co-activation in the same phase (Fig. 8.4, B vs. Fig. 8.3, B). Thus, three different co-contractions were identified:

in early stance (in ≈ 90% of strides), in push-off (in 25–30% of strides) and during swing (in ≈ 90% of strides).

The quantification of thigh-muscle co-contraction allowed to test also the effect of gender on this physiological phenomenon. Results showed no significant gender-related differences in occurrence frequencies of MH and RF muscular activity. On the contrary, in F-group, compared with M-group, VL showed a significantly higher occurrence frequency in modalities with a high number of activations, and a significantly lower occurrence frequency in modalities with a low number of activations. Analyzing the mean onset/offset instants (Table 1), no differences were observed between F and M groups in VL/MH co-activation. Small differences were detected for the other two co-contractions. Occurrence-frequency findings indicated an overall higher occurrence of thigh-muscle co-activations in females compared to males. In fact, occurrence frequency of RF/VL co-activation in PO phase was significantly higher ($p = 6.9 \times 10^{-3}$, Fig. 8.6, A) in F-group (25.8 ± 12.1% of strides) than in M-group (17.3 ± 14.2%). An increase of occurrence frequency in females was observed also for VL/MH co-activation during PO phase (21.9 ± 13.6% vs. 11.3 ± 8.6%, $p = 2.5 \times 10^{-3}$, Fig. 8.6, C). No further gender differences were detected in occurrence frequency for the other co-activations. These differences entailed a 74.1% increase in females ($p < 0.05$) of strides where thigh-muscle co-activity were noticed during PO phase. This increase was determined only by co-activations which involved VL muscle (VL/MH and RF/VL). Thus, the increased occurrence of VL activity and consequently of RF/VL and VL/MH co-activations in PO phase seems to suggest a more complex muscular recruitment in females, in line with [5][3]. In particular, this increased muscular recruitment in females occurred during PO phase of gait, when the control of balance is more awkward because of the final phase of single support [33]. It seems to reflect a female needing for a higher level of knee-joint stabilization, as reported for ankle joint [3]. A further hypothesis to be verified by specific studies is that increased muscular recruitment in females could be finalized to assist ACL in preventing excessive anterior tibial displacement and to protect the ACL itself from injury during walking.

For a better understanding of ACL mechanism, fundamental is the analysis of GL/VL co-contractions. Results of the present study showed as five co-contraction periods between GL and

VL were recognized in a single GC (Figs. 8.7 and 8.8). The ES co-contraction lasted, for about 9% of GC, from heel strike to the beginning of foot-contact phase (Fig.8.7, D), enhancing knee joint stiffness in order to gain stability during the ground contact. During this period, knee angle showed an almost constant value (from 9.4 ± 4.3° to 11.7 ± 5.3°), highlighting the absence of a full knee extension, joined to the need for a damping response after the heel strike. Further, ES co-activation showed the lowest OF (5.7 ± 5.1%). The second co-contraction arose during the foot-contact phase (Figs. 8.7 and 8.8). In this period, GL exerts its activity of ankle-extensor muscle, restraining the tibia rotation over the talus through the dorsiflexion control and decelerating the lower limb forward movement [5]. VL activity showed a single (2-and 3-activation modality) or a double (4-activation modality) burst (Fig. 8.7). In the former case, VL activity control the knee joint after the weight acceptance, when the contralateral limb swing begins. This muscular activity could be related to the occasional need for an additional knee extension effort, considering that in this phase the knee extension occurs without a direct participation of QF [5]. Splitting foot-contact period in two different sub-phases is justified by considering that different knee flexion values were associated to EFC and LFC co-contraction and muscular co-activations influence knee dynamics, depending strongly on joint angle value [10]. In early foot-contact, knee joint angle did not fall under 8.0 ± 4.9° (not complete extension, Fig. 8.8). Conversely, LFC co-activation occurred around 50% of stance phase, where knee joint angle reached its lowest value (3.7 ± 3.4°), close to the full extension. Despite its relatively low recurrence (8.9 ± 8.2%), LFC co-activation deserves particular attention: with an almost complete extended knee, a QF activity leads to an increase in anterior tibia translation, which could affect knee joint ligaments when a simultaneous GL activity arises [11]. During F-phase the landing leg holds the entire body weight, adding a significant mechanical stress for the knee. The latter is highlighted by the relative ACL strain, which reaches its highest value (about 13% of the ACL length measured while standing with the leg in full extension), for both anteromedial and posterolateral bundle, during the mid-stance. GL activity during the push-off phase is commonly related to the plantar-flexion needed for the heel raising [34]. VL acts for the patella stabilization and the knee flexion modulation before entering the swing phase [6]. During the PO co-activation, the knee joint progressively increases its flexion, reaching a maximum of 28.1 ± 6.9° at the end of co-

contraction (Fig. 8.8). The knee flexion results in a posterior tibia translation, which reduces the mechanical stress on the joint [11]. Therefore, despite the high recurrence of PO co-contraction (23.9 ± 12.2%), simultaneous activity of GL and QF muscles could have limited effects on the knee joint during the period preceding the swing phase. The last overlapping period was identified in late swing, when GL adopted its 3- and 4-activation modality (Fig. 8.7, C and D). VL exerts its well-known function of knee extensor, preparing the lower limb for ground contact [5]. SW co-contraction occurs with a high OF (29.0 ± 16.1%) and is associated with a low knee extension (around 6°). It has been indicated that co-contractions between gastrocnemius and QF muscles lead to higher ACL strain values with respect to those observed for a single contraction of either muscle. The association of GL/VL co-contractions with the knee angle values (Fig. 8.8) can contribute to suggest different GC epochs where the risk of concomitant occurrence of the two factors affecting ACL strain, i.e. GL/VL co-activations and knee joint extension, is higher in a cyclic activity of daily living such as walking. From this viewpoint, the nonnegligible occurrence of SW co-activation (OF=29.0 ± 16.1%) at low value of knee angle (around6°, Fig. 8.8), supports the relative peak of ACL strain observed by [35] at the end of the swing phase, immediately prior the heel strike.

Co-contractions during child walking

The analysis of thigh muscle co-contraction during child walking allowed to identify five different activation modalities for each muscle, describing the large variability of muscular recruitment. RF and VM showed a concomitant activity from late swing to following loading response (Fig. 8.11, A–C), as in adults [6]. This superimposition could be interpreted as a synergic action of muscles for assisting knee extension and developing muscle tension for weight acceptance and for controlling following weight bearing in early stance. RF and VM overlapped their activity also in push-off phase (Fig. 8.11, B-C), working in synergy for controlling rapid knee flexion. Simultaneously, VM is contributing to patella stabilization before entering pre-swing phase and RF is taking part in hip flexion. Co-contraction activity between VM and LH was detected in a high percentage of strides (89.8 ± 5.6%). It likely occurs in order to assist knee extension, developing

muscle tension for weight acceptance during loading response, and to control knee flexion. Concomitant activity of VM and LH was detected also during push-off phase, showing a lower occurrence frequency (12.2 ± 3.8%). In this gait phase, VM is recruited to modulate rapid knee flexion and to stabilize the patella before entering pre-swing phase, while LH is acting as hip extensor in the stabilization of pelvis and to propel body forward by extending hip backward [5]. Working VM and LH on different joints, this concomitant activity should not be considered as an actual co-contraction. A further superimposition between VM and LH activity was observed in flat-foot contact phase (Fig. 8.12, C). However, its action was considered not relevant, since it occurred very rarely (3.4 ± 2.2% of strides). Superimposition of LH with RF activity from terminal swing to following loading response was detected in more than 90% of considered strides (Fig. 8.13, D). This superimposition in terminal swing could be reasonably interpreted as an action of muscles across the knee, occurring to assist knee extension in preparation to weight acceptance [5]. To test whether variability noted in thigh-muscle co-contraction could be related to age of children, an age-related analysis was also performed. All four main activation modalities reported in mean values in Fig. 8.14 were detected in every single child, irrespective of age. Moreover, no changes or trends were noted with increasing age in co-contraction occurrence frequency. These findings suggest that across this age-range, variability of thigh-muscle co-contraction does not depend on age of children.

For a complete picture of child muscle co-contraction patterns, the reciprocal role of intrinsic (extensor digitorum brevis, EDB) and extrinsic foot muscles (tibialis anterior and gastrocnemius lateralis) has been analyzed. In school-age children, EDB muscle adopted different modalities in a number of activations, in occurrence frequency, and in the timing of signal onset/offset, in different strides of the same walking trial. Large muscle-activity variability was also detected for the TA and GL. EDB pattern of activation was observed mainly during the second half of the stance phase. In this phase, EDB activity was detected in 100% of the considered subjects and of the considered strides (Fig. 8.17). The activity in this percentage of the gait cycle (around 30%–55%) is recognized as the typical activation for the EDB during normal walking [5]. In adults, EDB activation during the early mid-stance phase has been interpreted as the active participation of this intrinsic dorsal muscle of the foot in controlling mid-tarsal dorsiflexion to regulate the shock-absorbing mechanism.

Moreover, when advancing the body, the action of the EDB is suggested to be present to control mid-foot stability by developing muscle tension for weight-bearing [5]. Considering that activation intervals of the EDB activation showed (Fig. 8.16) is comparable with what is reported in adults [5], the previous physiological considerations could be reasonably extended to children. A further region of EDB activity was detected in the swing phase. This activity occurs in a minor number of subjects (50%), around 85% of the gait cycle (Fig. 8.16). To our knowledge, this activity has never been reported in either children or in adults. An explanation of the activation of the EDB in this phase of the gait cycle could be related to the activity of the muscle for the correct positioning of the foot, in preparation of the following heel strike. The region of main EDB activity approximately superimposed the region of no activity (or low activity) for the TA (20%–60% of the gait cycle) and vice versa (60%–20% of the gait cycle); i.e. when the EDB is on, the TA is off and when the EDB is off, the TA is on. This suggested that the EDB and TA worked mainly as antagonist muscles for the ankle joint during walking. Otherwise, the regions of activity of the EDB and GL (mid-stance and final swing) were practically superimposed, indicating that the EDB and GL did not oppose each other in action, but acted in synergy for the control of the ankle joint.

The role of gender in the evolution of gait could be an important factor of investigation, for studying the different stages of gait maturation. Gender-related differences on ankle muscle co-contraction and gender-related comparison with adults provide a novel insight in maturation of gait. First relevant finding is that in school- age children, no significant differences ($p > 0.05$) were observed between females and males in GL and TA, considering both mean onset/offset instants of activation and occurrence frequency. This suggested that school-age-child walking is not conditioned by gender. Thus, to deepen the analysis of the different gender-related behavior detected between children and young adults, two sub-groups were extracted from C-group: YC-group (youngest children group, 6–8 years) and OC-group (oldest children group, 10–12 years). Results in YC-group confirmed what was found in the whole C-group, i.e. no gender-related differences in sEMG activity in child. Interesting findings were found in OC-group. In this group, females showed a significant increase in occurrence frequencies in the modalities with a higher number of activations and a significant decrease in occurrence frequencies in the modalities with a lower number of activations

for GL, exactly as in young adults. This suggests that gender-related differences in sEMG occurrence frequency do not characterize child walking in early years (6–8 years), start occurring when adolescence is approaching (10–12 years). These findings seem to support previous studies on maturation of gait [36][37], which indicate adolescence as the time-range where the gait is completing its maturation path.

8.5 Conclusion

The electromyographic characterization of motor control during walking leaded to four main results. The first result was the identification of up to three co-contraction intervals between quadriceps femoris and medial hamstrings in a single gait cycle. Moreover, the assessment of significant differences in myoelectric activation patterns between genders pointed out a more complex muscular recruitment in females respect to males. This higher complexity was mirrored by the higher occurrence frequency of activation modalities which presented a high number of active intervals in a single gait cycle, rather than differences in temporal onset/offset of muscular bursts. The higher recurrence of each co-contraction in females respect to males during walking allowed to consider gender as a not negligible factor in the evaluation of muscular co-contraction.

The second relevant results involved GL/VL co-contraction. Outcomes showed that late foot-contact and swing co-contraction could deserve particular attention: in both cases the knee joint was close to the full extension and thus, considering also the anterior tibia translation due to the quadriceps activity, the simultaneous gastrocnemius burst could lead to an enhanced knee ligaments elongation. These findings could be useful for possible applications in ACL reconstructed individuals, which present a higher risk of re-rupture, in order to deepen the neuromuscular mechanisms regulating knee joint stability, also in terms of different functional abilities.

The third result was the presence of thigh-muscles co-contractions for healthy children. Children regularly use co-contraction activities between QF and hamstring muscles in weight acceptance during walking. This supports the hypothesis of a regulatory role of QF/hamstrings co-contraction in providing knee joint stability. Concomitant activity of QF and hamstring muscles was detected

also during push-off phase, showing a large variability intra and inter subjects and a lower occurrence frequency. It could be intended for controlling rapid knee flexion and/or stabilizing pelvis during body progression. To a complete picture of child co-contraction, a frame of reference for the quantification of intrinsic and extrinsic muscle is useful, in order to provide insights in mechanisms regulating ankle-foot stability. Regions of EDB and GL activity were practically overlapped, suggesting that EDB and GL worked synergistically for foot and ankle-joint control in able-bodied-children walking, in a large percentage of strides. Otherwise, EDB and TA muscles are recruited in antagonistic way in controlling foot movement. Short and sporadic superimpositions between muscles may be interpreted as actions exercised by neuromotor system to control ankle-joint movement.

The final result is related to a novel insight in maturation of gait in the recruitment of ankle muscles. Findings suggested that the acknowledged propensity of adult females for a more complex recruitment of TA and GL is not present in school-age children and likely starts developing with the approaching of adolescence.

In conclusion, SGA allowed to provide reference data on lower-limb-muscle co-contraction during heathy adult and child walking. Despite the accuracy of the methodology and the reliability of the results achieved, further mechanics and kinematics studies are needed to confirm the physiological causes leading to the presences of thigh co-contraction, GL/VL concomitant recruitment, gender- related differences in healthy subjects, thigh co-contraction in child walking, gender-related differences for child subjects in ankle muscle co-contraction and the role of EDB in maturation of gait.

Chapter references

[1] S. J. Olney, "Quantitative evaluation of cocontraction of knee and ankle muscles in normal walking," in *Biomechanics IX: International Congress of Biomechanics*, 1983, vol. 9, pp. 431–436.

[2] R. Baratta, M. Solomonow, B. H. Zhou, D. Letson, R. Chuinard, and R. D'Ambrosia, "Muscular coactivation. The role of the antagonist musculature in maintaining knee stability.," *Am. J. Sports Med.*, 1988.

[3] A. Mengarelli, E. Maranesi, L. Burattini, S. Fioretti, and F. Di Nardo, "Co-contraction activity of ankle muscles during walking: A gender comparison," *Biomed. Signal Process. Control*, vol. 33, pp. 1–9, 2017.

[4] F. Di Nardo, A. Mengarelli, E. Maranesi, L. Burattini, and S. Fioretti, "Assessment of the ankle muscle co-contraction during normal gait: A surface electromyography study," *J. Electromyogr. Kinesiol.*, vol. 25, no. 2, pp. 347–354, 2015.

[5] J. Perry, *Gait Analysis: Normal and Pathological Function*, vol. 12. 1992.

[6] A. Strazza, A. Mengarelli, S. Fioretti, L. Burattini, V. Agostini, M. Knaflitz, and F. Di Nardo, "Surface-EMG analysis for the quantification of thigh muscle dynamic co-contractions during normal gait," *Gait Posture*, vol. 51, pp. 228–233, 2017.

[7] J. L. Honeine, M. Schieppati, O. Gagey, and M. C. Do, "The Functional Role of the Triceps Surae Muscle during Human Locomotion," *PLoS One*, 2013.

[8] S. T. Da Fonseca, P. L. P. Silva, J. M. Ocarino, R. B. Guimaràes, M. T. C. Oliveira, and C. A. Lage, "Analyses of dynamic co-contraction level in individuals with anterior cruciate ligament injury," *J. Electromyogr. Kinesiol.*, vol. 14, no. 2, pp. 239–247, 2004.

[9] B. C. Fleming, P. A. Renstrom, G. Ohlen, R. J. Johnson, G. D. Peura, B. D. Beynnon, and G. J. Badger, "The gastrocnemius muscle is an antagonist of the anterior cruciate ligament," *J. Orthop. Res.*, 2001.

[10] M. Adouni, A. Shirazi-Adl, and H. Marouane, "Role of gastrocnemius activation in knee joint biomechanics: gastrocnemius acts as an ACL antagonist," *Comput. Methods Biomech. Biomed. Engin.*, 2016.

[11] H. Fujiya, P. Kousa, B. C. Fleming, D. L. Churchill, and B. D. Beynnon, "Effect of muscle loads and torque applied to the tibia on the strain behavior of the anterior cruciate ligament: An in vitro investigation," *Clin. Biomech.*, 2011.

[12] A. Mengarelli, A. Gentili, A. Strazza, L. Burattini, S. Fioretti, and F. Di Nardo, "Co-activation patterns of gastrocnemius and quadriceps femoris in controlling the knee joint during walking," *J. Electromyogr. Kinesiol.*, vol. 42, no. July, pp. 117–122, 2018.

[13] W. Berger, J. Quintern, and V. Dietz, "Pathophysiology of gait in children with cerebral palsy," *Electroencephalogr. Clin. Neurophysiol.*, 1982.

[14] P. Crenna, "Spasticity and 'spastic' gait in children with cerebral palsy," *Neuroscience and Biobehavioral Reviews*. 1998.

[15] K. Falconer and D. A. Winter, "Quantitative assessment of co-contraction at the ankle joint in walking.," *Electromyogr. Clin. Neurophysiol.*, 1985.

[16] F. Di Nardo, A. Mengarelli, L. Burattini, E. Maranesi, V. Agostini, A. Nascimbeni, M. Knaflitz, and S. Fioretti, "Normative EMG patterns of ankle muscle co-contractions in school-age children during gait," *Gait Posture*, vol. 46, pp. 161–166, 2016.

[17] F. Di Nardo, A. Strazza, A. Mengarelli, S. Ercolani, N. Morgoni, L. Burattini, V. Agostini, M. Knaflitz, and S. Fioretti, "Surface EMG patterns for quantification of thigh muscle co-contraction in school-age children: Normative data during walking," *Gait Posture*, 2018.

[18] F. Di Nardo, A. Strazza, M. S. Palmieri, A. Mengarelli, L. Burattini, O. Orsini, A. Bortone, and S. Fioretti, "Detection of surface-EMG activity from the extensor digitorum brevis muscle in healthy children walking," *Physiol. Meas.*, 2018.

[19] F. Di Nardo, G. Laureati, A. Strazza, A. Mengarelli, L. Burattini, V. Agostini, A. Nascimbeni, M. Knaflitz, and S. Fioretti, "Is child walking conditioned by gender? Surface EMG patterns in female and male children," *Gait Posture*, vol. 53, pp. 254–259, 2017.

[20] H. J. Hermens, B. Freriks, C. Disselhorst-Klug, and G. Rau, "Development of recommendations for SEMG sensors and sensor placement procedures," *J. Electromyogr. Kinesiol.*, vol. 10, no. 5, pp. 361–374, 2000.

[21] V. Agostini, G. Balestra, and M. Knaflitz, "Segmentation and classification of gait cycles," *IEEE Trans. Neural Syst. Rehabil. Eng.*, vol. 22, no. 5, pp. 946–952, 2014.

[22] P. Bonato, T. D'Alessio, and M. Knaflitz, "A statistical method for the measurement of muscle activation intervals from surface myoelectric signal during gait," *IEEE Trans. Biomed. Eng.*, vol. 45, no. 3, pp. 287–299, 1998.

[23] V. Agostini and M. Knaflitz, "An algorithm for the estimation of the signal-to-noise ratio in surface myoelectric signals generated during cyclic movements," *IEEE Trans. Biomed. Eng.*, vol. 59, no. 1, pp. 219–225, 2012.

[24] A. R. Den Otter, A. C. H. Geurts, T. Mulder, and J. Duysens, "Gait recovery is not associated with changes in the temporal patterning of muscle activity during treadmill walking in patients with post-stroke hemiparesis," *Clin. Neurophysiol.*, 2006.

[25] V. Agostini and M. Knaflitz, "Statistical Gait Analysis," in *Distributed Diagnosis and Home Healthcare*, 2012, pp. 99–121.

[26] G. Staude, C. Flachenecker, M. Daumer, and W. Wolf, "Onset Detection in Surface Electromyographic Signals :," *J. Appl. Signal Process.*, 2001.

[27] F. Di Nardo, V. Agostini, M. Knaflitz, A. Mengarelli, E. Maranesi, L. Burattini, and S. Fioretti, "The occurrence frequency: A suitable parameter for the evaluation of the myoelectric activity during walking," in *Proceedings of the Annual International Conference of the IEEE Engineering in Medicine and Biology Society, EMBS*, 2015, vol. 2015–Novem, pp. 6070–6073.

[28] G. Frost, J. Dowling, K. Dyson, and O. Bar-Or, "Cocontraction in three age groups of children during treadmill locomotion," *J. Electromyogr. Kinesiol.*, vol. 7, no. 3, pp. 179–186, 1997.

[29] V. Agostini, A. Nascimbeni, A. Gaffuri, P. Imazio, M. G. Benedetti, and M. Knaflitz, "Normative EMG activation patterns of school-age children during gait," *Gait Posture*, vol. 32, no. 3, pp. 285–289, 2010.

[30] A. Nene, C. Byrne, and H. Hermens, "Is rectus femoris really a part of quadriceps? Assessment of rectus femoris function during gait in able-bodied adults," *Gait Posture*, vol. 20, no. 1, pp. 1–13, 2004.

[31] F. Di Nardo and S. Fioretti, "Statistical analysis of surface electromyographic signal for the assessment of rectus femoris modalities of activation during gait," *J. Electromyogr. Kinesiol.*, vol. 23, no. 1, pp. 56–61, 2013.

[32] R. P. Grelsamer and J. Gould, "The biomechanics of the patella," in *The Knee Joint: Surgical Techniques and Strategies*, vol. 9782287993, 2012, pp. 519–523.

[33] J. B. Dingwell and L. C. Marin, "Kinematic variability and local dynamic stability of upper body motions when walking at different speeds," *J. Biomech.*, vol. 39, no. 3, pp. 444–452, 2006.

[34] D. A. Winter and H. J. Yack, "EMG profiles during normal human walking: stride-to-stride and inter-subject variability," *Electroencephalogr. Clin. Neurophysiol.*, 1987.

[35] K. A. Taylor, H. C. Cutcliffe, R. M. Queen, G. M. Utturkar, C. E. Spritzer, W. E. Garrett, and L. E. DeFrate, "In vivo measurement of ACL length and relative strain during walking," *J. Biomech.*, 2013.

[36] T. H. Petersen, M. Kliim-Due, S. F. Farmer, and J. B. Nielsen, "Childhood development of common drive to a human leg muscle during ankle dorsiflexion and gait," *J. Physiol.*, 2010.

[37] D. Sutherland, "The development of mature gait," *Gait and Posture*, vol. 6, no. 2. pp. 163–170, 1997.